DEVELOPMENT OF THICK-FILM OXIDE-BASED ELECTRONIC CERAMICS

Rok Rudež

Doctoral Dissertation
Jožef Stefan International Postgraduate School
Ljubljana, Slovenia

Supervisor: Prof. Dr. Slavko Bernik, Jožef Stefan Institute, Jamova cesta 39, 1000 Ljubljana, Slovenia

Evaluation Board:
Asst. Prof. Dr. Nina Daneu, Chair, Jožef Stefan Institute, Jamova cesta 39, 1000 Ljubljana, Slovenia
Asst. Prof. Marko Hrovat, Member, Jožef Stefan Institute, Jamova cesta 39, 1000 Ljubljana, Slovenia
Prof. Dr. Andrzej Dziedzic, Member, Faculty of Microsystem Electronics and Photonics, Wroclaw University of Technology, Długa Street 63, 53-663 Wroclaw, Poland

MEDNARODNA PODIPLOMSKA ŠOLA JOŽEFA STEFANA
JOŽEF STEFAN INTERNATIONAL POSTGRADUATE SCHOOL



Rok Rudež

DEVELOPMENT OF THICK-FILM OXIDE-BASED ELECTRONIC CERAMICS

Doctoral Dissertation

RAZVOJ DEBELOPLASTNE OKSIDNE ELEKTRONSKE KERAMIKE

Doktorska disertacija

Supervisor: Prof. Dr. Slavko Bernik

Ljubljana, Slovenia, December 2016

I want to dedicate this thesis to my family and especially to my wife Eva, who stood by me and gave me all the support.

Acknowledgments

I acknowledge the financial support from the Slovenian Research Agency (Project PR-05038, Project Grant L2-4192 and Program Contact Number P2-0084).

I am also grateful to my co-workers at the K7, K5 and F3 departments for their technical support and advice.

For their advice and support I also wish to thank Andrzej Dziedzic and Piotr Markowski from the Faculty of Microsystem Electronics and Photonics, Wroclaw University of Technology, where a major part of my experimental work on thermoelectrics was carried out.

Abstract

The screen printing is a mature technology for preparing thick films and hybrid circuits. The advantages of the screen printing are miniaturization, faster and easier production of complex structures and lower production cost. However, an inherent problem in the preparation of thick-film oxide electronic ceramics could be low green density and hence porosity of fired films and excessive volatilization of volatile components during firing due to an extremely large area-to-volume ratio. In the dissertation the ZnO-based thick-film varistors and the thermoelectric microgenerators (TEMG) made from the *n*-type $(ZnO)_5In_2O_3$ and the *p*-type $Ca_3Co_4O_9$ materials were developed using screen printing processing.

The screen-printing of the thick-film varistors shows two critical problems. One is the high porosity of the thick-film varistors after firing, which mainly results from the low green density of the films, and hinders their electrical characteristics. The research in the first part of the dissertation showed that the increase of the solids load in the screen-printing inks improves green density. It also enhances densification and microstructure development, and results in reduced porosity of the films fired at 900 °C for 15 minutes, which consequently showed also better electrical characteristics. The development of the screen-printing inks with high solids load is discussed, considering the influence of the inks' composition in regard to the used vehicle, amount of added surfactant and binder, and the content of solids load on the rheology of the inks, their printing characteristics and quality of the printed films. The formulation of a high-solids load screen-printing ink was set and used for further development of the thick-film varistors and the thick-film thermoelectrics.

Regarding the second problem of excessive volatilization of the Bi_2O_3 during firing thick-film varistors, lower firing temperatures and short firing times are preferred. At such firing conditions the presence of free Bi_2O_3 to form a liquid phase, which enhances the microstructure development, is desired. Accordingly, the second part of the dissertation shows and discusses the significance of a proper amount of the Bi_2O_3 and the Sb_2O_3-to-Bi_2O_3 ratio in the starting varistor powder mixture for enhanced electrical characteristics of the thick-film varistors.

In the last part of the dissertation the development of the screen-printed thermoelectric (TE) thick-films and the challenges for the low cost processing of the thermoelectric microgenerators (TEMGs) are presented and discussed. The TE thermopiles were successfully prepared from oxide-based TE materials, the *p*-type $Ca_3Co_4O_9$ (Ca349) and the *n*-type $(ZnO)_5In_2O_3$ (Z5I). The Ca349 thick films, fired at 920 °C for 15 minutes, had TE characteristics comparable to the bulk ceramics. However, the Z5I thick film had very low TE characteristics due to poor densification even after firing at 1350 °C causing strong interaction with alumina substrate and sublimation of ZnO, which represents a serious challenge.

Povzetek

Sitotisk je tradicionalna tehnologija izdelave debelih filmov elektronskih komponent, integriranih v elektronske naprave. Prednosti te tehnologije so miniaturizacija, hitra in enostavna metoda izdelave kompleksnih struktur in nizki stroški izdelave. Slabosti te tehnike pri pripravi debeloplastne oksidne elektronske keramike sta lahko nizka zelena gostota natisnjenih filmov ter posledično velika poroznost filmov po žganju in pa izhlapevanje hlapnih komponent zaradi velikega razmerja med površino in volumnom debelih filmov. V disertaciji je predstavljen razvoj debeloplastnih varistorjev na osnovi ZnO in termoelektričnih mikrogeneratorjev na osnovi $(ZnO)_5In_2O_3$ tipa n in $Ca_3Co_4O_9$ tipa p z uporabo tehnologije sitotiska.

Izdelava debeloplastnih varistorjev z metodo sitotiska kaže dve ključni pomanjkljivosti. Ena je velika poroznost žganih filmov, ki je v veliki meri posledica majhne zelene gostote debelih filmov pred žganjem in povzroči slabše električne lastnosti. V prvem delu doktorskega dela je predstavljen vpliv zviševanja deleža suhe snovi v pasti za sitotisk na povečanje zelene gostote natisnjenih filmov, izboljšanje zgoščevanja in razvoj mikrostrukture in s tem zmanjšanje poroznosti filmov po žganju pri 900 °C 15 minut, kar se pokaže tudi v boljših električnih lastnostih. Predstavljeni in pojasnjeni so rezultati študija vpliva sestave paste glede na uporabljen nosilec, dodatek surfaktanta, veziva in delež suhe snovi (varistorskega prahu) na reološke lastnosti paste in posledično njene lastnosti med tiskanjem in kvaliteto natisnjenega filma. Določena je bila sestava paste z visokim deležem suhe snovi in odličnimi lastnostmi za sitotisk, kar je omogočilo optimalne pogoje pri nadaljnjem razvoju debeloplastnih varistorjev in termoelektrikov.

Zaradi drugega problema, ki je izhlapevanje Bi_2O_3, so nižje temperature ter krajši časi žganja ustreznejši. Pri takšnih pogojih žganja je prisotnost prostega Bi_2O_3, ki povzroči nastanek taline is s tem boljše zgoščevanje in razvoj mikrostrukture, zaželena. Glede na to v drugem delu disertacije pojasnim vpliv ustrezne količine dodatka Bi_2O_3 in razmerja Sb_2O_3/Bi_2O_3 v začetni sestavi varistorskega prahu na izboljšanje električnih lastnosti debeloplastnih varistorjev, žganih pri 900 °C 15 minut.

V zadnjem delu disertacije predstavim razvoj debeloplastnih termoelektrikov in izzive pri izdelavi debeloplastnih termoelektričnih mikrogeneratorjev s cenovno ugodno metodo sitotiska. Uspešno sem izdelal mikrogeneratorje na osnovi obetavnih oksidnih termoelektričnih materialov, in sicer $(ZnO)_5In_2O_3$ (Z5I) tipa n in $Ca_3Co_4O_9$ (Ca349) tipa p. Debeloplastni termoelektrik na osnovi Ca349, žgan pri 920 °C, je imel podobne termoelektrične lastnosti kot masivna keramika Ca349. Mikrogenerator na osnovi Z5I, ki je bil glede na literaturo izdelan prvič, je imel bistveno slabše termoelektrične lastnosti zaradi porozne mikrostrukture kljub žganju pri visoki temperaturi 1350 °C, pri kateri je prišlo do močne reakcije s substratom in sublimacije ZnO, tako da njihov razvoj predstavlja velik izziv.

Contents

List of Figures **xi**

List of Tables **xv**

Abbreviations and Symbols **xvii**

1 Introduction **1**
1.1 Thick-Film Technology ... 1
1.1.1 Screen printing ... 2
1.1.2 Screen-printing ink ... 4
1.1.3 Rheology tests ... 6
1.2 ZnO-Based Thick-Film Varistor ... 7
1.2.1 Electrical properties of the varistors ... 7
1.2.2 Microstructure and chemistry of varistor ceramics ... 9
1.2.3 Development of thick-film varistors ... 12
1.3 Thick-Film Thermoelectric Microgenerators ... 13
1.3.1 Thermoelectricity ... 13
1.3.2 Thermoelectric materials ... 15
1.3.3 Development of the thick-film thermoelectric generators ... 18

2 Aims and Hypothesis **21**
2.1 Description of the Problem ... 21
2.2 Aims and Goals of the Dissertation ... 22

3 Materials and Methods **25**
3.1 Processing ... 25
3.1.1 Lists of chemicals and processing equipment ... 25
3.1.2 Preparation of the screen-printing ink ... 27
3.1.3 Preparation of the thick-film varistors ... 29
3.1.4 Preparation of the thick-film thermoelectrics ... 30
3.2 Sample Characterization ... 32
3.2.1 Ink rheology characterization ... 32
3.2.2 Evaluation of the quality of the printed film ... 32
3.2.3 Characterization of electrical properties of thick-film varistors ... 33
3.2.4 Characterization of thick-film thermoelectrics ... 34
3.2.5 Methods for microstructural analysis ... 35

4 Results and Discussion **37**
4.1 Optimization of the Screen-Printing Paste ... 37
4.1.1 Inks based on commercial vehicles ... 37
4.1.2 Inks based on our-selves made vehicles ... 41

4.1.2.1 Influence of the surfactant on the ink's rheology and the quality of the printed thick film 41
4.1.2.2 Influence of the binder on the ink's rheology and the quality of the printed thick film 43
4.1.2.3 Influence of the solids load on the ink's rheology and the quality of the printed thick film 44
4.2 Thick-Film Varistors 46
4.2.1 Influence of the solids load on the microstructure and the electrical properties 46
4.2.2 Influence of the Bi_2O_3 content and Sb/Bi ratio on the microstructure and the electrical properties 49
4.2.3 Influence of the firing time on the microstructure and the electrical properties 54
4.3 Thick-Film Thermoelectric Micro Generators 54
4.3.1 Thick-film thermoelectric microgenerators based on $Ca_3Co_4O_9$ 55
4.3.2 Thick-film thermoelectric microgenerators based on $(ZnO)_5In_2O_3$ 60

5 Conclusions **65**

References **69**

Bibliography **75**

Biography **77**

List of Figures

Figure 1.1: Schematic presentation of the screen printing process showing: a) deposited ink on the screen, b) traveling of the squeegee along the screen, and c) the end of the printing leaving the printed film with a desired pattern. [8] 2
Figure 1.2: Examples of different patterns of thick-film microgenerators made with screen printing: a) showing a circular structure and b) showing a rectanglar structure. [10] 3
Figure 1.3: Scheme of the thick-film cros-section with defined lines and variation in thickness. 3
Figure 1.4: Schematic presentation of viscosity as a function of shear rate of shear thickening (rheopexy), Newtonian and shear thinning (thixotropy) fluids. [14] 4
Figure 1.5: Schematic presentation of the thixotropic liquid viscosity behaviour as a function of shear rate during applied shear stress (priniting) and after shear stress is removed (relaxation). [9].....5
Figure 1.6: Graph showing shear rates and viscosity change during the printing stages: stirring of the ink, squeegee pressure, flow of the ink through the screen, leveling of the ink. [19] 6
Figure 1.7: Varistor connected in AC/DC circuit for potecting a device. [23] 8
Figure 1.8: Graph showing current I versus applied voltage U for typical varistor. On the graph three working regions are shown: pre-switched, non-linear and high currents [3, 21] 8
Figure 1.9: The SEM microgaph showing a varistor microstucture, which contains all phases typical for varistor ceramics: ZnO grains, spinel grains, Bi_2O_3 pahse and pyrochlore phase. 10
Figure 1.10:Schematic presentation of maximized zT and P value for doped semiconductors, which are directly affected by the S, σ and λ as a function of carrier concentration. [45] 14
Figure 1.11:Schematic view of a thermoelectric module conecting the p-type and the n-type material. [45] 15
Figure 1.12: Schematic presentation of the TE materials according to the abundance of the elements in their composition, environment impact and the temperature range of their application. [46] 16
Figure 1.13:The crystal structure of $Ca_3Co_4O_9$ consists of two sublattice structures, the CoO_2 layers and the Ca_2CoO_3 layers. [47].....17
Figure 1.14: TEM micrograph showing a $(ZnO)_kIn_2O_3$ superlattice structure with aranged planar defects of InO_2^- and »zig-zag« ZnO/In defects in between. 17
Figure 1.15:Schematic view of a thick-film microgenerator made from p- or n-type thermocouples [63]. 19
Figure 3.1: Sandwich configuration of the thick-film varistor [64]. 30
Figure 3.2: Scheme of a thick-film meander-type structure made from the oxide TE material for measurement of the electrical conductivity. 31
Figure 3.3: Scheme of a thick-film microgenerator made from the oxide TE material leg and the metal electrode leg. [65] 31

Figure 3.4: Optical micrographs showing typical defects observed in the screen-printed films prepared in the process of ink optimisation: a) cracks and missing defect, b) mesh imprints and holes, c) creping defect and d) the defect-free film with a smooth surface. 33
Figure 3.5: Laboratory set-up for measurements of the Seebeck coefficient (S) made from multimeter, power generator, measuring device and computer. 34
Figure 3.6: Schematic side view of oxide-based thick film placed in laboratory set up between the hot block and cold block. 34
Figure 4.1: Results of the FT showing change in the viscosity vs. shear rate for the inks with different solids load CV10-50 (50 %), CV10-55 (55 %) and CV10-60 (60 %). 38
Figure 4.2: Result of the SST showing a change in the viscosity after the removal of the shear stress in inks with various amounts of solids load CV10-50 (50 wt. %), CV10-55 (55 wt. %) and CV10-60 (60 wt. %). 38
Figure 4.3: Results of the FT showing change in the viscosity vs. shear rate of the ink with 0.6 wt. % of surfactant CV6-60S and without surfactant CV6-60WS..... 39
Figure 4.4: Results of the FT showing change in the viscosity vs. shear rate of the ink with 0.6 wt. % of surfactant A-70S and without surfactant A-70WS. 41
Figure 4.5: Confocal micrographs showing the surface (a, c, e, g) and the edge (b, d, f, h) of the printed films. 42
Figure 4.6: Results of the FT showing change in the viscosity vs. shear rate for the inks with various amounts of binder A-70S (2.2 wt. %), B-70S (2.6 wt. %), and C-70S (3.0 wt. %). 43
Figure 4.7: Result of the SST showing a change in the viscosity after the removal of the shear stress in inks with various amounts of binder: A-70S (2.2 wt. %), B-70S (2.6 wt. %), and C-70S (3.0 wt. %). 44
Figure 4.8: Results of the FT showing change in the viscosity vs. shear rate for the inks with various amounts of solids load B-65S (65 wt. %), B-70S (70 wt. %), and B-75S (75 wt. %). 45
Figure 4.9: Result of the SST showing a change in the viscosity after the removal of the shear stress in inks with various amounts of solids load B-65S (65 wt. %), B-70S (70 wt. %), and B-75S (75 wt. %). 45
Figure 4.10: Confocal micrographs showing the surface (a, c, e) and the edge (b, d, f) of the printed films. 46
Figure 4.11: SEM micrographs of thick-film varistors fired at 900 °C, made from screen-printing inks containing different amount od solids load a) CV10-50S (50 wt. %), b) CV6-60WS (60 wt. %), c) B-65S (65 wt. %) and d) B-70S (70 wt. %). 47
Figure 4.12: Voltage–current density (U–J) characteristics of printed varistors made from inks with different solids loads CV10-50S (50 wt. %), CV6-60WS (60 wt. %), B-65S (65 wt. %) and B-70S (70 wt. %). 48
Figure 4.13: Voltage–current density (U–J) characteristics of printed varistors made with different Bi_2O_3 amounts: DV4 (0.4 wt. %), DV2 (0.8 wt. %) and DV5 (1.6 wt. %). 50
Figure 4.14: SEM micrographs of thick-film varistors with different Bi_2O_3 contents and different Sb-Bi ratio. 51
Figure 4.15: Histograms of the grain size distribution measured for samples DV1, DV2, DV3, DV4, DV5 and DV6, showing grain size and their proportion. 52
Figure 4.16: Voltage–current density (U–J) characteristics of printed varistors made with different Sb/Bi ratios DV1 (0.25), DV2 (0.8) and DV3 (1.25)..... 53
Figure 4.17:Microstructures of a polished cross-section of the bulk ceramics and powders of the $Ca_3Co_4O_9$ (Ca349) and $(ZnO)_5In_2O_3$ (Z5I) TE materials..... 55
Figure 4.18:The X-ray diffractograms of the $(ZnO)_5In_2O_3$ and $Ca_3Co_4O_9$ powders. 55
Figure 4.19:Screen-printed thick-film microgenerator made from ten Ca349 legs and ten Ag/Pd legs connected in series..... 56

Figure 4.20: SEM micrograph of the Ca349 thick-film: cross-section a) and surfaces b) fired temperature of 900 °C (T1) and cross section d) and surfaces c) fired temperature of 920 °C (T2). 56
Figure 4.21: Temperature dependence of the specific resistivity for Ca349 thick-films fired at different temperatures Ca349-T1 (900 °C), Ca349-T2 (920 °C).....57
Figure 4.22: Temperature dependence of the Seebeck coeficient of the Ca349 thick-films fired at different temperatures Ca349-T1 (900 °C), Ca349-T2 (920 °C).....58
Figure 4.23: Temperature dependence of the Seebeck coeficient of Ca349 thick-films fired at different temperatures Ca349-T1 (900 °C), Ca349-T2 (920 °C).....58
Figure 4.24:Screen-printed thick-film microgenerator made from ten Z5I legs and ten Pt legs connected in series. 60
Figure 4.25: SEM micrograph of the Z5I thick-film: cross-section a) and surfaces b) fired temperature of 1250 °C (T1), cross section d) and surfaces c) fired temperature of 1300 °C (T2), cross section e) and surfaces f) fired temperature of 1350 °C (T3) and cross section h) and surfaces g) fired temperature of 1400 °C (T4).....61
Figure 4.26: Temperature dependence of specific resistivity of the Z5I thick-films fired at different temperatures Z5I-T1 (1250 °C), Z5I-T2 (1300 °C) and Z5I-T3 (1350 °C). 62
Figure 4.27: Temperature dependence of the Seebeck coefficient of the Z5I thick films fired at different temperatures Z5I-T2 (1300 °C) and Z5I-T3 (1350 °C). 63
Figure 4.28: Temperature dependence of power factor (P) for Z5I thick films fired at different temperatures Z5I-T2 (1300 °C) and Z5I-T3 (1350 °C).....64

List of Tables

Table 3.1 List of chemicals used in this work divided into three groups: thick-film technology, thick-film varistors, thick-film thermoelectrics (in alphabetic order).....25
Table 3.2: List of equipment for processing and characterization of the thick-film (in alphabetic order). 26
Table 3.3: Composition of the screen-printing inks in regard to solids load, binder and surfactant, divided in the three groups based on the vehicle used: commercial high- and low-viscosity vehicles CV10 and CV6 , respectively, and vehicles I prepared using standard components (2-(2-butoxyethxy)ethyl) acetate and α-terpineol in the ratio 1:4, respectively. 27
Table 3.4: The compositions of the varistor powder mixtures (i.e. solids load) in the screen-printed inks, varied for the amount of added Bi_2O_3 and the Sb_2O_3-to-Bi_2O_3 (Sb/Bi) ratio at the same amount of other varistor dopants. 29
Table 4.1: Compositions and rheological properties of the inks, and the results of the optical examinations of the dried single-layer thick films deposited on an alumina substrate by screen printing the inks (N/A – not applicable, X – not present, ✓ – present). 37
Table 4.2: The electrical characteristics of the thick-film varistors on an alumina substrate made from inks with different solids loads, fired at 900 ˚C (15 min). 48
Table 4.3: The electrical characteristics and average grain size of the thick-film varistors with different Bi_2O_3 contents and different Sb/Bi ratio.....49
Table 4.4 The electrical characteristics of the thick-film varistors with the composition DV1, fired at 900 °C for different durations. 54
Table 4.5: Electrical properties of Ca349 thick-films fired at different temperatures. 57
Table 4.6: Electrical properties of Z5I thick-films, fired at different temperatures. 62

Abbreviations and Symbols

THICK-FILM TECHNOLOGY

d_{50}	... Average particle size
EC	... Ethyl-cellulose
FT	... Flow test for the rheology measurement of the screen-printing inks
K	... Estimation of the rate of recovery calculated from the viscosity slope in the SST test
k	... Slope in the final stage of recovery calculated from the viscosity slope in the SST test
PCB	... Printed circuit boards
R	... Percentage of recovery of the viscosity calculated from the curve in the SST test, [%]
R_a	... Surface-roughness factor of the thick-film surface measured with the contact profilometer, [µm]
SST	... Screen-printing simulation test for rheology measurement of the screen-printing inks
TFT	... Thick-film technology
TNT	Transient network theory explaining rheology behaviour of the screen-printing inks
η_0	... Zero viscosity obtained from the FT curve, [Pa·s]
η_∞	... Infinite viscosity obtained from the FT curve, [Pa·s]

THICK-FILM VARISTORS

A/V	... Area/volume ratio of the thick-films
d	... ZnO grain size, [µm]
DSB	... Double Schottky barrier explaining varistor properties
GBs	... Grain boundaries explaining the microstructure of the varistor
I_C	... Capacitive current explaining electrical properties of the varistor, [A]
I_L	... Leakage current electrical properties of the varistor, [A]
I_R	... Resistive current electrical properties of the varistor, [A]
L	... Thick-film varistor thickness, [µm]
U_{NB}	... Break down voltage U_{NB} per barrier, [V]
U_N	... Nominal varistor voltage electrical properties of the varistor, [V]
U_T	... Threshold voltage electrical properties of the varistor, [V]

α ... Nonlinearity coefficient electrical properties of the varistor

THICK-FILM THERMOELECTRIC MICROGENERATORS

Ca349 $Ca_3Co_4O_9$ TE material
P ... Power factor describing electrical properties of the TEG, [W/mK^2]
S ... Seebeck coefficient describing electrical properties of the TE, [$\mu V/K$]
TE ... Thermoelectrics
TEG ... Thermoelectric generator
TEMG ... Thermoelectric microgenerator
U ... Voltage electrical properties of the TEG, [V]
$Z5I$ ... $(ZnO)_5In_2O_3$ TE material
ZT ... Figure of merit
σ ... Electrical conductivity describing electrical properties of the TE, [$m\Omega \cdot cm$]

Chapter 1

Introduction

1.1 Thick-Film Technology

The thick-film technology (TFT) is used to produce electronic devices such as microelectronic circuit boards, hybrid circuits and sensors. The manufacture of such devices is an additive process involving deposition of one or several layers of a functional material, such as conductors, resistors and dielectrics [1, 2, 3]. One of the most important thick-film deposition methods which is also used in this thesis is the screen printing. The first step in the screen printing is dispersing functional material in the form of a powder (solids load) in the organic phase (organic vehicle) to form a viscous ink. The ink composition must have suitable rheological properties to print [4, 5]. The second step is deposition of the ink on the substrate through the use of screen. The screen is partly masked with a filler. When the ink is forced, it goes through those remaining holes in the screen. On the substrate surface the replica of a pattern on the screen is obtained. The last step is firing the printed film to form an electronic component. The final form of a single- or multi-layer film with a defined pattern is known as thick film, hence the thick-film technology [2, 3]. A more detailed description of the screen-printing process is described in the next chapters.

The earliest printed films appeared as screen-printed films in microelectronics for making more efficient and cheaper printed circuit boards (PCB). The second step was manufacturing the whole set of electric passive components. The very beginning of the thick-film hybrid circuits as we know today occurred in the 1960s with the first `fired on´ resistor adopted by the IBM company. With additional advantage that the resistors and circuits could be trimmed. Today screen printing is used for manufacturing various devices, such as heating resistors, gauges for the exhaust system, fuel-cells, various gas sensors etc. [1, 2, 3]. The trend is to make use of new cost-efficient ways to mass produce microelectronic devices and the screen printing is one of the most mature and traditional print processes. Screen printing meets requirements, such as uniformity in thickness, fine line continuity and good pattern definition [1, 2, 3].

Despite the advantages of the screen-printing process, manufacturing of a new ceramic thick-film device from a functional material does not mean a straightforward process. In manufacturing thick films with similar properties as in bulk there are some problems to overcome. The first problem is the formation of ink with rheological properties compatible with the screen-printing process [1]. In the thesis we describe the optimization process of the screen-printing ink regarding the functional material.

The second problem is connected with the screen-printing ink composition. Ink consists of the inorganic powder (solids load) mixed in the organic vehicle. The organic vehicle is mostly made of solvent and binder. The organics burn out during the firing and consequently increase the porosity of the fired thick film compared to the bulk ceramics [1, 6]. In this thesis the influence on minimizing porosity with the increase of the solids load (inorganic powder) in the ink was studied. The first part of the thesis focuses on optimization of high solids load screen-printing inks with regard to different compositions and components on the ink properties and the quality of the printed films.

The second part of the thesis is divided into two case studies about manufacturing of the functional device using the screen-printing technology. The starting point was the ceramic material with required properties for an application in bulk. In this thesis we discuss optimization of thick-film varistors and thick-film oxide-based thermoelectrics with a focus on resolving their own drawbacks. Each of them is described in its own chapter.

1.1.1 Screen printing

The screen-printing is the most important and most mature technology in the field of thick-film deposition methods. In comparison to other technologies (i.e. drop-coating, tape casting etc.) it is simple, cheap and flexible. Its importance is in printing almost any material on different substrates. With screen-printing it is easy to produce films with different thicknesses and patterns, with uniformity in thickness, fine line continuity and good pattern definition [1, 7]. The process of the screen printing is schematically shown in Figure 1.1.

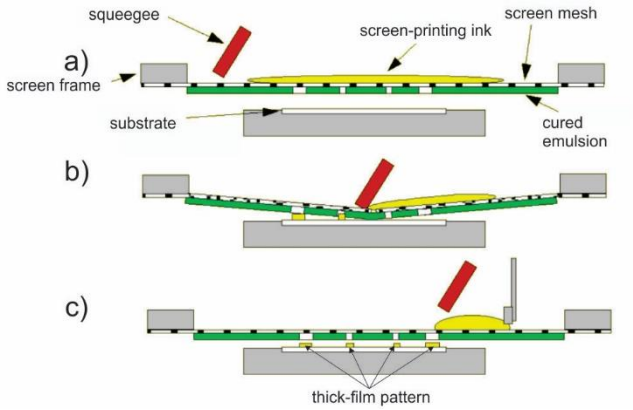


Figure 1.1: Schematic presentation of the screen printing process showing: a) deposited ink on the screen, b) traveling of the squeegee along the screen, and c) the end of the printing leaving the printed film with a desired pattern [8].

The screen-printing process starts with the formulation of the screen-printing ink. The ink consists of a functional material in the form of a powder (solids load) dispersed in the organic phase (organic vehicle). Next, the ink is deposited on the screen, which is made from a mesh mounted on a metallic frame. The mesh is prepared with coating, with the UV-curable emulsion, which is partly covered and cured photographically. The covered and thus uncured emulsion is removed, leaving an opening, a so-called stencil. The finished

stencil has open mesh areas through which the ink could be printed [2, 7, 9]. The screen is placed in close contact with the substrate, usually in the distance around 0.5 mm [7].

The printing starts with the traveling of the squeegee along the screen under pressure, as seen in Figure 1.1 b. The squeegee forces the ink through the stencil and at the same time presses the screen into close contact with the substrate. After printing the mesh is lifted and peels away from the substrate to regain its original position. A printed pattern of the ink, the so-called printed wet film, remains on the substrate [2, 3]. A few of the final pattern structures of the printed thick-film are shown in Figure 1.2.

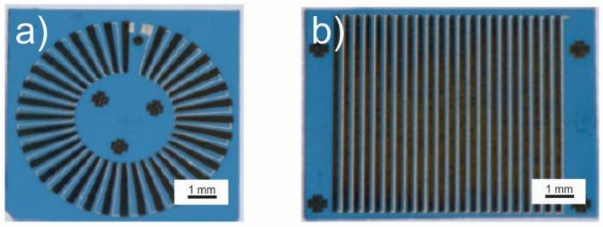


Figure 1.2: Examples of different patterns of thick-film microgenerators made with screen printing: a) showing a circular structure and b) showing a rectanglar structure [10].

The thickness of the printed wet film could be mainly defined by screen, ink flow behaviour (rheology) and the number of prints. The thickness increases with the number of prints and is limited with the distance between screen and substrate. The final thickness of the printed wet film varies from around ten to more than a hundred µm, as schematically shown in Figure 1.3 [2, 7].

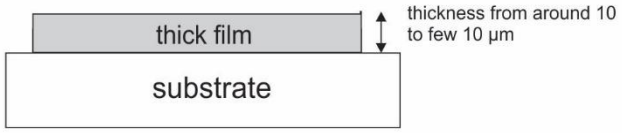


Figure 1.3: Scheme of the thick-film cros-section with defined lines and variation in thickness.

The screen defines the pattern and also the amount of the ink that is deposited. The most common screens are made from a metallic frame, usually aluminium, onto which a woven mesh is stretched. Some important properties of the mesh are size and density of the strands (usually expressed in lines per inch) and the material. The material should be flexible enough to be able to get in close contact with the substrate. At the same time it should be resilient enough to be refunded in the original position after printing. The most common material used for mesh is stainless steel. The main advantages in comparison to other materials (polyester and nylon) are high standard of line definition and also good control of ink deposition. The size and density of the strands regulates with the amount of ink deposited and consequently regulates the thickness of the printed film [2].

Finally, the thickness is influenced by the ink's rheology (described in the next chapter) and the amount of the solids load in the ink [2, 7]. The thickness increases with the increase

of the solids load. The high solids load is also required for achieving high density of the fired thick-film inks [11].

At the end of the screen printing process the wet film is dried to remove solvents from the paste and fired at the optimized temperature to form a solid thick-film material [2].

1.1.2 Screen-printing ink

The screen printing requires ink with a proper flow behaviour (rheology) for printing under highly complex flow conditions. The required rheology characteristics of the ink depend on the printing stage. The ink viscosity should be low enough to flow through the mesh when the force with the squeegee is applied and high enough after printing to prevent creeping to retain its printed geometry [5, 12].

For ideal (Newtonian) fluids, the viscosity is independent of the shear and only varies with temperature. However, for the screen-printing ink deposition process viscosity must change with the pressure applied. The screen-printing ink should have specific rheological properties known as thixotropy. The liquids can be divided into two different categories based on their behaviour when the stress is applied as Newtonian and non-Newtonian fluids. Screen-printing inks are based on the properties categorized as non-Newtonian fluids, more specifically as a thixotropic fluid. They have a shear-thinning effect as shear-dependent phenomena. Shear thinning effect means that the viscosity of the ink reduces with an increase in the applied stress as seen in Figure 1.4 [13].

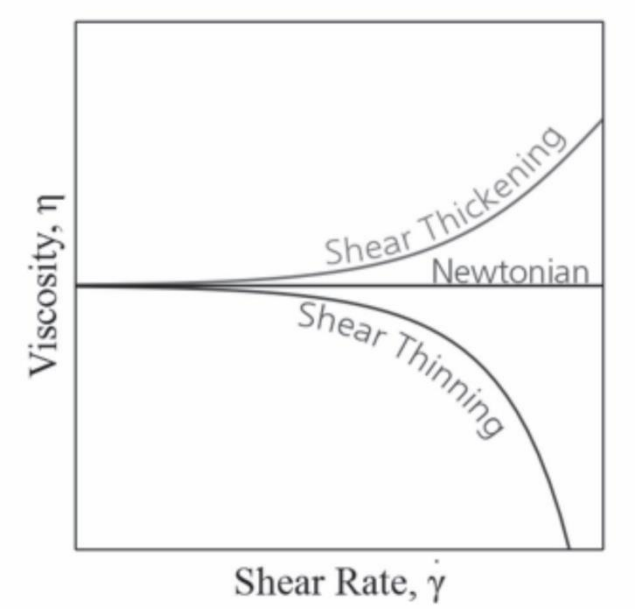


Figure 1.4: Schematic presentation of viscosity as a function of shear rate of shear thickening (rheopexy), Newtonian and shear thinning (thixotropy) fluids [14].

After shear stress is released the viscosity increases to the approximately initial value, as seen in Figure 1.5. The thixotropic fluids show a specific hysteresis after the shear is removed and viscosity recovers. The viscosity in thixotropic fluids will not recover to the initial value [13].

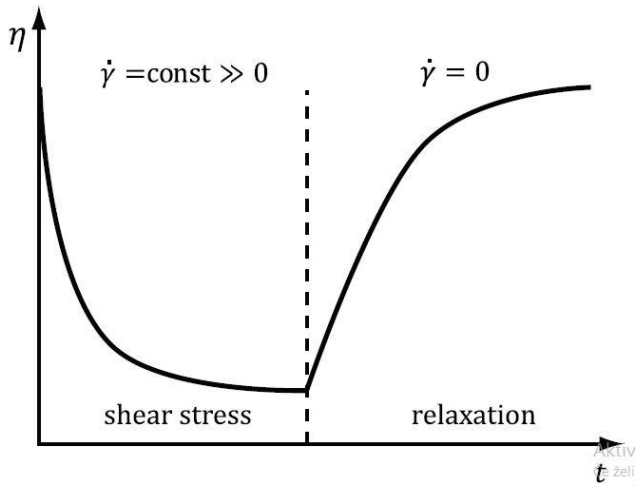


Figure 1.5: Schematic presentation of the thixotropic liquid viscosity behaviour as a function of shear rate during applied shear stress (priniting) and after shear stress is removed (relaxation) [9].

The shear-thinning effect originates from the ink composition. Inks used in the screen-printing process consist of fine particles of functional powder dispersed in organic vehicle. Functional powder is grinded, homogenized and dried to ensure uniform size distribution. The organic vehicle is composed of solvent, resin and usually surface active agent (surfactant) [2].

The solvent should be able to dry without large decrease in viscosity to prevent creeping of the ink. On the other hand, the solvent should not be volatile at the printing temperature. Usually (2-(2-butoxyethxy)ethyl) acetate and α-terpineol are used as solvents [2]. Essential for the characteristics of the organic vehicle is the resin, which acts as a binder. The resin connects with the powder particles by the active end groups giving vehicle the thixotropic properties. In most organic vehicles is used as a resin Ethyl cellulose. [2] One or more surfactants are normally included to ensure dispersion of the powder particles and adequate wetting of the substrate. Chemicals such as 2-Furoic acid, 1,2-dihydroxybenzene, 1-heksadecanol etc. are used as surfactants [15]. The proportion of components in the organic vehicle is adjusted according to the type of particles and the required printing rheological properties of the ink.

In the screen printing ink inorganic particles (in my case functional ceramic powder) act as an inorganic linker and are connected by the elastically active chains with sticky end groups (in my case ethyl-cellulose (EC)) to form a cross-linked network. The more structured the ink network, the higher the viscosity.

The low shear causes stretching of the elastically active chains and reduces the interactions between the particles and the polymer binder. This results in free or dangling chains, producing intermolecular associations of ionic groups and coagulation of the free chains, which results in macro-agglomerates.

The high shear that occurs during the passing of the ink through the mesh arranges the macro-agglomerates in the direction of the shear. This lowers the viscosity of the ink and allows it to flow through the mesh and fill the unevenness from the screen wires.

After the shear is released, the free and dangling chains from the macro-agglomerates produce more junctions between the macro-agglomerates and consequently form a structured network that causes an increase in the viscosity, which in turn results in a stiff structure of the film being formed. After deposition the levelling should be slow enough to eliminate mesh imprints and quick enough to eliminate the creeping defect [5, 16, 17, 18]. The explanations are based on the transient network theory (TNT) developed by Tanaka and Edwards [18], the application of which to the screen-printing inks was demonstrated by Sanson et al. [16].

1.1.3 Rheology tests

The properties of the printable inks are determined by the rheology tests. The rheology experiments reveal information about flow behaviour of the liquids while the shear forces are applied (during printing) and after the shear forces are released (during the levelling stage). The screen-printing ink is subjected to a wide range of shear rates during and after screen printing (see Figure 1.6). The estimated flow conditions during screen printing are expressed with shear rates and are ranging from 0.01-0.1 s^{-1} during stirring and up to around 1000 s^{-1} when the ink is penetrating through the mesh [5, 19].

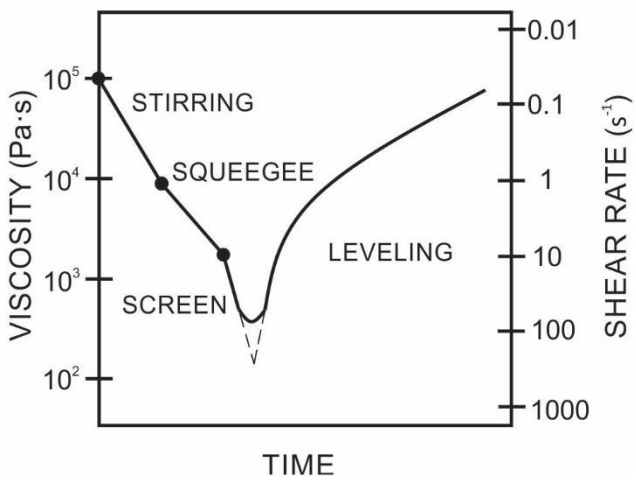


Figure 1.6: Graph showing shear rates and viscosity change during the printing stages: stirring of the ink, squeegee pressure, flow of the ink through the screen, leveling of the ink [19].

The rheology of the screen-printing ink is characterized with a rotational viscometer using two tests: the flow test (FT) [4, 5, 13, 17] and the screen-printing simulation test (SST). It is essential that due to a complex nature of screen-printing ink the viscosity tests are made in a wide range of shear rates.

The most common characterization method for the estimation of the viscosity is the FT where we change shear stress and measure change in the viscosity in the range from 0.01 s^{-1} to 1000 s^{-1}.

The SST is based on the work of Kardashian and Vellanki [17]. The shear rate applied in the first shear rate regime was 0.01 s^{-1} and is simulating quasi-static conditions. In the second applied shear rate regime the shear rate is about the same as that generated by

mixing of ink before applying it to the stencil (about 10 s^{-1}), that imported by the squeegee passing over the stencil (about 100 s^{-1}) and when ink is passing through the stencil screen (about 1000 s^{-1}). The entire shear rates are applied for a very short period of time to simulate the actual screen printing. After that, the viscosity of the ink is once again measured under quasi-static conditions, simulating the conditions after the ink has been deposited onto the substrate.

The screen-printing inks have an important correlation between the rheology and printing characteristics. Careful optimization of the inks' compositions and hence rheology are needed to print a thick film with no defects due to tackiness, poor levelling, creeping or the low mechanical strength of the deposited film. The rheology of the ink can be controlled by adjusting the ink components, such as solids load, binder, solvent and surfactant.

1.2 ZnO-Based Thick-Film Varistor

ZnO-based varistors are electronic ceramic devices that are used to sense and limit transition voltage surges, without influencing the working device and without being destroyed. The ZnO varistors are formed from mixing of ZnO semiconductor powder with the powder of other oxides (Bi_2O_3, Sb_2O_3, Co_3O_4, Mn_3O_4, NiO, Cr_2O_3, …) and subjecting powder to pressing and firing techniques, which results in a polycrystalline ceramic with a unique grain-boundary interface states that contributes to a nonlinear current-voltage (*I-U)* electrical properties of the device. The varistors are technologically important because of their electrical characteristics that enable them to be used as solid state switches with large energy handling capabilities. The working range of the varistor depends on the microstructure and thickness. The varistor can operate in a wide range of voltages from a few volts to a few hundred kilovolts and over a different range of currents from microamperes to kiloamperes [20, 21, 22].

For the overvoltage and surge protection of low-voltage devices, such as microelectronic circuit boards and hybrid circuits, chip or multilayer chip varistors are used as surface-mounted devices. Thick-film varistors made by the screen-printing technique open up another possibility for the integration of varistors into hybrid circuits. The possible advantages of screen printing are miniaturization, faster and easier production of complex structures, and lower production costs. However, the screen printing of thick films has a few drawbacks, mainly because of Bi_2O_3 evaporation during firing due to a large surface-area-to-volume ratio and a strong reaction between the varistor ceramics and the substrate at the firing temperatures typical for varistor ceramics [3].

1.2.1 Electrical properties of the varistors

Zinc oxide based varistor or variable resistors are electric polycrystalline ceramic materials, which have a non-linear *I-U* response that enables a reversible switch in the case of the overvoltage. The varistors are typically connected parallel with the circuit (see Figure 1.7) [20, 21].

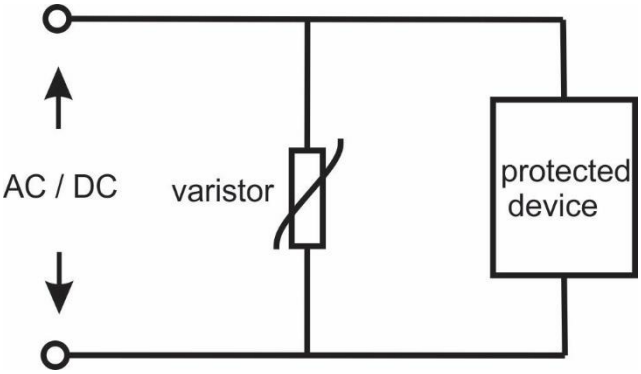


Figure 1.7: Varistor connected in AC/DC circuit for potecting a device. [23]

The primary function of a varistor is to detect and limit the overvoltage and excess current in the circuit to prevent damaging, without effecting the functioning of the working device. The varistor is under voltage all the time, but in normal conditions without overvoltage it acts as a passive element with high resistivity. The breakdown voltage of a varistor can be in a range from several kilovolts to a few volts depending on the microstructure and the thickness of varistor ceramics.

The varistor has three *I-U* dependent working regions shown in Figure 1.8.

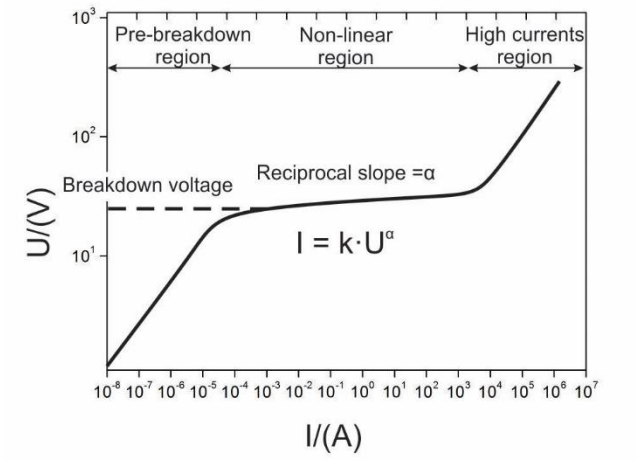


Figure 1.8: Graph showing current I versus applied voltage U for typical varistor. On the graph three working regions are shown: pre-switched, non-linear and high currents [3, 21].

During normal conditions the varistor works in the voltage range below the break down voltage; this region is called the pre-breakdown region. In this region the varistor has an ohmic *I-U* characteristic and acts like an ohmic resistor. The current that flows through the varistor in this region is called the leakage current I_L and is composed of the capacitive current (I_C) and the resistive current (I_R) determined by the impedance of the grain boundaries. For the designing of the surge suppressors resistive heating is of importance since this is responsible for the Joule heating and consequently degradation of the varistor performance. The I_L is one of the critical parameters that should be considered in the design of a varistor. The operating voltage should be at 20% above the maximum system voltage

under normal conditions and the reference leakage current is stated at 75% of the nominal breakdown voltage U_n [21, 23].

The second region of the varistor performance is a non-linear region where the varistor has a non-ohmic behaviour. The non-linear region is defined by the nominal breakdown voltage (U_N) expressed in V or the threshold voltage (U_T), i.e., the breakdown voltage per unit thickness expressed in V/mm. The U_N marks the transition from linear to nonlinear mode and is usually measured at a current density (J) 1 mA/cm^2 [24]. When the operating voltage exceeds the switch voltage, the resistance of the varistor rapidly decreases and the varistor becomes highly conductive, thereby draws excess current, usually to the ground and then as quickly as possible returns to its starting characteristics. Small increase in voltage means an increase of the passing current by several orders of magnitude. The varistor characteristics in this region are described with Eq. (1.1).

$$I = \mathrm{k}(U)^{\alpha} \tag{1.1}$$

In the equation k is constant, and α is a parameter called the non-linearity coefficient or alpha factor, which is characteristic of the varistor. The alpha factor α indicates the degree of non-linearity and is determined from the reciprocal slope of the I-U curve, which is expressed with Eq. (1.2). The higher the value of non-linearity (α), the flatter the I-U curve (lower slope) and the better the protection of the device.

$$\alpha = \frac{d \log I_2 - d\ log\ I_1}{d \log U_2 - d\ log\ U_1} \tag{1.2}$$

The alpha value reaches maximum near current density 1 mA/cm^2 and ranges from value of 20 to 100 [3, 24].

The third region is called high-voltage or upturn region. In this region the varistor again displays ohmic behaviour and is controlled by the impedance of the grains [20, 21]. For optimizing electrical properties, the influence of chemistry and microstructure on electrical properties of thick-film varistors has to be understood.

1.2.2 Microstructure and chemistry of varistor ceramics

The undoped ZnO is a non-stoichiometric n-type semiconductor exhibiting ohmic behaviour. To make a non-linear material a small amount of different metal oxides is incorporated in the ZnO. The Bi_2O_3 is one of the most essential components for forming non-linear behaviour. Some other oxides can be added to control the sintering temperature, grain growth, microstructure development and electrical properties (leakage current, break down voltage, non-linearity coefficient). Usually the varistor ceramic contains 2 – 15 mol. % of dopants, such as Bi_2O_3-Sb_2O_3-Co_3O_4-MnO-NiO-Cr_2O_3 [3, 20, 21, 23, 24].

The microstructure of such ZnO-based ceramic consists of a matrix of ZnO grains containing dissolved Co, Ni and Mn, small spinel phase grains ($Zn_7Sb_2O_{12}$) containing dissolved Co, Mn, Ni and Cr, pyrochlore phase grains ($Zn_2Bi_3Sb_3O_{14}$) discontinuously distributed along the grain boundaries and different types of intergranular layer of Bi_2O_3-

rich phases, containing Zn and other varistor dopants. The typical varistor microstructure is shown in Figure 1.9:

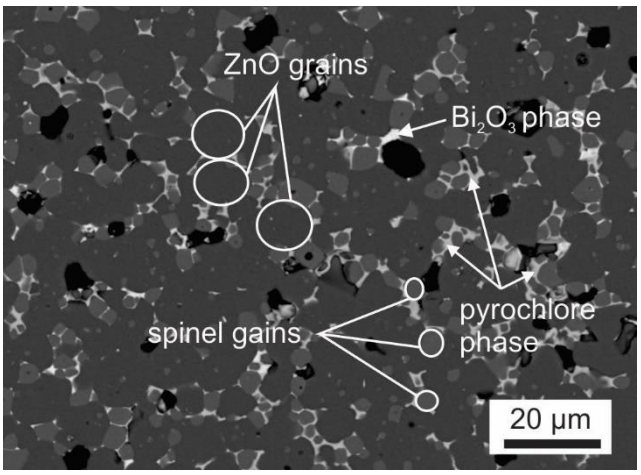


Figure 1.9: The SEM microgaph showing a varistor microstucture, which contains all phases typical for varistor ceramics: ZnO grains, spinel grains, Bi_2O_3 pahse and pyrochlore phase.

The varistor microstructure and hence electrical properties are developed from functional powder during different firing stages. The following reactions are generally accepted to occur during the firing, as described in the works of Inada [25, 26] and Arefin et al. [27].

At relatively low temperatures the formation of liquid phases takes place by melting the eutectic between ZnO and Bi_2O_3 at 735 °C. At 700-800 °C the trirutile phase ($ZnSb_2O_6$) is formed according to Eq. (1.3).

$$Sb_2O_5 + ZnO \rightarrow ZnSb_2O_6 \tag{1.3}$$

The second stage at temperatures >800° is a solid state reaction of the trirutile phase with ZnO according to Eq. (1.4) to form the spinel phase ($Zn_7Sb_2O_{12}$).

$$ZnSb_2O_6 + 6ZnO \rightarrow Zn_7Sb_2O_{12} \tag{1.4}$$

Almost simultaneously the trirutile phase at temperatures between 700 °C and 900 °C forms the pyrochlore phase ($Zn_2Bi_3Sb_3O_{14}$) according to Eq. (1.5).

$$3ZnSb_2O_6 + 3Bi_2O_3 + ZnO \rightarrow 2Zn_2Bi_3Sb_3O_{14} \tag{1.5}$$

During the third stage, at higher temperatures >900°C, the pyrochlore phase decomposes to the spinel phase and Bi-rich liquid phase according to Eq. (1.6).

$$2Zn_2Bi_3Sb_3O_{14} + 17ZnO \leftrightarrow 3Zn_7Sb_2O_{12} + 3Bi_2O_3 \tag{1.6}$$

Two important processes occur at this stage, which have a large influence on non-linearity and breakdown voltage. First dopant ions such as Co, Ni and Mn diffuse into ZnO grains and provide uniform dopant distribution. Ions of Co, Ni and Mn are known to

increase electrical conductivity and *I-U* nonlinearity. Their valence may change near the vicinity of the grain boundary, especially with local charges in oxygen partial pressure [23, 28].

The other process that occurs at this stage is liquid phase densification due to the formation of a Bi_2O_3-rich liquid phase. According to the equations of formation and decomposition of the pyrochlore phase in which the amount of Sb_2O_3 is equal to Bi_2O_3, the Sb_2O_3-to-Bi_2O_3 (Sb/Bi) ratio affects the temperature at which Bi_2O_3-rich liquid phase is formed in the system. At Sb/Bi < 1, the Bi_2O_3 in excess (not bounded into the pyrochlore phase) results in the formation of liquid phase already at 735 °C. However, for Sb/Bi ≥ 1 all Bi_2O_3 is bounded into the pyrochlore phase (Eq. (1.5)) and the liquid phase is formed only after the decomposition of the pyrochlore phase at temperature above 900 °C (Eq. (1.6)) [29].

The liquid phase strongly affects grain growth depending also on the temperature and duration of the firing process. Grain growth is also affected by the Sb_2O_3 in which two mechanisms are involved. The first and most important mechanism is that added Sb_2O_3 determines the nucleation of the inversion-boundaries (IB) in the ZnO grains. The grains containing IB are growing faster at the expense of the normal grains. When two of the grains containing IB impinge on each other, growth is reduced [30]. The second mechanism is Sb_2O_3 forming the spinel ($Zn_7Sb_2O_{12}$) phase. Grains of the spinel phase are segregated and located discontinuously at the grain boundaries; however, they can reduce grain boundary mobility by Zener pinning effect hindering growth of ZnO grains. Both mechanisms affect grain growth and hence the break-down voltage of ceramics [26].

The grain size of varistor ceramics is important because it defines break down voltage. The break down voltage U_N of the varistor body (thickness L) is proportional to the number of barriers between the electrodes, and therefore inversely proportional to the average grain size d, according to (1.7). The experimental break down voltage U_{NB} per barrier is typically in the range 3 to 3.5 V [3].

$$U_N = U_{NB} L/d \tag{1.7}$$

The last stage is cooling. At the slow cooling from sintering temperatures to about 900 °C the pyrochlore phase can form again in accordance with Eq. (1.6).

Bi_2O_3-rich phase forms a continuous intergranular crystalline phase that surrounds ZnO grains. The Bi_2O_3 segregated at the grain boundaries can accommodate other varistor dopants like Sb, Mn and Co, which is essential for the non-linear behaviour creating defects that act as electron traps, thus forming an electrostatic barrier at the grain boundaries, also known as the Schottky barrier. At voltages below breakdown voltage U_n only a small current flows through, called the leakage current. Those barriers become highly conductive when the applied voltage exceeds U_n and most accepted mechanisms for electron transport across those barriers are thermionic emission and tunnelling [21, 23, 25, 26, 29].

Typically, varistor ceramic is sintered at temperatures in the range from 1100 °C to 1300 °C for several hours. Such sintering conditions represent a challenge in the case of thick-film varistor ceramics, the firing of which is preferred at much lower temperatures below 1000 °C for less than 30 minutes [3]. Sintering at a temperature above 1100 °C is important to ensure complete decomposition of the pyrochlore phase in accordance with

Eq. (1.6) and the formation of optimal amount of the Bi_2O_3-rich liquid phase for the starting composition. The upper firing temperature of 1300 °C is set mostly due to excessive evaporation of Bi_2O_3 and also sublimation of ZnO [31, 32, 33, 34]. The problems and challenges of the optimizing thick-film varistors are described in the next chapter.

1.2.3 Development of thick-film varistors

Usually sintering temperature in hybrid circuit technology is required below 1000 °C, hence, processing compromises for forming a stable thick-film varistor are needed. On one hand firing temperature should be high enough to ensure uniform distribution of varistor dopants, densification, grain growth and microstructure development, all essential for good varistor characteristics. And on the other hand firing temperature should be low enough to avoid risk of interactions between the materials (varistor ceramics, substrate, electrodes) with formation of the reaction layer and evaporation of volatile components [3]. The most critical is evaporation of Bi_2O_3, which can result in increased porosity, poor microstructure development and reduced grain boundary nonlinearity. The determination role on the bismuth oxide evaporation also plays surface area-to-volume ratio (A/V) of the green ceramics. In the thick-film varistors A/V ratio is much larger than in bulk ceramics. Larger surface area of the printed film is exposed to the environment and the vaporization is higher [31, 32].

Different strategies were used to optimize the thick-film varistor fired at temperatures below 1000 °C. De la Rubia et al. [6, 12] used previously synthesised spinel and $Bi_{38}ZnO_{58}$ phases, which was mixed with the varistor powder and further fired at different temperatures. Authors reported lower Bi_2O_3 evaporation and α values up to 20 at peak firing temperature 900 °C. Mis et al. [35] used varistor powder with 1 mol. % of Bi_2O_3 addition. Also, for development of thick-film varistors different substrates were used (alumina and LTCC), different electrodes (Pd/Ag, Au a Pt) and different peak firing temperature (850 °C or 950 °C for 10 min.). Reported α values were up to 23 having platinum electrodes, peak firing temperature 850 °C and printed on LTCC. Lucat et al. [36] studied different electrodes (Pt and Ag – containing Bi_2O_3, Pt, Ag and sputtered Pt) used in thick-film varistors fired at 850 °C for 15 min., and reported α values around 5, with the exception of extremely high α of 43 when using Ag electrode containing Bi_2O_3.

However, at such low firing temperatures the densification of the thick film and the development of the microstructure, required for good *I-U* characteristics, are hindered, even more so if the green density of the screen-printed film is low [6, 36, 37, 38]. The problem of densification causing weak grain boundaries and high porosity is clearly evident in the microstructure of the thick-film varistors reported in previous studies, which did not take into account the concentration of the solids load in the screen-printing ink as a key element for obtaining a high green density of the printed film [6, 12, 36, 39]. The high porosity of the films and the hindered microstructure development can cause localization of the electrical current and, consequently, unequal heating and degradation of the varistor [21, 40, 41, 42].

None of the above articles reported a study of the optimization in the varistor composition in regard to the Bi_2O_3 and Sb_2O_3 addition and the Sb_2O_3-to-Bi_2O_3 (Sb/Bi) ratio.

1.3 Thick-Film Thermoelectric Microgenerators

1.3.1 Thermoelectricity

The thermoelectricity among other things enables also direct conversion of the heat into electricity by exploiting the Seebeck effect. Hence, the Seebeck effect has gained much interest in the past 20 years as the fundamental principle enabling the harvesting of the waste heat by direct conversion into electric energy. The Seebeck effects result in the thermoelectric material exposed to a temperature gradient into electrical potential; the mobile charge carriers at the hot end tend to diffuse to the cold end and the build-up of charge carriers results in a net charge at the cold end, producing voltage (i.e. electrostatic potential). Thus, an equilibrium is reached between the chemical potential for diffusion and the electrostatic repulsion due to the build-up of charge. This property is known as the Seebeck effect or thermopower and can be calculated from the voltage difference dU and the temperature gradient dT, according to the equation [9]:

$$S = \frac{dU}{dT} \tag{1.8}$$

The performance of TE materials is usually described by the dimensionless figure of merit (zT), which depends on the Seebeck coefficient (S), electrical conductivity (σ), thermal conductivity (λ) and temperature (T), according to the equation:

$$zT = \frac{S^2\sigma}{\lambda}T \tag{1.9}$$

In the thick-film thermoelectrics thermal conductivity (λ) is hard to determine due to the close contact of TE materials and substrate. Hence, a performance of the TE material is usually expressed by the power factor (P), which is the numerator $S^2\sigma$ in equation (1.9) [43].

For reasonable high zT value TE material should have high S and σ and low λ. TE materials with good performance are usually doped semiconductors. In semiconductors, charge carrier concentration (electrons or electrons holes) can be increased with proper doping. It increases σ and unfortunately, however, typically also decreases S and increases λ, which is both contradicting for an increase of the zT value according to Eq. (1.9), as seen also in Figure 1.10.

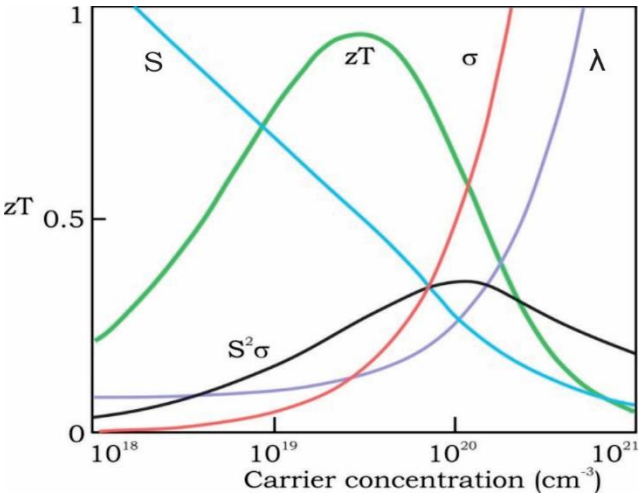


Figure 1.10: Schematic presentation of maximized zT and P value for doped semiconductors, which are directly affected by the S, σ and λ as a function of carrier concentration [44].

The influence of the electron carrier concentration on the Seebeck coefficient is defined by:

$$S = \frac{8\pi^2 k_B^2}{3eh^2} m^* T \left(\frac{\pi}{3n}\right)^{2/3} \tag{1.10}$$

where h is the Planck's constant, k is the Boltzmann's constant, n is the carrier concentration and m^* is the effective mass of the carrier. From the equation it is evident that with increasing the carrier concentration the Seebeck coefficient decreases.

The electrical conductivity (σ) is influenced by carrier concentration n, through the carrier mobility μ:

$$\sigma = ne\mu \tag{1.11}$$

It is obvious that with higher carrier concentration electrical conductivity increases. With an increase of the electron carrier concentration the thermal conductivity also increases. The thermal conductivity in semiconductors consists of two sources. One source of thermal conductivity are electron carriers, such as electrons and holes, transporting the heat. Such mechanism is referred to as electronic thermal conductivity. The other source are phonons, with different wavelengths and mean free paths, transporting the heat through the lattice. Such mechanism is referred to as lattice thermal conductivity. For achieving low thermal conductivity, the TE materials should have lower and yet optimal electron carrier concentration for sufficiently high electrical conductivity and a crystalline lattice structure with elements for enhanced photon scattering [9, 44].

As seen from Figure 1.10 and Equations (1.10) and (1.11), a compromise among values of the TE parameters should be made to gain the highest possible σ for still high S and low λ, and to achieve the maximum value for the zT. Such material should have carrier concentration somewhere between 10^{19} and 10^{21} carriers per cm^3, depending on the material system [9].

The TE semiconducting materials are defined by the majority charge carriers. For exploiting of the heat energy usually two types of TE materials are required, the *p*-type and the *n*-type. In the *p*-type TE the majority carriers are electron holes. In the *n*-type TE the majority carriers are electrons. The thermal diffusion accumulates electron holes on the hot side and hence the Seebeck coefficient for *p*-type TE is positive and accumulates electrons at the cold side and the Seebeck coefficient for *n*-type TE is negative. The *p*-type and the *n*-type materials connected in series are called a thermo-electric module – a thermoelectric generator (TEG) (Figure 1.11).

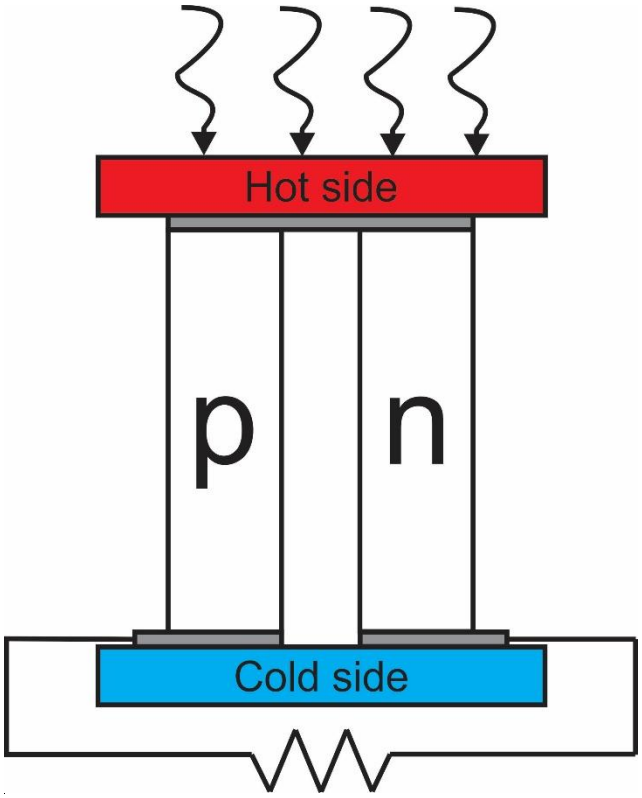


Figure 1.11: Schematic view of a thermoelectric module conecting the *p*-type and the *n*-type material [44].

When the temperature gradient is applied to TEG, thermoelectric voltage is created. TEGs have no moving parts and do not need maintenance, which are important characteristics for long term use [9].

1.3.2 Thermoelectric materials

The TE materials can be in general divided into three groups regarding the operation temperature, as seen in Figure 1.12.

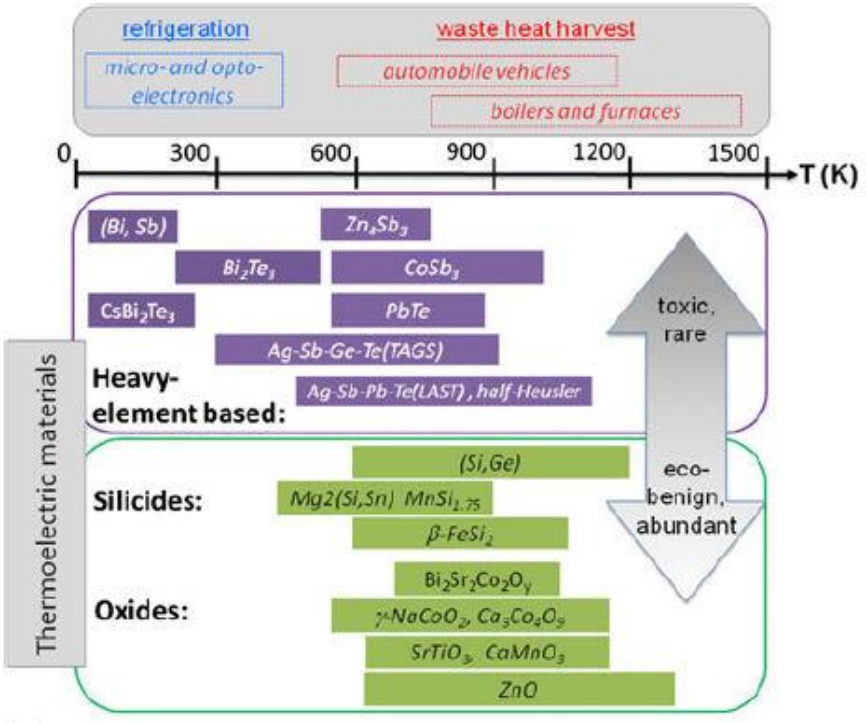


Figure 1.12: Schematic presentation of the TE materials according to the abundance of the elements in their composition, environment impact and the temperature range of their application [45].

The TE materials with the largest achieved zT value for each temperature group are: i) at low temperatures from zero to about 180 °C (450 K) the Bi-Te-based TE metallic alloys; ii) in the temperature range from 270 °C to 650 °C the PbTe-based TE materials and at the high temperatures above 650 °C the SiGe-based TE materials. A zT value larger than one is usually considered to be needed for practical application and many of those compounds exceed that value [44]. However, the toxicity, stability (especially at high temperatures) and limited natural resources of elements in those compounds are an issue for their widespread applications [46, 47].

For TEG operation at higher temperatures in the range above 400 °C and up to 1000 °C TE oxide materials have some advantages in comparison to the classical thermoelectric alloys. Oxide TE are resistant to heat degradation, melting and oxidation, composed of non-toxic and relatively abundant elements and hence cheaper; however, their TE characteristics are inferior to the classical TE alloys and much below the one required for application [44, 47, 48, 49]. Hence, significant increase of their zT is required.

For the p-type oxide TE materials layered cobaltites, such as Na_xCoO_2 and $Ca_3Co_4O_9$, are mostly studied, and also some other oxides ($LaCoO_3$-, $LaCuO_4$- and $CuAlO_2$-based ceramics). While the Na_xCoO_2 is highly sensitive to humidity and unstable at temperatures above 800 °C, the $Ca_3Co_4O_9$ is highly stable and also has very promising TE characteristics of high S and low λ with prospects for further enhancement [46]. The thermoelectric properties of the $Ca_3Co_4O_9$ originate from the misfit layered crystal structure, shown in Figure 1.13.

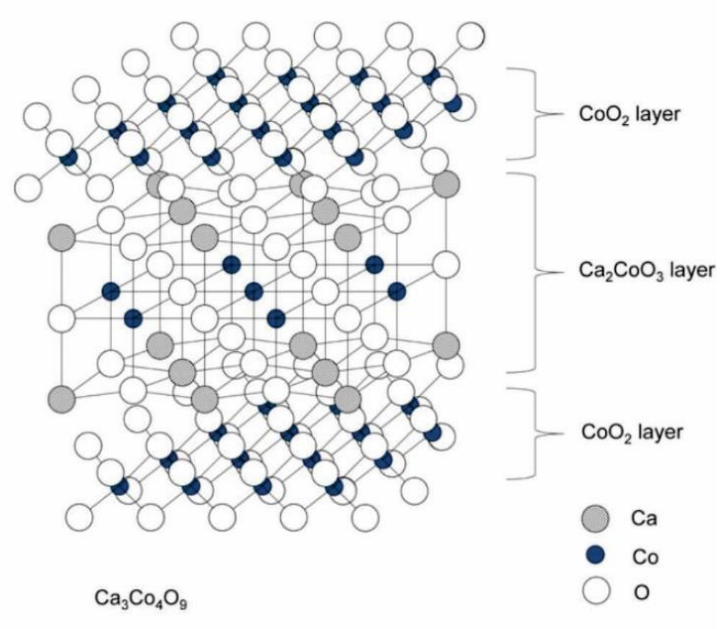


Figure 1.13: The crystal structure of $Ca_3Co_4O_9$ consists of two sublattice structures, the CoO_2 layers and the Ca_2CoO_3 layers [46].

The $Ca_3Co_4O_9$ is a layered cobalt oxide whose structure consists of two subsystems, $[CaCo_2O_3]$ and $[CoO_2]$. The $[CaCo_2O_3]$ subsystem is a distorted rock salt type, which disrupts the heat transfer by the phonon scattering and serves as a charge carrier reservoir. The $[CoO_2]$ subsystem is a CdI_2-type which serves as a *p*-type electronic conduction path. Both sublattices are alternatively stacking along the c-axis [50]. Bulk layered cobalt oxides show $P < 0.2$ mW/mK^2, S higher than 100 μ V/K and electrical resistivity lower than 15 mΩ·cm at temperatures up to 700 °C [51, 52, 53].

As the most promising *n*-type TE oxides are reported $CaMnO_3$–, $SrTiO_3$– and $(ZnO)_kIn_2O_3$–based ceramic materials. However, the $(ZnO)_kIn_2O_3$ system provides the most stable thermoelectric properties at high temperatures [46]. Among the $(ZnO)_kIn_2O_3$ homologous phases the $(ZnO)_5In_2O_3$ phase has the highest zT value due to the highest density of highly ordered planar defects (Fig. 1.14), which contributes to high σ and low λ.

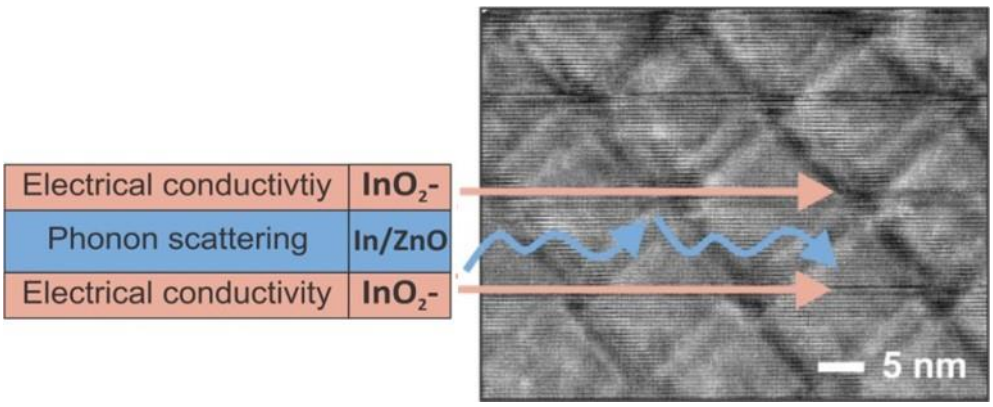


Figure 1.14: TEM micrograph showing a $(ZnO)_kIn_2O_3$ superlattice structure with aranged planar defects of InO_2^- and »zig-zag« ZnO/In defects in between.

The $(ZnO)_5In_2O_3$ has a superlattice structure composed of planar InO_2^- defects and zig-zag" type ZnO/In defects in between the planar ones. The InO_2- defects are governing the electrical conductivity. The ZnO/In defects in between the planar ones are causing additional phonon scattering for the reduced thermal conductivity. The $(ZnO)_5In_2O_3$ ceramics show $P < 0.16$ mW/mK^2, S higher than – 200 μ V/K and electrical resistivity, σ, lower than 10 mΩ·cm at temperatures up to 800 °C [54].

I focused my study on the *p*-type $Ca_3Co_4O_9$ and the *n*-type $(ZnO)_5In_2O_3$, both being among the most promising oxide TE materials of their type and also widely studied [49]. However, the described TE oxide materials have some drawbacks to be solved, especially those related to their poor electrical conductivity and consequently low power factor P, which is in general still much too low for the effective use in energy harvesting and also much lower in comparison with the classical TE materials. The aim of this thesis is focused on the other drawback, which is related to the high cost of making TEGs and hence high cost per watt. An inexpensive solution would be a huge step towards the mass production of TEGs.

1.3.3 Development of the thick-film thermoelectric generators

The thick-film technology gives broad opportunities for development of thermoelectric devices and their miniaturisation for integration into thermal management packages and low power, high voltage electrical power source systems, which are interesting for various space and terrestrial applications. The solid-state micro-coolers and micro-generators offer solutions for miniaturization of electronic components and advanced systems, which integrate the functions of sense, compute, actuate, control, communicate and power in a single device [55, 56, 57, 58, 59]. In addition, the preparation of a thick-film TEG by screen printing, which is a simple and cost effective technique, brings a solution for lowering the expenses of the manufacturing process [9, 60].

Authors Markowski et al. [10, 61] described in their work some of the structures of TE microgenerators with planar-circular and tree-dimensional structures with higher output power than previously described. The structure of a TE microgenerator, based on their work on thermocouples made from germanium doped semiconductors, is shown in Figure 1.15.

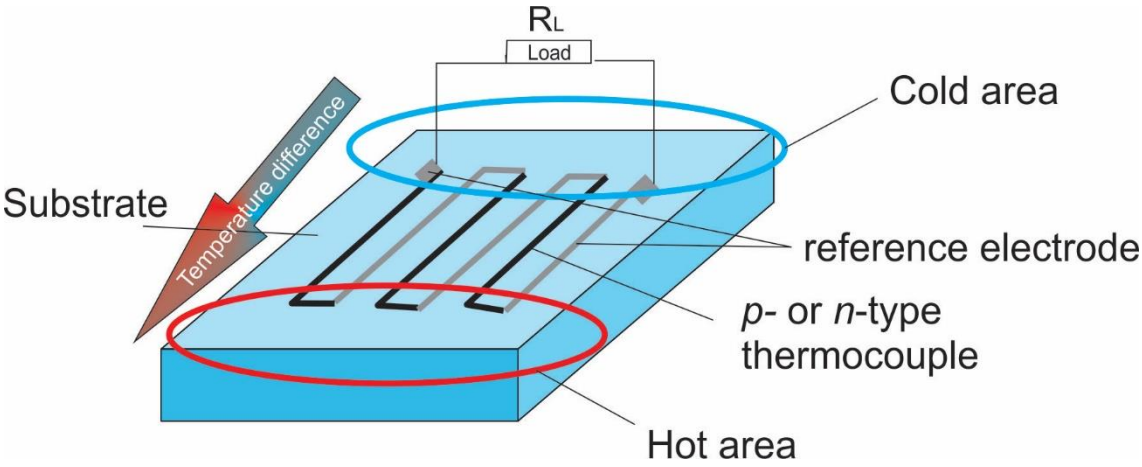


Figure 1.15: Schematic view of a thick-film microgenerator made from *p*- or *n*-type thermocouples [62].

The authors Nong et al. have investigated the thick-film high-temperature thermoelectric properties of $Ca_3Co_4O_9$ with Ag addition made by the screen-printing. The study showed that by reducing the thickness of the TE material, the maximum amount of heat through the sample at a given temperature difference is noticeably increased, resulting in a high heat flux and a low thermal resistance in the thin direction of the TE material [43]. The problem was high porosity of the fired films, consequently higher resistivity of the thick films in comparison to the bulk material. This problem could be reduced by the preparation of screen printing inks with high solids load, which enables better connection among the grains and hence better densification during firing.

The TE microgenerator based on the *n*-type $(ZnO)_5In_2O_3$ has, according to my knowledge, not yet been reported.

This thesis describes the development of the thick-film oxide-based thermoelectric device based on the *p*-type $Ca_3Co_4O_9$ and the *n*-type $(ZnO)_5In_2O_3$, made with screen printing of the high solids load screen-printing inks. The main challenges associated with microgenerator fabrication are also discussed.

Chapter 2

Aims and Hypothesis

2.1 Description of the Problem

The screen-printing is one of the most important and mature methods used in thick-film technology for manufacturing of the thick-film components in the hybrid circuits. The manufacturing advantages of thick films made with screen printing are miniaturization, faster and easier production of complex structures and lower production cost.

However, screen printing still has some drawbacks, especially when forming thick-film electronic ceramics. The first general problem is low green density of the thick film, which after firing results in higher porosity. The screen-printing ink with high solids load could significantly decrease the porosity and consequently increase the density of the fired thick film. The preparation of high solids load inks is not a straight forward process and should include careful optimization with regard to different compositions and the components. The high solids load screen-printing ink should have been optimized to have a proper flow behaviour (rheology) for forming quality printed films, whit no defects.

The second general problem is excessive volatilization of the volatile components and reaction of the active powder with electrodes and substrate. This problem is connected with high area-to-volume ratio of the printed thick-film in comparison to the bulk ceramic.

In hybrid circuits the typically used firing conditions are temperatures around 900 °C and short firing times at peak temperature from 2 to 30 minutes, typically about 15 minutes. In contrast, for manufacturing bulk varistors, typical sintering temperature and times are around 1200 °C and several hours, respectively. Hence, firing conditions typical for hybrid-circuits are harsh for achieving proper microstructure development of varistor ceramic and required electrical properties. However, low firing temperatures and short firing times are an advantage in preventing excessive evaporation of the Bi_2O_3 at large area-to-volume (A/V) ratio in thick-film varistors. The influence of Bi_2O_3 amount and the Sb_2O_3-to-Bi_2O_3 (Sb/Bi) ratio was extensively studied in the bulk varistor ceramics; both composition parameters significantly affect the temperature of formation and the amount of the Bi_2O_3-rich liquid phase, which contributes to uniform distribution of varistor dopants and enhances the microstructure development. It could be expected that both compositional parameters strongly influence also the microstructure development in thick-film varistor ceramics. However, with important differences in comparison to the bulk ceramics; they originate from specific geometrical parameters of thick-films with large area-to-volume (A/V) ratio and being also in direct contact with the substrate and the electrode

during the firing process. Nevertheless, the Bi_2O_3 amount and the Sb/Bi ratio as important parameters of varistor powder mixture composition have mostly been neglected so far in the development of thick-film varistors. In addition, the influence of the peak firing temperature on the microstructure development and electrical properties should also be considered.

For energy harvesting at high temperatures oxide-based thermoelectric materials have gained great attention, because of the possibility for direct conversion of the waste heat into electrical energy. In comparison to the classical TE alloys they are made from non-toxic and abundance elements and are stable in air (i.e. oxidizing atmosphere) at high temperatures. However, the high temperature oxide-based thermoelectric generators (TEMs) are not yet used, mainly because of low conversion efficiency of the materials and high price per watt. The screen printing opens up the possibility to manufacture low cost thermoelectric microgenerators TEMGs. The most promising oxide-based materials for producing TEMG are $Ca_3Co_4O_9$ for *p*-type TEMG and $(ZnO)_5In_2O_3$ for *n*-type TEMG.

For optimal microstructure development of the thick-film thermoelectrics to have similar TE characteristics as bulk TE materials, high green density of thick-films is required and can be achieved by using the screen-printing ink with high solids load content.

Further optimization of both $Ca_3Co_4O_9$ and $(ZnO)_5In_2O_3$ TE parameters (S, σ and P) can be achieved by variation in the firing temperature. The optimal firing temperature should be high enough to ensure enhanced densification and microstructure development for proper grain connectivity. On the other hand, the temperature should be low enough to prevent vaporization of the volatile components and excessive interaction with the substrate and the electrodes.

2.2 Aims and Goals of the Dissertation

The first goal of my PhD research was to examine the influence of the content of solids load in the screen-printing inks on the deposition of films on the substrate, their microstructural characteristics after firing and consequently the electrical properties. My study was based on a hypothesis that to ensure proper microstructure development in short firing time at relatively low firing temperatures high green density of the printed film is needed and can be achieved only by the use of the screen-printing inks with the highest possible solids load. The challenge was to produce high solids load screen-printing ink, with rheological properties suitable for printing. The development of the screen-printing ink was done by investigating the influence of different organic vehicles and/or the used amount of solvents, binder and surfactant. Inks with different solids load (50 wt. %, 60 wt. %, 65 wt. % and 70 wt. %) were printed and fired at the same firing regime. The quality of the green thick-films deposited on the alumina substrate was examined and the characteristics of the thick-film varistor ceramics after firing were evaluated by the microstructural analysis on the scanning electron microscope (SEM) and measurements of the current-voltage characteristics.

Once we have the formulation of the screen-printing ink with high solids load and good printing characteristics, the inks were prepared for further development of the thick-film varistors and the thick-film thermoelectrics.

Accordingly, the second goal of this thesis was studying the influence of the composition of the varistor powder mixture (i.e. composition of solids load in the ink) to enhance, under critical processing conditions of low firing temperature and short firing times, the development of proper varistor microstructure required for good current-voltage (*I-U*) characteristics. In this regard the emphasis in the composition of varistor powder was on the variation of the amount of Bi_2O_3 in the range from 0.4 to 1.8 mol. % and the Sb_2O_3-to-Bi_2O_3 (Sb/Bi) ratio in the range from 0.25 to 1.25.

The third goal of my dissertation was the development of the high temperature microgenerators (TEMG), based on $Ca_3Co_4O_9$ for *p*-type TEMG and $(ZnO)_5In_2O_3$ for *n*-type TEMG using screen printing. The TEMGs were made using the high solids load screen-printing inks to increase green density of the printed and dried thick-films. Furtherly, the use of different electrodes was also examined. The heat treatment of the thick-films was studied at different peak firing temperatures to ensure proper densification and microstructure development for enhanced TE properties. The microstructural and TE characteristics of the thick-film structures were analysed to assess the main problems of their development.

Chapter 3

Materials and Methods

3.1 Processing

3.1.1 Lists of chemicals and processing equipment

The chemicals and equipment used for experimental work are listed in Table 3.1 and Table 3.2, respectively.

Table 3.1 List of chemicals used in this work divided into three groups: thick-film technology, thick-film varistors, thick-film thermoelectrics (in alphabetic order).

Chemicals	Specification and producer	Role
	THICK-FILM TECHNOLOGY	
(2-(2-butoxyethxy) ethyl) acetate	98.4 %, Merck	Solvent
alumina substrate	Rubalit® 708 S with 96% Al_2O_3, CeramTec	Substrate
Chemical with unknown composition	CV10, ESL	Organic vehicle
Chemical with unknown composition	CV6, ESL	Organic vehicle
Chemical with unknown composition	809, ESL	Surfactant
Ethyl-cellulose	ethoxyl content 48 %, Acros Organics	Binder
α–terpineol	99.0 %, Merck	Solvent
	THICK-FILM VARISTORS	
Ag conductive ink	9912–MM, ESL	Electrode for varistor
Bi_2O_3	>99.8 %, Alfa Aesar	Varistor dopant
Co_3O_4	>99.8 %, Alfa Aesar	Varistor dopant
Cr_2O_3	>99.8 %, Alfa Aesar	Varistor dopant

Mn_3O_4	>99.8 %, Alfa Aesar	Varistor dopant
NiO	>99.8 %, Alfa Aesar	Varistor dopant
Sb_2O_3	>99.8 %, Alfa Aesar	Varistor dopant
ZnO	>99.8 %, Pharma 4, Grillo Zinkoxid GmbH	The main component of varistor ceramics
	THICK-FILM THERMOELECTRICS	
$CaCO_3$	99.5 %, Alfa Aesar	Reagent for preparation of Ca349 phase
Co_3O_4	99.7 %, Alfa Aesar	Reagent for preparation of Ca349 phase
In_2O_3	99.9 %, Alfa Aesar	Reagent for preparation of Z5I phase
Pd/Ag conductive ink	6146, DuPont	Electrode for Ca349-based TEG
Pt conductive ink	9141, DuPont	Electrode for Z5I-based TEG
ZnO	>99.8 %, Pharma 4, Grillo Zinkoxid GmbH	Reagent for preparation of Z5I phase

Table 3.2: List of equipment for processing and characterization of the thick-film (in alphabetic order).

Item	Specification and manufacturer	Role
	EQUIPMENT FOR THICK-FILM PROCESSING	
Belt furnace	QA 41-6-54, BTU	Firing of the thick-film varistors
Chamber furnace	HTC 03/16, Nabertherm	Firing of the thick-film thermoelectrics
Drying oven	Kambic	Drying of the thick-films
Laser-scattering particle size distribution analyser	LA–920, Horiba	Determination of the powder particle size after milling
Planetary mill	Pulverisette, Fritsch	Homogenization and size reduction of the powder particles
Screen-printer	1202, DEK	Preparation of the thick films
Three-roll mill	Tripple Roller Mill 50, EXAKT	Preparation of the screen-printing ink

EQUIPMENT FOR THICK-FILM CHARACTERIZATION		
Coating system	Model 682, PECS	Sputtering of the carbon a sample prepared for microscopy
Confocal microscope	Axio CSM 700, Zeiss	Imaging of the thick-film surface
Contact profilometer	Form Talysurf Series 2, Taylor–Hobson Ltd	Imaging of the thick-film surface roughness
Electron microscope	SEM JSM–5800, JEOL	Determination of the thick-films microstructural characteristics (grain size, thickness etc.)
Keysight multimeter	34972A Data Acquisition/Switch Unit	Determination of the electrical properties of thick-film thermoelectrics
Rotational viscometer	MCR 301, Physica	Determination of rheological properties of the ink
Sputtering device	Model 682, PECS	Sputtering of samples with carbon before SEM microscopy
Voltage source meter	2410 High Voltage Digital Source Meter, Keithley	Determination of the electrical properties of thick-film varistors
X-ray powder diffraction instrument	XRD X'Pert PRO MPD	Determination of crystal phases of the Ca349 and Z5I material

3.1.2 Preparation of the screen-printing ink

The preparation of the screen-printing ink used in this work was based on the reported formulation described by Holmes and Loasby [2]. However, for the purpose of this thesis some modification of the reported formulation was required. The goal was to prepare ink with as high as possible solids load, while still having good screen-printing characteristics.

The inks were prepared on a three-roll mill (EXAKT Tripple Roller Mill 50) by mixing the following constituents: functional powder, organic vehicle made of solvent and binder, optionally, the commercially available surfactant ESL 809. The functional powder was a varistor powder mixture with the composition of 98.3 mol ZnO, 0.40 mol. % Bi_2O_3, 0.10 mol. % Sb_2O_3, 0.5 mol. % Co_3O_4, 0.1 mol. % of Mn_3O_4, 0.5 mol. % NiO and 0.1 mol. % Cr_2O_3. Functional powder was homogenised in absolute ethanol using a planetary mill at 200 rpm for 1 hour. The average particle size after homogenization d_{50} was 0.6 µm, measured with a laser-scattering particle size distribution analyser (Horiba LA–920).

The compositions of the analysed inks are presented in Table 3.3 in terms of the amounts of solids load, surfactant and binder. Compositions are further divided into three

groups based on the vehicle used: a commercial high viscosity CV10 and a commercial low viscosity CV6 (the compositions of the commercial vehicles were unknown and the producer declined to reveal them on my inquiry), and a vehicle I made using standard components ((2-(2-butoxyethxy)ethyl) acetate and α -terpineol in a ratio 1:4, respectively).

Table 3.3: Composition of the screen-printing inks in regard to solids load, binder and surfactant, divided in the three groups based on the vehicle used: commercial high- and low-viscosity vehicles CV10 and CV6 , respectively, and vehicles I prepared using standard components (2-(2-butoxyethxy)ethyl) acetate and α -terpineol in the ratio 1:4, respectively.

Ink	COMPOSITION		
	Solids load (wt. %)	Binder (wt. %)	Surfactant (wt. %)
High viscosity commercial vehicle CV10			
CV10-50WS	50	N/A*	0
CV10-50S	50	N/A*	0.6
CV10-55S	55	N/A*	0.6
CV10-60S	60	N/A*	0.6
Low viscosity commercial vehicle CV6			
CV6-60S	60	N/A*	0.6
CV6-60WS	60	N/A*	0
CV6-70WS	70	N/A*	0
Vehicles made by myself			
A-70WS	70	2.2	0
A-70S	70	2.2	0.6
B-70S	70	2.6	0.6
C-70S	70	3	0.6
B-65S	65	2.6	0.6
B-75S	75	2.6	0.6

*N/A – not applicable

Based on the commercial ESL vehicles, either the high-viscosity ESL CV10 or the low-viscosity ESL CV6, inks with a solids load from 50 to 70 wt. % were prepared, with (label S) or without (label WS) the surfactant ESL 809.

The vehicles I made were prepared from the solvents (2-(2-butoxyethxy)ethyl) acetate (98.4 %, Merck) and α -terpineol (99.0 %, Merck) in the ratio 1:4, with additions of ethyl-cellulose (EC) (ethoxyl content 48 %, Acros Organics) as a binder and ESL 809 as a surfactant. Using this vehicle, three groups of inks were investigated to analyse the effect of a variation in the concentrations of the surfactant, the binder and the solids load on their screen-printing characteristics: i) inks with a high 70 wt. % of solids load, with and without 0.6 wt. % of the surfactant (labelled as A-70S and A-70WS, respectively); ii) inks with a 70 % solids load, 0.6 wt. % of surfactant and different amounts of the binder, 2.2,

2.6 and 3.0 wt. % (labelled as A-70S, B-70S and C-70S, respectively); iii) inks containing 65, 70 and 75 wt. % of functional powder (labelled as B-65S, B-70S and B-75S, respectively), with 0.6 wt. % of surfactant and 2.6 wt. % of binder.

The composition of the screen-printing ink optimised for high solids load of 70 wt.%, labelled as B-70S, was used for further development of the thick-film varistors and the thick-film thermoelectrics.

3.1.3 Preparation of the thick-film varistors

In the process of developing the screen-printing ink with the highest possible solids load while still having proper printing characteristics, the varistor powder mixture with composition 98.3 mol ZnO, 0.40 mol. % Bi_2O_3, 0.10 mol. % Sb_2O_3, 0.5 mol. % Co_3O_4, 0.1 mol. % of Mn_3O_4, 0.5 mol. % NiO and 0.1 mol. % Cr_2O_3, was used as solids load (Chapter 3.1.2.).

In the study of further optimization of the electrical properties exploiting the composition of the varistor powder mixture, the thick-film varistors on alumina substrate were made by using the B-70S-type screen-printing inks with high solids load of 70 wt.%. The composition of the solids load (i.e. varistor powder mixture) in the paste was varied for the amount of the Bi_2O_3 from 0.4 to 1.8 mol. % and the Sb/Bi ratio from 0.25–1.25 (see Table 3.4), while the amount of other varistor dopants was fixed at 0.5 mol. % Co_3O_4, 0.1 mol. % of Mn_3O_4, 0.5 mol. % NiO and 0.1 mol. % Cr_2O_3.

Table 3.4: The compositions of the varistor powder mixtures (i.e. solids load) in the screen-printed inks, varied for the amount of added Bi_2O_3 and the Sb_2O_3-to-Bi_2O_3 (Sb/Bi) ratio at the same amount of other varistor dopants.

Varistor	Bi_2O_3 mol. %	Sb/Bi ratio
DV1	0.8	0.25
DV2	0.8	0.8
DV3	0.8	1.25
DV4	0.4	0.8
DV5	1.6	0.8
DV6	1.8	0.8

The thick-film varistors were printed on an alumina substrate (Rubalit® 708 S with 96% Al2O3, CeramTec) in a sandwich configuration (Figure 3.1). First, a silver electrode (ESL, 9912–MM) was printed, then five layers of varistor film and finally an upper silver electrode (ESL, 9912–MM). Every layer was dried in an oven at 130 °C for 15 min before the next layer was applied.

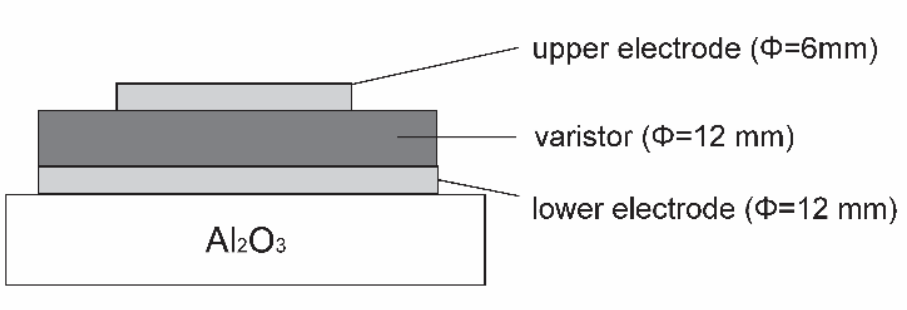


Figure 3.1: Sandwich configuration of the thick-film varistor [63].

The printed and dried samples were fired in a conventional belt furnace at a peak firing temperature of 900 °C and firing time 15 min., 30 min. and 60 min.

3.1.4 Preparation of the thick-film thermoelectrics

The p-type $Ca_3Co_4O_9$ (Ca349) and n-type $(ZnO)_5In_2O_3$ (Z5I) TE materials were prepared from starting powder mixtures by the classical ceramic solid-state synthesis.

For the $Ca_3Co_4O_9$ (Ca349), a stoichiometric ratio of reagent-grade $CaCO_3$ (Alfa Aesar, 99.5 % metals basis) and Co_3O_4 (Alfa Aesar, 99.7 % metals basis) powders was mixed with absolute ethanol in an agate mortar. The resulting homogenized mixture was dried, pressed into pellets and sintered at 760 °C for 12 hours. The calcinated pellets were grinded for additional homogenisation, pressed into pellets and sintered at 920 °C for 20 hours.

For the Z5I stoichiometric ratios of reagent-grade ZnO (Grillo Zink oxide, GmbH, Pharma 4, > 99.9 %) and In_2O_3 (Alfa Aesar, 99.9 % metals basis, 325-mesh powder) powders were mixed with absolute ethanol in a planetary ball mill. The resulting homogenized mixture was dried for one hour at 80 °C, pressed into pellets (750 MPa) and sintered at 1200 °C for 2 hours.

The pellets of the Ca349 and Z5I were grinded into powder for further preparation of the screen-printed ink. The phase compositions of both powders, the Z5I and the Ca349, were identified using the X-ray powder diffraction (XRD X'Pert PRO MPD (Cu-K α , 2Θ range 10-80°) analysis.

The screen-printing inks were prepared in accordance with the formulation of the ink labelled as B-70S (described in Chapter 3.1.2), while as a solids load either the Ca349 powder or the Z5I powder were used in the amount of 70 wt.%.

The thick-film TE structures were printed on alumina substrates (96% Al_2O_3, thickness 0.6 mm) in two configurations (Figure 3.2 and Figure 3.3), using a DEK 1202 screen-printer through a 325-mesh screen, at a 1.5-mm snap-off distance, printing speed of 150 mm/s and a squeegee pressure of 3.5 kg.

The first configuration was made for measurements of the electrical resistivity. A film of TE material in total area of 0.9 cm^2 at line width of 0.3 mm was printed in the meander configuration, shown in Figure 3.2, with an electrode on each side.

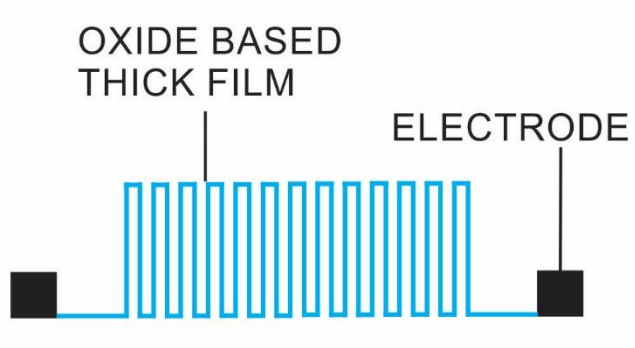


Figure 3.2: Scheme of a thick-film meander-type structure made from the oxide TE material for measurement of the electrical conductivity.

The films of the Ca349 were fired for 15 minutes at 900 °C or 920 °C and the Z5I films were fired for 15 minutes at 1250 °C, 1300 °C, 1350 °C or 1400 °C. The Pd/Ag conductive ink (DuPont 6146) was used as electrodes for the $Ca_3Co_4O_9$ system, whereas the Pt- (DuPont 9141) or the Pd/Ag-based (DuPont 6146) inks were used for the $(ZnO)_5In_2O_3$ system.

The second type of configuration was made for the measurement of the Seebeck coefficient. The TE thermopiles were screen-printed as a rectangular structure, shown in Figure 3.3 and previously described by Markowski [64].

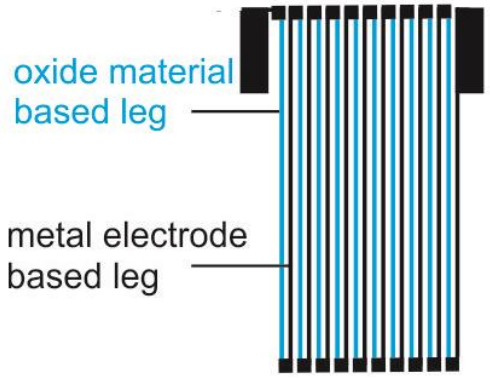


Figure 3.3: Scheme of a thick-film microgenerator made from the oxide TE material leg and the metal electrode leg [64].

The whole structure is made from ten thermocouples connected in series; each thermocouple is made from either a *p*-type or an *n*-type TE thick-film leg and a metal leg as a reference, so that in the thermopile the TE leg and the reference metal leg are sequentially exchanging. The thermopile made from ten thermocouples was made for more accurate measurement of the output voltage. For a single leg output the voltage was calculated by dividing the measured output voltage of the thermopile by ten.

First, the Pd/Ag and the Pt metal electrodes were printed and dried in an oven at 90 °C and fired in a belt furnace at temperatures up to 1000 °C. Next, three layers of the *p*-type or the *n*-type thick-film were printed. Every layer was dried in an oven at 90 °C before the application of the next layer. The printed TE leg was fired in the case of the $Ca_3Co_4O_9$ in a belt furnace for 15 minutes at 900 °C or 920 °C (just below the decomposition

temperature of the Ca349 phase at 926 °C) and in the case of the $(ZnO)_5In_2O_3$ in a conventional furnace at different temperatures above 1000 °C, the same as for the resistivity measurements (see Table 4.5).

3.2 Sample Characterization

3.2.1 Ink rheology characterization

The inks' rheological properties were determined at 25 °C using a rotational viscometer Physica MCR 301, with a cone (C25/1) and plate geometry. Two types of tests were performed to compare the properties of the prepared screen-printing inks: a flow test (FT) [4, 5, 13, 17] and a screen-printing simulation test (SST) based on reports by Lin et al. [5], Mezger [13], Kardashian and Vellanki [17], and Phair et al. [65].

In the FT the viscosity of the inks was estimated as the viscosity at shear rates ranging from 0.01 s^{-1} to 1000 s^{-1}. From the graph of viscosity vs. shear rate the zero viscosity (η_0) and infinite viscosity (η_∞) were determined. The zero viscosity (η_0) was regarded as the viscosity measured under quasi-static conditions, i.e., at a shear rate of 0.01 s^{-1}. The infinite viscosity (η_∞) was regarded as the viscosity measured at high shear rates, i.e., at 1000 s^{-1}.

In the SST the viscosity was measured in three shear-rate regimes: i) a shear rate of 0.01 s^{-1} applied for 200 s, ii) a shear rate of 1000 s^{-1} applied for 5 s and iii) a shear rate of 0.01 s^{-1} applied for 500 s. From the printing simulation test (SST) we can estimate the levelling of the ink by determining the three parameters.

The percentage of recovery R was calculated by dividing the viscosity value measured in the third regime after a time of 500 s by the viscosity value measured in the first regime at the start of the test, expressed as a percentage [17].

The rate of recovery K [65] was calculated from a derivate of the initial slope (the first three points after the stress are released) of the viscosity curves measured in the third regime of the SST test. It indicates how quickly the ink viscosity starts to recover after the stress is released. However, it does not tell us how much time it needs to reach equilibrium conditions.

The last parameter is the slope in the final stage of recovery (k) fitted from the last 200 points of the SST viscosity curve and an indication of how far the system is from reaching equilibrium conditions after the stress is released; the larger the value of k, the farther away the system is from equilibrium conditions, while for $k = 0$ the line is perfectly horizontal and the system is in equilibrium. The parameter k was determined based on the report of Sanson et al. [16] Levelling has direct effects on the roughness of the thick film [65].

3.2.2 Evaluation of the quality of the printed film

In order to evaluate the printing characteristics of the inks, one layer of thick film was printed on an alumina substrate utilizing a screen printer (Aurel C1010), a screen mesh the size of 325, a 1.5 mm snap-off, a printing speed of 150 mm/s and a squeegee pressure of 3.5 kg. The samples were dried at 130 °C for 15 min.

The obtained films were examined for printing defects on a confocal microscope (Axio CSM 700, Zeiss) and analysed using a contact profilometer (Form Talysurf Series 2, Taylor–Hobson Ltd) across different directions of the film surface with a measuring length of 10 mm, based on the report of Green et al. [66].

Based on the FT and SST measurements, the varistor ink with a high solids load was optimised. The results of the tests were compared with the observed quality of the single-layer printed film in regard to the presence of defects, such as missing defects, mesh imprints, holes and cracks determined by a visual inspection with an optical microscope [65] and a confocal microscope (Zeiss, Axio CSM 700). The defects that were observed on the surface of my printed films are shown in Figure 3.4 and present all types of defects typically related to the use of inks with unsuitable rheological characteristics for the screen printing.

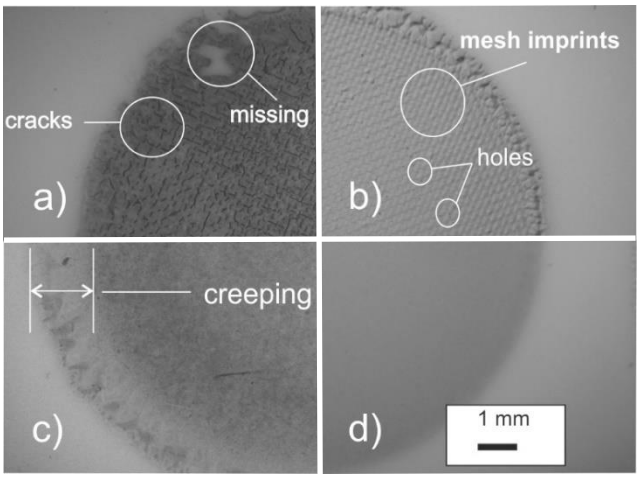


Figure 3.4: Optical micrographs showing typical defects observed in the screen-printed films prepared in the process of ink optimisation: a) cracks and missing defect, b) mesh imprints and holes, c) creping defect and d) the defect-free film with a smooth surface.

Defects, such as creeping (elongated edge of the printed films) and the levelling quality (determined by the surface-roughness factor R_a), were identified by means of the contact profilometry and a confocal microscope. A higher roughness factor means a larger deviation of the surface profile from the mean line and is in direct correlation with the mesh imprints and the missing defect. The missing effect originates from stencil clogging because of the tackiness. Using the contact profilometer it was also possible to determine the thicknesses of the dried films.

3.2.3 Characterization of electrical properties of thick-film varistors

Measurements of the voltage–current density (U-J) characteristics of the thick-film varistors were made using a Keithley 2410 High Voltage Digital Source Meter; the nominal varistor voltage U_N was measured at 1 mA/cm^2 and 10 mA/cm^2 and the leakage current was measured at 0.75 U_N(1mA/cm^2). Based on these measurements the threshold voltage U_T (V/mm) and the nonlinearity coefficient α of the thick-film varistors were determined as well.

3.2.4 Characterization of thick-film thermoelectrics

The electrical resistivity of thick-film thermoelectrics was measured using a Keysight multimeter (34972A Data Acquisition/Switch Unit) in the temperature range from room temperature to 500 °C.

The Seebeck coefficient was determined from the measured values of ΔU produced by a temperature difference ΔT, according to the equation $\Delta U = S\,\Delta T$ (Eq. (1.8)) from room temperature to 300 °C using a specially built laboratory measuring system (Figure 3.5).

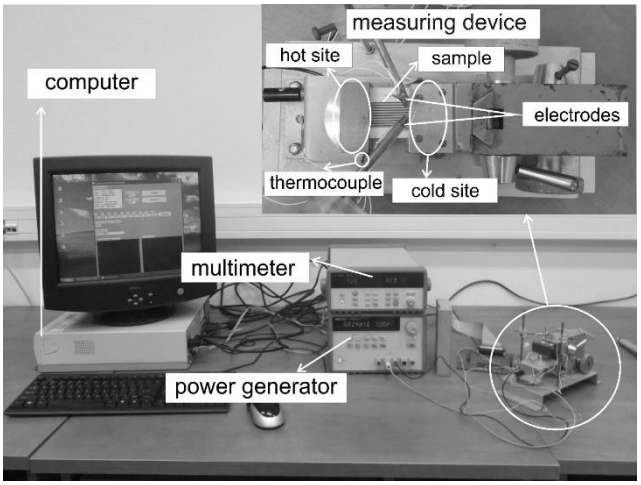


Figure 3.5: Laboratory set-up for measurements of the Seebeck coefficient (S) made from multimeter, power generator, measuring device and computer.

The samples were placed between the hot block and the cold block and the temperature on the heating block was controlled with a power generator, as shown in Figure 3.6.

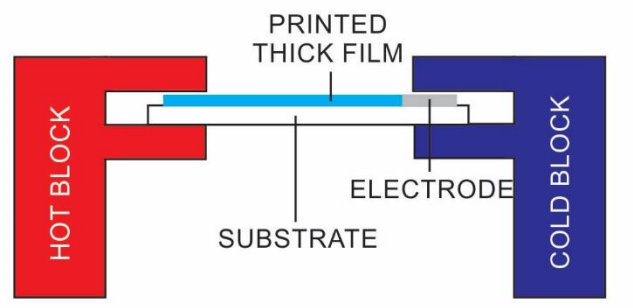


Figure 3.6: Schematic side view of oxide-based thick film placed in laboratory set up between the hot block and cold block.

The samples were connected to the multimeter at their electrodes and at different temperatures the set-points system measured the temperature of the hot and the cold sides, the resistivity and the generated voltage of the device. For the comparison with the bulk material, I measured the TE properties with the home-built Z-system. It is based on a 4-point method measured in a high vacuum in the temperature range from room temperature to 500 °C [67].

3.2.5 Methods for microstructural analysis

The microstructures of the thick-film varistors and the TE thick-films were prepared using metallographic procedures. The microstructures of the varistor and TE thick-film were investigated in the cross-section direction. In the case of the TE thick-films the surface of the films was analysed as well. To prepare the microstructure in the cross-section direction, the film was cut in half and embedded in a resin (EpoFix Kit), grinded using SiC papers and finally polished with diamond pastes (3 µm and ¼ µm). The lubricant liquid was ethanol. Afterwards the sample was cleaned in ethanol using ultrasonic bath. The microstructures were carbon coated prior to electron microscopy analysis to prevent surface charging using the sputtering system PECS (Model 682).

The microstructures of the varistor and the TE thick-films in the cross-section direction were analysed using the scanning electron microscope JEOL JSM–5800 (SEM) to evaluate the thickness, density, phase composition and distribution of phases, interaction of the thick film with substrate or electrode, grain size, size distribution and morphology, and in general microstructure development in regard to the processing conditions. In the case of the varistor ceramics the average grain size was determined using open access image analysis software Image Tool; the area of each grain on the selected SEM image is determined and the size of the grains calculated as the diameter of the circle with an equivalent area. The average grain size was determined from the measurement of 300 to 450 grains per sample. The same SEM was also used in the analysis of the surface of the TE films.

Chapter 4

Results and Discussion

4.1 Optimization of the Screen-Printing Paste

4.1.1 Inks based on commercial vehicles

The compositions of the inks made from the vehicles CV10 and CV6, their rheological properties and the results of the optical examinations (detections of certain defects) for the printed films are summarized in Table 4.1. In the case of the high viscosity vehicle CV10, the addition of 0.6 wt. % of the surfactant was essential for the preparation of the inks labelled as CV10; without any surfactant, the ink with the lowest solids load of 50 wt. % (CV10-50WS) was already too viscous to be measured or to be printed.

Table 4.1: Compositions and rheological properties of the inks, and the results of the optical examinations of the dried single-layer thick films deposited on an alumina substrate by screen printing the inks (N/A – not applicable, X – not present, ✓ – present).

Ink	COMPOSITION			RESULTS							DEFECTS			
	Solids load (wt. %)	Binder (wt.%)	Surfactant (wt. %)	η_0 (Pa·s)	η_∞ (Pa·s)	Thickness (µm)	R (%)	Rate of recovery K *(Pa)*	Slope in the final stage of recovery k *(Pa^{-1})*	R_a (µm)	Missing	Mesh imprints	Creep	Holes and cracks
High viscosity commercial vehicle CV10														
CV10-50WS	50	N/A	0	N/A	N/A	N/A	N/A	N/A	N/A	N/A	N/A	N/A	N/A	N/A
CV10-50S	50	N/A	0.6	4610	4.5	14.1	57	7.1	2.5	0.18	**X**	**X**	**X**	**X**
CV10-55S	55	N/A	0.6	6920	2.8	17.1	39	10.5	2.7	0.19	X	✓	X	X
CV10-60S	60	N/A	0.6	11700	4.5	20.7	49	28.8	4.0	0.2	✓	✓	X	X
Low viscosity commercial vehicle CV6														
CV6-60S	60	N/A	0.6	1420	2.8	14.4	143	18	4.0	0.51	X	✓	✓	X
CV6-60WS	60	N/A	0	1580	3.2	19.3	101	7	1.6	0.17	**X**	**X**	**X**	**X**
CV6-70WS	70	N/A	0	8550	4	28.6	80	60	4.1	0.39	✓	✓	X	X
Vehicles made by us														
A-70WS	70	2.2	0	7710	3.7	16.8	N/A	N/A	N/A	0.13	✓	✓	X	X
A-70S	70	2.2	0.6	1980	4.5	18.4	299	1.3	4.2	0.12	X	X	✓	X
B-70S	70	2.6	0.6	4020	3.9	23.3	140	5	1.5	0.21	**X**	**X**	**X**	**X**
C-70S	70	3	0.6	5810	1.5	23.5	86	8	2.9	0.15	X	✓	X	✓
B-65S	65	2.6	0.6	3170	4.8	22.7	83	0.3	0.01	0.13	X	X	✓	X
B-75S	75	2.6	0.6	10300	3.5	31.4	97	67	4.7	0.22	✓	✓	X	✓

The FT of the inks based on the organic vehicle CV10 shows that the zero viscosity of the ink increased with the solids load from 4610 Pa·s at 50 wt. % to 6920 Pa·s at 55 wt. %, and ends up at 11700 Pa·s for 60 wt. %, as seen in Figure 4.1.

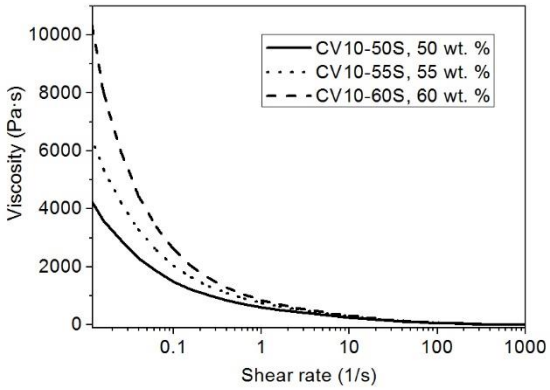


Figure 4.1: Results of the FT showing change in the viscosity vs. shear rate for the inks with different solids load CV10-50 (50 %), CV10-55 (55 %) and CV10-60 (60 %).

The zero viscosity is related to the degree of structuring of the ink by the formation of the cross-linked chains network in the suspension of a long-chain polymer and varistor powder as the inorganic cross-linker. A higher solids load means more particles that can act as an active inorganic cross-linker for enhanced network strength and consequently increase zero viscosity [16].
The results of the SST showed (Figure 4.2) that the CV10 inks have a thixotropic behaviour; their viscosity strongly decreased under shear stress and again increased once the stress was removed, however to the lower value of viscosity, which is indicated by the percentage of recovery (R) in the range between 39 and 57 %. The recovery of the viscosity is the result of a viscoelastic property of the ink and the relatively low R values were an indication of their lower elasticity due to a high solids load.

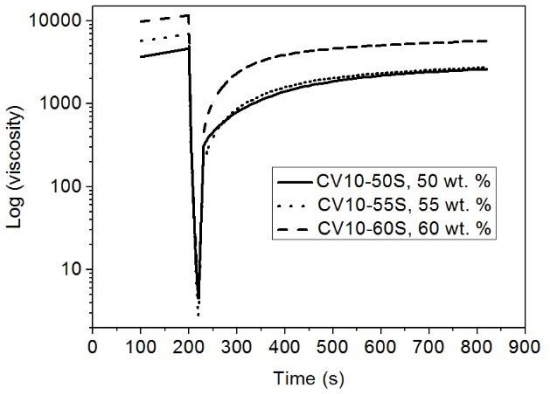


Figure 4.2: Result of the SST showing a change in the viscosity after the removal of the shear stress in inks with various amounts of solids load CV10-50 (50 wt. %), CV10-55 (55 wt. %) and CV10-60 (60 wt. %).

The optical examination with confocal microscope and contact profilometer showed no defects in the green or fired films made with the ink CV10-50S. However, on a printed film made with the ink CV10-55S, the mesh-imprint defects started to appear, which can be correlated with a high zero viscosity (η) and a relatively high rate of recovery (K). Despite the relatively low R (39 %), the recovery of the viscosity to a too high value was relatively fast (moderate $K = 10.5$ Pa) after the stress release for efficient levelling. These results can be related to the structuring in the ink with such a solids load due to a large number of particle-polymer associations [16]. With a further increase in the solids load the ink CV10-60S had an even higher viscosity. Its rate of recovery (K) was much higher showing that the ink started to recover sooner towards the high-end viscosity. In addition, according to the higher slope of viscosity curve in the final stage of recovery ($k = 4.0$ Pa^{-1}), the ink also needed more time to reach the equilibrium condition, as an indication of the higher level of structuring. All these factors contributed to the mesh imprints on the printed film becoming even more pronounced, and missing defects also appeared.

Based on the low viscosity vehicle CV6, with a lower base viscosity, I prepared an ink with a solids load of 60 wt. % and 0.6 wt. % of surfactant (CV6-60S). The FT (Figure 4.3) showed that in comparison to the CV10-60S (Figure 4.1) the zero viscosity and the infinite viscosity dropped significantly to 1420 Pa·s and 2.8 Pa·s, respectively (Table 4.1).

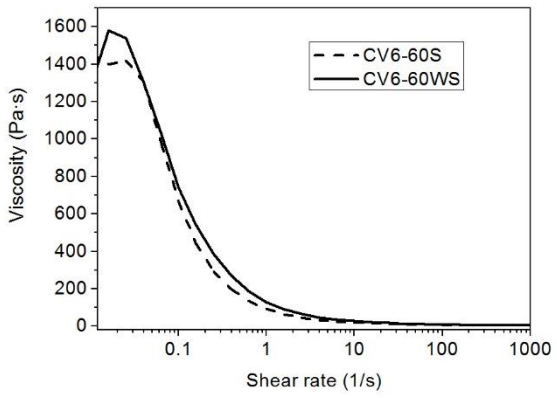


Figure 4.3: Results of the FT showing change in the viscosity vs. shear rate of the ink with 0.6 wt. % of surfactant CV6-60S and without surfactant CV6-60WS.

The low viscosity could contribute to the insufficient structure of the ink due to a reduced number of junctions between the polymeric chains and the cross-linking agents (powder particles); depending on the nature of the surfactant (commercial ESL 809, the composition of which I do not know), it can affect the surface of the inorganic particles as well as the active sites of the polymeric chains, which all inhibit the formation of the network [4, 16].

Despite the lower zero viscosity of the ink, large mesh-imprint defects were observed in the printed film CV6-60S due to an increase in the end viscosity at a percentage of recovery of 143 % (Table 4.1), which likely resulted from the changes in the ink's structure during the screen printing. At high shear rates, when the ink passes through the screen [19], the cross-linking of the dangling and free polymer chains, which are numerous due to the effect of the surfactant, could take place [4, 16]. The end viscosity of the ink was still relatively

low and despite the high rate of its recovery (K = 18 Pa) the creeping defect appeared due to the slow structuring of the ink, indicated by the steepness of the viscosity curve in the final stage of the recovery (higher k = 4 Pa^{-1}). For such characteristics the tackiness of the ink to the screen due to the dangling and free polymeric chains most likely also contributed to the appearance of the mesh imprints and, consequently, a higher roughness factor R_a of 0.51 µm [4, 16]. Hence, the paste CV6-60WS without the addition of the surfactant was prepared and its zero viscosity increased to 1580 Pa·s (Figure 4.3). According to the lower rate of recovery (K) the ink started to recover more slowly; however, the mild slope in the final stage of recovery (low k = 1.6 Pa^{-1}) indicated that it reached an equilibrium stage with a viscosity similar to the initial value (percentage of recovery R = 101%) faster. Hence, the film prepared from the ink CV6-60WS had good levelling and no defects with a smooth surface (R_a of 0.17 µm) (Table 4.1). In the viscosity curve of the ink CV6-60WS (Figure 4.3) the peak at a low shear rate is present, indicating that the ink has a shear thickening behaviour, while a decrease in the apparent viscosity at a higher shear stress indicates shear-thinning behaviour. A shear-thickening behaviour at low shear rates could be attributed to an elongation of the cellulose polymeric chains and additional interactions between the solid particles and the cellulose chains, leading to more structured macro-agglomerates that cause an increase in the viscosity. When the shear reaches a plateau value an ordering of the macro-agglomerates causes a drop in the viscosity [16]. In the case of such shear-thickening behaviour at low shear rates it is difficult to determine the zero viscosity. Therefore, I used the maximum measured viscosity as the zero viscosity [68].

A further increase in the solids load to 70 wt. % resulted in an increase of the zero viscosity of the ink CV6-70WS to 8550 Pa·s and the film surface showed mesh imprints and missing defects. Such a pronounced occurrence of the missing and the mesh imprint defects correlates well with the high surface-roughness factor R_a of 0.39 µm. The defects can be attributed to very high zero viscosity and, at the percentage of recovery (R = 80 %) still-too-high end viscosity; due to the extremely high rate of recovery K of 60 Pa the ink had insufficient time for levelling, despite the steep slope in the final stage of recovery (k = 4.1 Pa^{-1}) indicating that it needs more time to reach equilibrium conditions. The high viscosity resulted from a higher level of structuring due to more particles and, consequently, a higher probability of junction formations, which is also the reason for the rapid recovery after the stress was released [16].

The studies of the inks based on the vehicles CV6 and CV10 clearly showed that with the higher solids load the zero viscosity and the infinite viscosity increase. Higher solids load and the particle concentration enhance the interactions among the particles and also increase the probability of junction formation between the binder polymer and the particle, which results in a higher level of structuring and, consequently, an increased zero viscosity of ink, as well as a longer time for the ink to reach equilibrium conditions. It can be reduced with the addition of the surfactant; however, too low zero viscosity and end viscosity with a slow recovery of the ink cause creeping of the printed film. The first indication of a too high viscosity and a slow recovery time of the ink is the appearance of the mesh imprints. Even higher viscosity and time of recovery, in addition to the mesh imprints, results also in the occurrence of the missing defects in the film. The high-viscosity vehicle CV10 enabled the preparation of the printable inks only with the addition of a surfactant, while the

optimal properties occurred at the lowest solids load of 50% (CV10-50S). With the low-viscosity vehicle CV6 the optimal properties of the ink were obtained at a solids load of 60 wt. % and with no surfactant (CV6-60WS). Both inks had good printing characteristics and resulted in screen-printed films without defects; they had lower zero viscosity even with a higher solids load in comparison to the other inks based on the same vehicle, and also the higher recovery, which ensured the proper end viscosity and the time of recovery.

4.1.2 Inks based on our-selves made vehicles

To prepare a screen-printing ink with an even higher solids load the influence of the components and composition of ink on its properties and the quality of the screen-printed films were studied. The inks, based on the organic vehicle from solvents (2-(2-butoxyethxy) ethyl) acetate and αterpineol in the ratio 1:4, were optimized with respect to the addition of the surfactant ESL 809, the binder ethyl cellulose (EC) and the solids load. The compositions of the prepared and analysed inks are given in Table 4.1.

4.1.2.1 Influence of the surfactant on the ink's rheology and the quality of the printed thick film

The ink for screen printing typically has a solids load of about 60 wt. % [6]. Based on my own organic vehicle I initially prepared the ink A-70WS with a solids load of 70 % and without surfactant. The result of the FT (Figure 4.4) showed that it had a high zero viscosity of 7710 Pa·s and it was impossible to measure the R value.

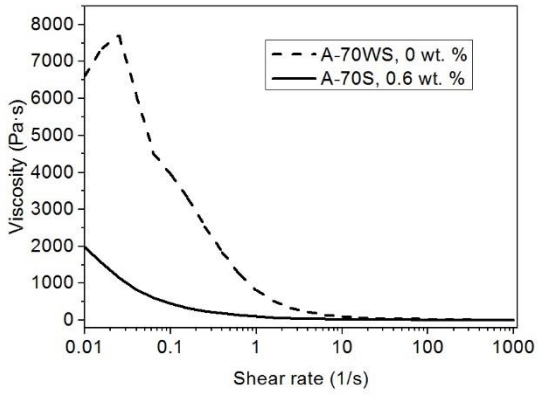


Figure 4.4: Results of the FT showing change in the viscosity vs. shear rate of the ink with 0.6 wt. % of surfactant A-70S and without surfactant A-70WS.

The screen-printed film had defects, such as missing or stencil clogging, and mesh imprints (Table 4.1), as shown in Figure 4.5 a and b.

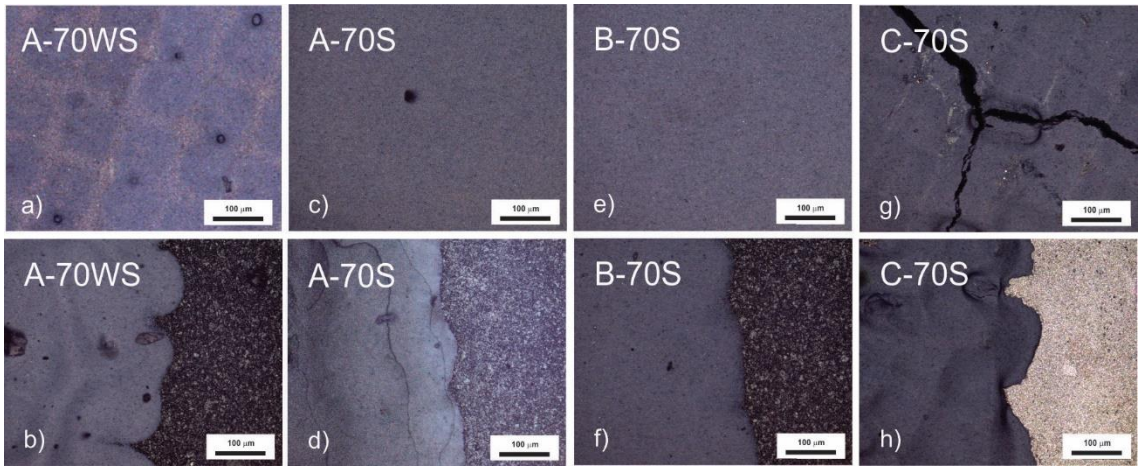


Figure 4.5: Confocal micrographs showing the surface (a, c, e, g) and the edge (b, d, f, h) of the printed films.

To reduce high viscosity of the A-70WS ink and possibly to improve the printing behaviour, a surfactant was added in the amount of 0.6 wt. % in the ink A-70S. The FT viscosity measurements showed that with the surfactant the zero viscosity dropped drastically from 7710 Pa · s to 1980 Pa · s (Figure 4.4). This indicated a significant influence of the surfactant on the ink's rheology with respect to the profiles of the screen-printed films of the inks A-70WS and A-70S; the film from the A-70S has a slightly elongated edge in comparison to the film from the A-70WS, which indicates that the rheological properties of the ink A-70S are just at a level where the creeping starts.

The viscosity curves of the A-70WS and the A-70S inks presented in Figure 4.4 clearly showed a drop in the viscosity with a higher shear rate, which indicated the required shear thinning behaviour of the inks for screen printing and is related to the α-terpineol-based solvent and ethyl cellulose as a binder. The stability of the ink depends on the ability of the particles to remain separated, which requires that the repulsive forces among the particles are larger than the attractive or Van der Waals forces, which makes an ink with a lower viscosity [5, 11]. The much lower zero viscosity of the ink A-70S resulted from the influence of the surfactant on the particle–polymer chains interactions, reducing the structuring of the ink by the limited formation of a cross-linking network. Due to the slow recovery of the viscosity at a K value of only 1.3 Pa and also the longer time needed to recover a higher level of structuring under equilibrium conditions, which is indicated by the steeper slope in the final stage of recovery with $k = 4.2$ Pa^{-1}, the formation of the mesh imprints was prevented, but creeping appeared (Figure 4.5 d). Once the surfactant is added in noticeable excess, strongly reduced interactions between the particles and the polymer chains result in dangling or free chains that can cause a bridging of the polymers and, consequently, coagulation, which is manifested in an increase of the viscosity [4, 16]. In my study the inks prepared with even higher surfactant additions were not suitable for printing. Hence, the addition of surfactant in the amount of 0.6 wt. % was shown to be appropriate for further optimisation of the ink.

4.1.2.2 Influence of the binder on the ink's rheology and the quality of the printed thick film

To reduce the creeping defect created by the surfactant addition and to further optimize the screen-printing ink, I studied the influence of the amount of added ethyl cellulose (EC) as a binder. According to literature reports by Sanson et al. [16] and Zhang et al. [4], a higher content of the EC binder increases the interactions between the particles and the long polymer chains of binder, which can reduce the creeping defect. Hence, I prepared three inks with different binder contents, given in Table 4.1.

The FT measurements seen in Figure 4.6 showed that with a higher binder content the zero viscosity increased from 1980 Pa·s with 2.0 wt. % (A-70S) to 4020 Pa·s with 2.6 wt. % (B-70S) and to 5810 Pa·s with 3.0 wt. % (C-70S).

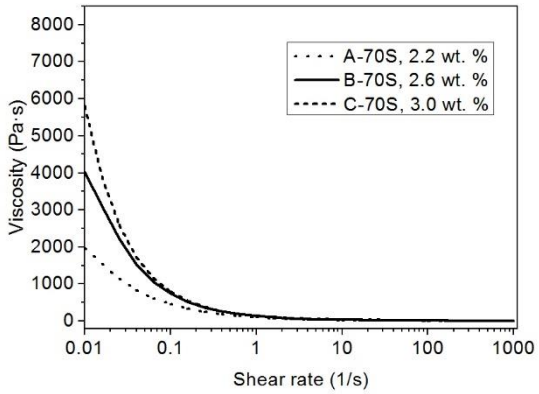


Figure 4.6: Results of the FT showing change in the viscosity vs. shear rate for the inks with various amounts of binder A-70S (2.2 wt. %), B-70S (2.6 wt. %), and C-70S (3.0 wt. %).

While the confocal micrograph of the printed thick film A-70S (Figure 4.5 d) with the addition of 2.0 wt. % of binder showed creeping defect, it was completely eliminated with the addition of 2.6 wt.% of binder in the B-70S (Figure 4.5 g). An increase in the amount of binder content increased the cross-linking of the inorganic particles and polymeric chains, which resulted in an increase of the network strength, improved viscoelastic properties and higher viscosity of the ink. Hence, after stress removal the ink B-70S showed a high rate of viscosity recovery with $K = 5$ Pa and according to the flatness of the k (1.5 Pa^{-1}) also the rapid establishment of equilibrium conditions with a compact structuring. However, when too much binder was added the mesh imprint defects started to appear in the case of the C-70S ink (Figure 4.5g). Their appearance was the result of a poor levelling and can be related to a high viscosity of the ink, which was quickly restored (high K value of 8 Pa) after the shear was released and also a further steady increasing of the viscosity toward the equilibrium conditions, as indicated by the k value of 2.9 Pa^{-1}. Such characteristics of the ink likely resulted from the high level of structuring and due to the high content of binder, also from dangling tails during high shear that can cause agglomeration of the polymers and tackiness to the mesh during printing. Consequently, cracks and missing defects were also observed in the film made from the C-70S ink.

The results of the SST seen in Figure 4.7 showed the viscosity response of the inks after the removal of the shear, indicating their levelling behaviour.

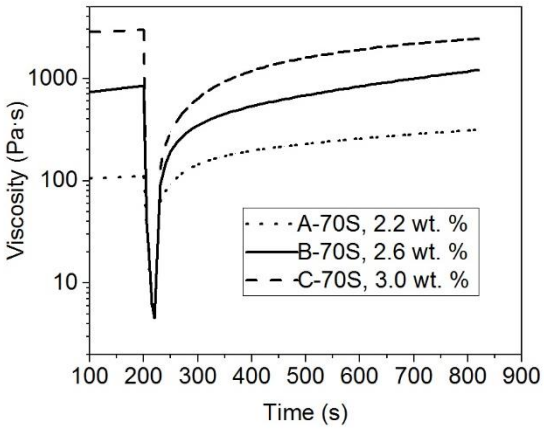


Figure 4.7: Result of the SST showing a change in the viscosity after the removal of the shear stress in inks with various amounts of binder: A-70S (2.2 wt. %), B-70S (2.6 wt. %), and C-70S (3.0 wt. %).

The ink A-70S with the lowest amount of binder has the lowest zero viscosity and hence at extremely high percentage of recovery (299 %) a relatively low end viscosity with a slow rate of recovery K, which is manifested in a creeping defect. The percentage of recovery of over 100 % can be correlated with the high solids load and the low polymer binder content. According to Hoffman [69], the ink with the high solids load could be considered as a deflocculated system where with critical shear rate solid particles arranged from a 2-demensional system to a 3-dimensional system that is more structured and produces a higher end viscosity. This is also in agreement with the transient network (TNT) theory, explaining the effect of the shear force on the elongation of binder macromolecules, which enable the additional interaction of the binder chains with the inorganic particles to form a more structured network [18]. These effects are much less pronounced in the inks with the same solids load, but larger additions of the binder, which already have a higher level of network structuring. The C-70S ink with the highest addition of binder showed the highest zero viscosity and hence at a relatively low percentage of recovery (86 %) for the inks of this series a high end viscosity, which resulted in mesh imprints and cracks after the drying of the screen-printed film. The ink B-70S with the medium addition of binder had a relatively moderate end viscosity and a moderate slope in the third region of the SST test, despite the higher percentage of recovery (140 %). This ink was found to be stiff and the screen printing resulted in a defect-free thick film after drying.

4.1.2.3 Influence of the solids load on the ink's rheology and the quality of the printed thick film

Based on the results of the optimisation of the ink in the previous steps, with respect to the organic vehicle's composition, I further analysed the influence of the solids-load increase on the rheology and the printing characteristics of the inks. The zero viscosity increased

with a higher solids load (Table 4.1 and Figure 4.8) from 3170 Pa·s with 65 wt. % (B-65S) to 4020 Pa·s with 70 wt. % (B-70S), and even to 10300 Pa·s with 75 wt. % (B-75S).

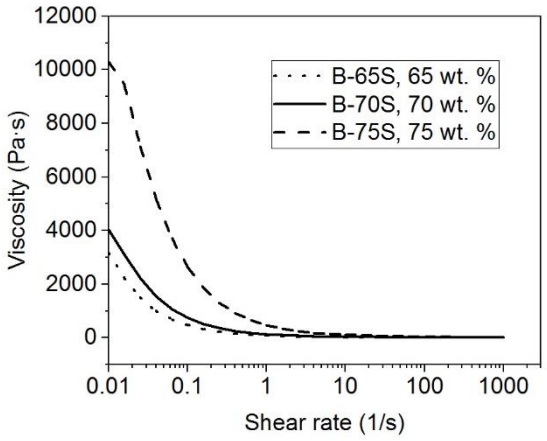


Figure 4.8: Results of the FT showing change in the viscosity vs. shear rate for the inks with various amounts of solids load B-65S (65 wt. %), B-70S (70 wt. %), and B-75S (75 wt. %).

At a higher solids load there are fewer free and dangling polymer chains because of the increased interaction between the binder polymer chains and the particles, which results in a more structured ink network and, consequently, a stiffer ink with a higher zero viscosity. It is interesting that there is also a drop in the infinite viscosity (Table 4.1) with a higher solids load from 4.8 Pa·s of B-65S to 3.5 Pa·s of B-75S. In the ink with the lower solids load fewer interactions between the particle and the polymer binder chain result in more free polymeric tails, which at high shear rates tend to tangle, causing an increased infinite viscosity [42].

From the SST results (Table 4.1 and Figure 4.9) it is clear that the ink B-65S, with the lowest solids load in this series of samples, also had the lowest zero viscosity and at low percentage of recovery equal to 83 % also a lower end viscosity.

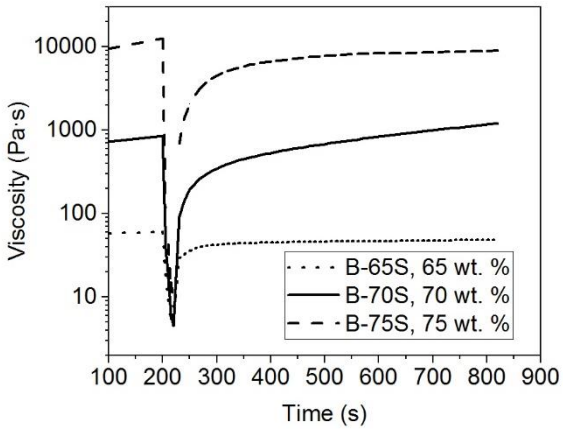


Figure 4.9: Result of the SST showing a change in the viscosity after the removal of the shear stress in inks with various amounts of solids load B-65S (65 wt. %), B-70S (70 wt. %), and B-75S (75 wt. %).

It also had an extremely low rate of recovery K (0.3 Pa) after the stress is removed; it means that in the printed film the ink needed more time to recover its viscosity, which was still too low to prevent creeping, and also minimally increased in the final stage of recovery at an extremely low k value of 0.01 Pa^{-1} (Figure 4.10 b).

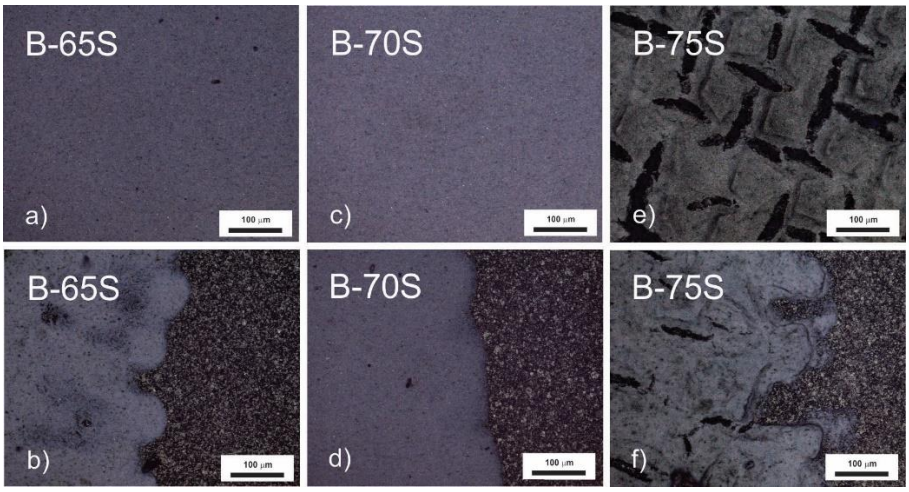


Figure 4.10: Confocal micrographs showing the surface (a, c, e) and the edge (b, d, f) of the printed films.

A higher solids load of 75 wt. % (B-75S) gave a very high zero viscosity of 10300 Pa·s and a percentage of recovery equal to 97 % due to the stronger association between the particles and polymeric chains, and hence a more structured ink network. In addition, the high rate of recovery K of 67 Pa indicated an extremely fast recovery of the viscosity to a too high value of the viscosity for proper levelling of the ink after printing, and it further increased relatively quickly (k = 4.7 Pa^{-1}). Hence, in the film made from the ink B-75S missing defects, mesh imprints and also cracks were observed, as shown in Figure 4.10f. As could be expected from the optical examinations of the films, an increase in the surface roughness (R_a) was also observed with an increase of the solids load from 0.13 µm with 65 wt. % to 0.21 µm with 70 wt. % and 0.22 µm with 75 wt. %. The maximum solids load in the ink with still suitable characteristics to print, i.e., with no observable defects, was 70% in the ink B-70S.

4.2 Thick-Film Varistors

4.2.1 Influence of the solids load on the microstructure and the electrical properties

Once I obtained inks with good printing characteristics, I was able to study, under optimal conditions, the influence of the solids load on the densification and microstructure development. The microstructure development in the varistor ceramics is of key importance for obtaining good current–voltage (I–U) characteristics. There are various parameters that can influence the densification of a thick film. However, with the same technical process and the same composition of the varistor powder (solids load), we can reduce the options

to two key parameters of the ink, i.e., the composition of the organic vehicle and the solids-load concentration.

In the early stage of the firing regime the organic vehicle has to burn out efficiently and leave no residues that could interfere with the sintering process, and without the formation of micro- and macro-defects (cracks), keeping the structure of the solid particles compact. A higher solids load in the ink means a higher density of the particles in the film and better contact among them after the removal of the organic vehicle, which can provide better conditions for densification and further microstructure development. The effect of the solids load on the microstructural characteristics of the thick-film varistors was studied using inks with a solids load of 50 wt. % (CV10-50S), 60 wt. % (CV6-60WS) and 70 wt. % (B-70S). They were selected due to their suitable rheological properties and good screen-printing characteristics, leading to defect-free films.

Since they are based on different organic vehicles, I wanted to evaluate the effect of the organic vehicle on the densification to clearly distinguish the effect of the solids load. In this regard I analysed thick films prepared using the same organic vehicle and different solids loads of 65 wt. % (B-65S) and 70 wt. % (B-70S). Figure 4.11 shows SEM micrographs of the cross-sections of the analysed thick-film varistors prepared from these four different screen-printing inks.

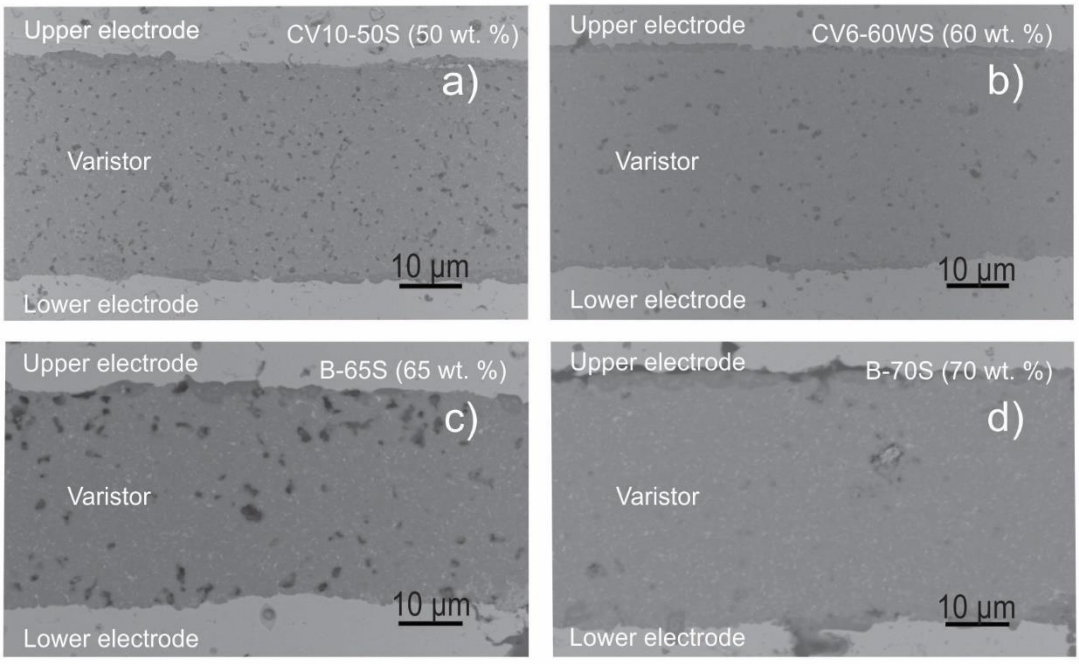


Figure 4.11: SEM micrographs of thick-film varistors fired at 900 °C, made from screen-printing inks containing different amount od solids load a) CV10-50S (50 wt. %), b) CV6-60WS (60 wt. %), c) B-65S (65 wt. %) and d) B-70S (70 wt. %).

It is clear that the porosity of the thick films decreased with an increase of the solids load in the printing ink. Also in the case of films made from inks based on the same organic vehicle, the printed film of B-65S ink (Figure 4.11 c) with 65 wt. % of solids load had a noticeably higher porosity than the film made from the B-70S ink with a solids load of 70 wt. % (Figure 4.11 d). It should also be emphasised that with an increase of the solids load

in the screen-printing ink the thickness of the printed single layer after drying increased from 14.1 µm (50 wt. %) to 23.3 µm (70 wt. %). The increase of the thickness of the film is also evident after firing and the observed values for one printed layer are from 10 µm (50 wt. %) to 20 µm (70 wt. %). These results clearly indicate the dominant role and influence of the solids-load concentration in the ink on the density of the screen-printed, thick-film varistors. All the films presented in Figure 4.11 have a homogenous microstructure, a uniformly distributed Bi_2O_3-rich phase and a well-established contact between the varistor ceramics and the electrode. However, the film made from the B-70S ink with 70% of solids load had a noticeably higher density (i.e., a lower porosity).

The solids load in the ink affects not only the microstructure but also electrical properties of the thick-films. The electrical characteristics of the screen-printed thick-film varistors fired at 900 °C for 15 minutes are summarized in Table 4.2.

Table 4.2: The electrical characteristics of the thick-film varistors on an alumina substrate made from inks with different solids loads, fired at 900 ˚C (15 min).

Thick–film varistor	U_T (V/mm)	α (/)	I_L (µA)
CV10-50S (50 wt. %)	1712	11	47
CV6-60WS (60 wt. %)	1850	8	210
B-65S (65 wt. %)	1838	10	111
B-70S (70 wt. %)	1720	16	44

The nominal breakdown voltages (U_N (1mA/cm^2)) of the films were in the range from about 90 to 175 V, as shown by the graphical presentation of the voltage U_N vs. the current density J in Figure 4.12, while their threshold voltages (U_T), i.e., the breakdown voltage per unit thickness, were between 1700 and 1850 V/mm (Table 4.2).

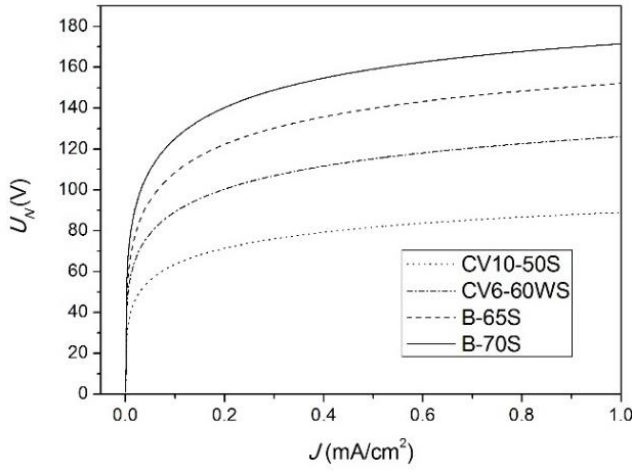


Figure 4.12: Voltage–current density (U–J) characteristics of printed varistors made from inks with different solids loads CV10-50S (50 wt. %), CV6-60WS (60 wt. %), B-65S (65 wt. %) and B-70S (70 wt. %).

Only the screen-printed films made from the ink with 70 wt. % of solids load (B-70S), with the highest density, exhibit a reasonably good varistor behaviour, with a coefficient of nonlinearity α of 16 and a relatively low leakage current I_L of 44 µA (Figure 4.12). The α values of my films are comparable with the α values reported for the screen-printed varistors in the literature. A comparison of the electrical characteristics of the films prepared with the inks based on the same organic vehicle, i.e., B-65S and B-70S, also shows that the B-70S ink with the higher solids load resulted in better electrical properties, i.e., higher U_T and α values and a lower I_L.

4.2.2 Influence of the Bi_2O_3 content and Sb/Bi ratio on the microstructure and the electrical properties

For further optimization of the thick-film varistors, a study about the influence of the active powder composition was made by variating the amount of Bi_2O_3 and the Sb/Bi ratio. The different compositions of the varistor powder mixtures and the obtained electrical characteristics of the screen-printed thick-film varistors fired at 900 °C for 15 minutes are summarized in Table 4.3. Each of the fired varistor films exhibited nonlinear *J-U* behaviour with U_n in the range from 94 to 175 V and αvalue in the range from 17 to 24.

Table 4.3: The electrical characteristics and average grain size of the thick-film varistors with different Bi_2O_3 contents and different Sb/Bi ratio.

Varistor	Bi_2O_3	Sb/Bi	U_N	U_T	α	I_L	Average grain size	Standard deviation
	mol. %	ratio	V	V/mm	/	µA	µm	µm (%)
DV1	0.8	0.25	94	2510	17	14	0.50	± 0.21 (42%)
DV2	0.8	0.8	107	2620	18	13	0.46	± 0.19 (41%)
DV3	0.8	1.25	119	2900	19	12	0.42	± 0.16 (38%)
DV4	0.4	0.8	175	4760	20	100	0.41	± 0.16 (39%)
DV5	1.6	0.8	117	3080	24	10	0.49	± 0.22 (45%)
DV6	1.8	0.8	108	2840	23	11	0.41	± 0.18 (44%)

It can be seen from Table 4.3 and Figure 4.13 that with higher Sb/Bi ratio, at the same amount 0.8 mol. % of Bi_2O_3 the threshold voltages (U_T) tend to increase from 2510 V/mm with 0.25 Sb/Bi ratio (DV1) to 2620 V/mm with 0.8 Sb/Bi ratio (DV2) and to 2900 V/mm with 1.25 Sb/Bi ratio (DV3).

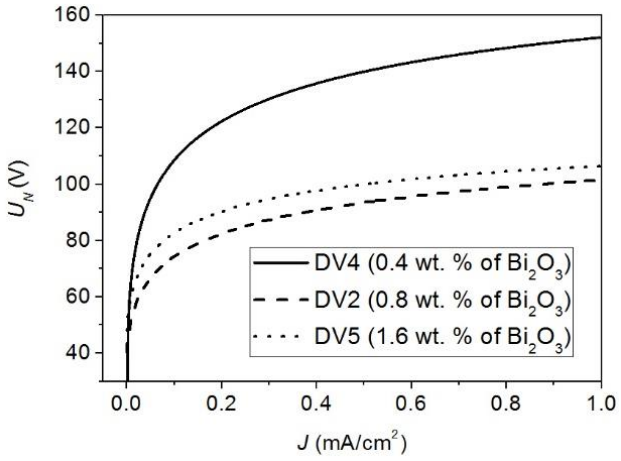


Figure 4.13: Voltage–current density (U–J) characteristics of printed varistors made with different Bi_2O_3 amounts: DV4 (0.4 wt. %), DV2 (0.8 wt. %) and DV5 (1.6 wt. %).

At the Sb/Bi ratio smaller than 1, in the samples DV1 and DV2, all Sb_2O_3 is consumed according to Eq. (1.5) forming a pyrochlore phase. Consequently, some of the free Bi_2O_3 results in the formation of the liquid phase during firing, which enhances sintering and the grain growth, as seen in Figure 4.14 a, b.

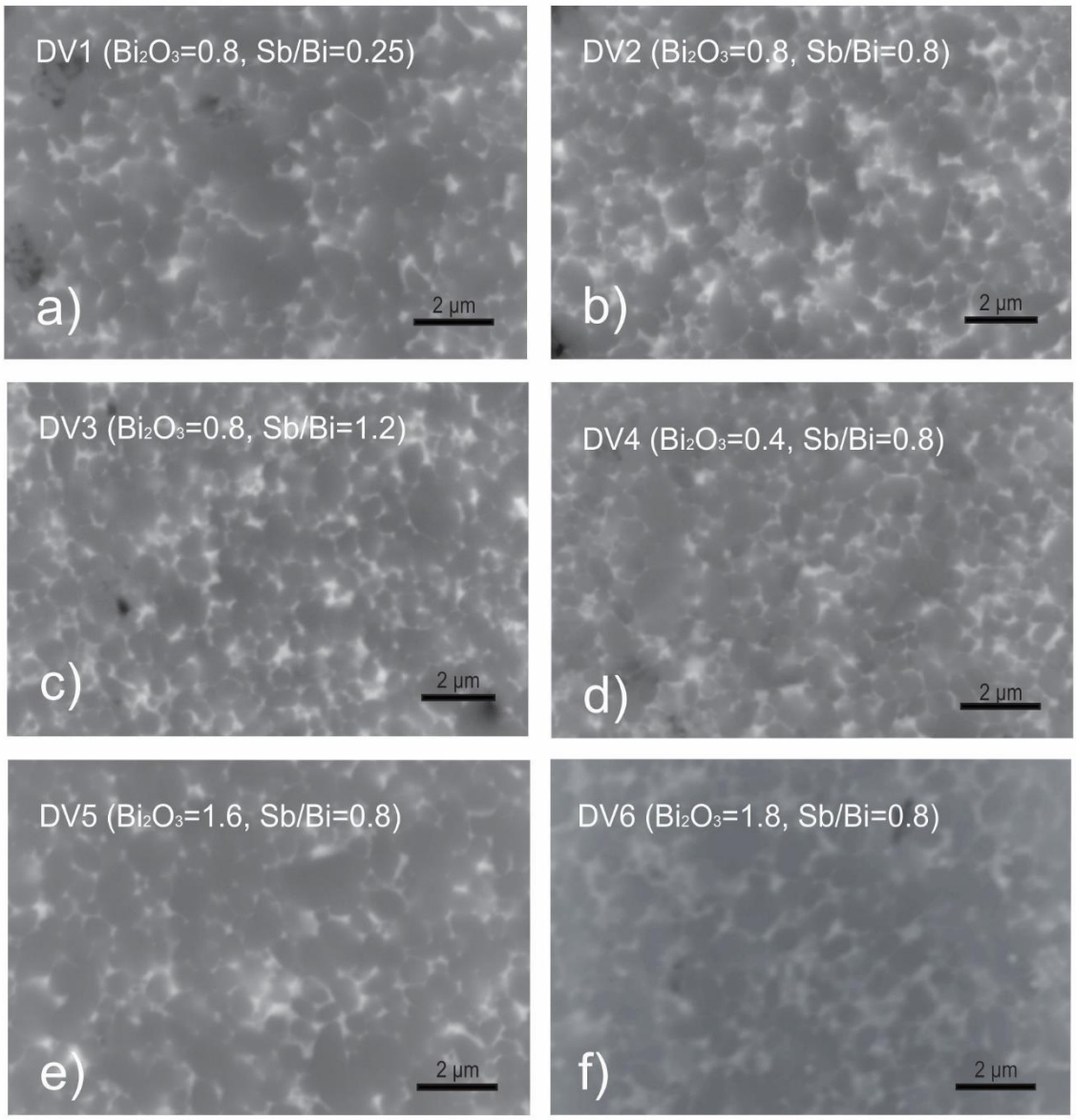


Figure 4.14: SEM micrographs of thick-film varistors with different Bi_2O_3 contents and different Sb-Bi ratio.

This observation is also supported by the grain size analysis summarized in Table 4.3, showing the average grain size of 0.5 µm in the DV1 sample and a slightly decreased size of 0.46 µm in the DV2 sample. The standard deviation in both samples is quite high, ie. 42 % for DV1 and 41 % for DV2. Such standard deviations indicate the presence of larger grains in the microstructure, which is even more evident from the histograms of the grain size distribution presented in Figure 4.15. With a fraction of much larger grains low resistivity conduction paths are locally formed with a reduced number of nonlinear (varistor) grain boundaries, which shows in lower nominal voltages (U_N) and also nonlinear coefficient α.

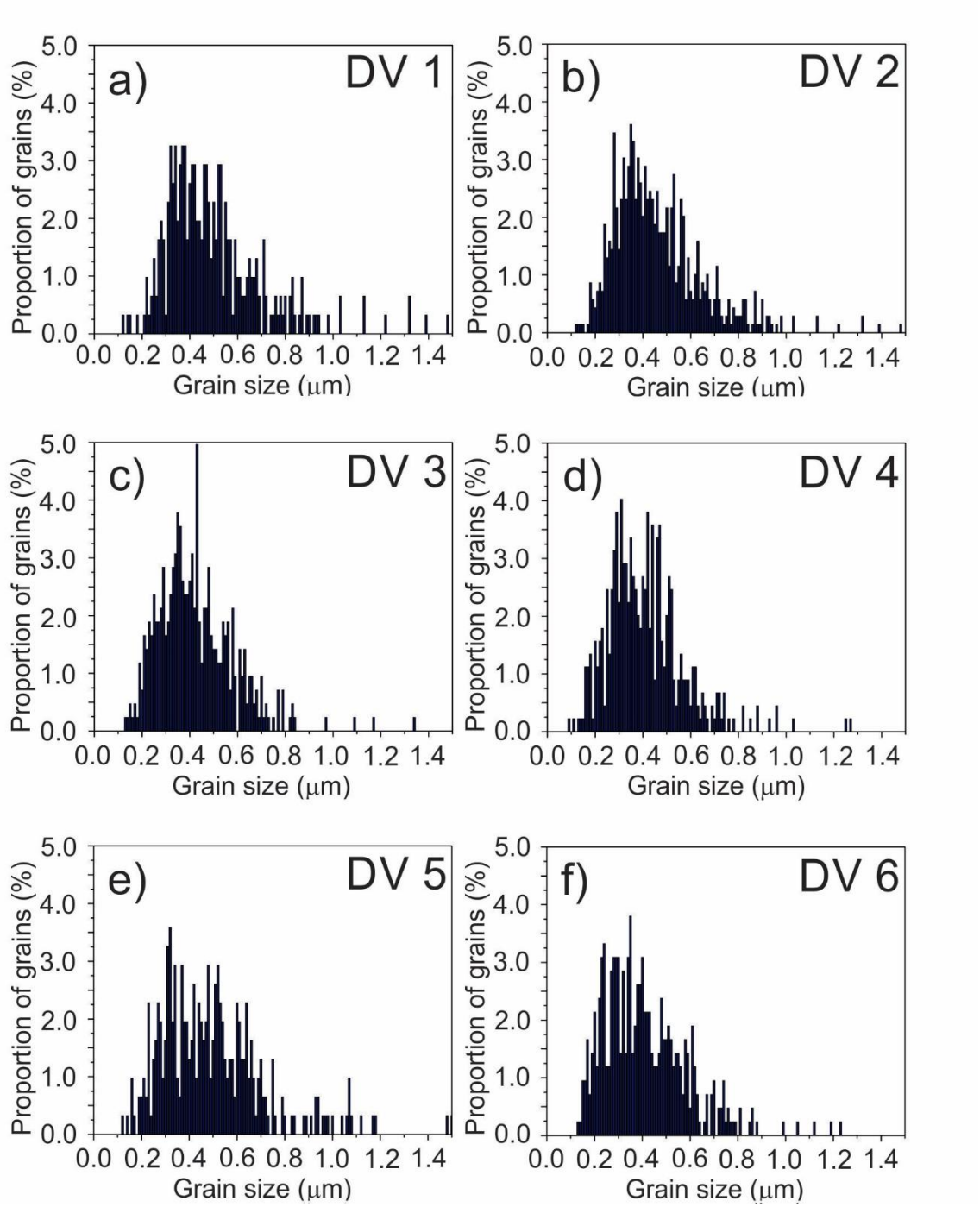


Figure 4.15: Histograms of the grain size distribution measured for samples DV1, DV2, DV3, DV4, DV5 and DV6, showing grain size and their proportion.

With the Sb/Bi ratio larger than 1, in sample DV3, all the Bi_2O_3 is consumed by the pyrochlore formation. The Sb_2O_3 that is not incorporated in the pyrochlore phase can undergo reaction according to Eq. (1.4) to form the spinel phase, which hinders grain growth and results in higher U_T. Hence, the varistor DV3 with large Sb/Bi ratio of 1.25 had smaller average grain size of 0.42 µm and narrower grain size distribution (Figure 4.15 c) with standard deviation of 38 %. The absence of much larger grains and hence more homogeneous microstructure (Figure 4.20 c) resulted also in higher α. The α in the samples

with the same Bi_2O_3 content increases from 17 in the sample with 0.25 Sb/Bi ratio (DV1) to 18 in the sample with 0.8 Sb/Bi ratio (DV2) and to 19 in the sample with 1.25 Sb/Bi ratio (DV3). With the higher Sb/Bi ratio the samples have a narrower grain size distribution and hence more homogenous density of grain boundaries, which can also contribute to the higher α value.

The Dong et al. [32] showed that Bi_2O_3 vaporization has a significant impact on the electrical characteristics of varistor ceramics, even higher when the area/volume (A/V) ratio is high. In the classic bulk varistors the A/V ratio is typically in the range from 1 to 5 cm^{-1} and vaporization at 900 °C in short firing times (usually 10-15 min at peak temperature) can be over 10 wt. % [31, 32]. However, in thick films the A/V ratio can exceed 40 cm^{-1} and consequently the expected Bi_2O_3 vaporization can be even higher. Hence, I prepared samples with even lower and also higher Bi_2O_3 contents. It can be seen from Table 4.3 and Figure 4.16 that with the same Sb/Bi ratio at 0.8, the sample with lower 0.4 wt. % of Bi_2O_3 had U_T 4760 V/mm (DV4) while with 0.8 wt. % Bi_2O_3 decreased to 2620 V/mm (DV2).

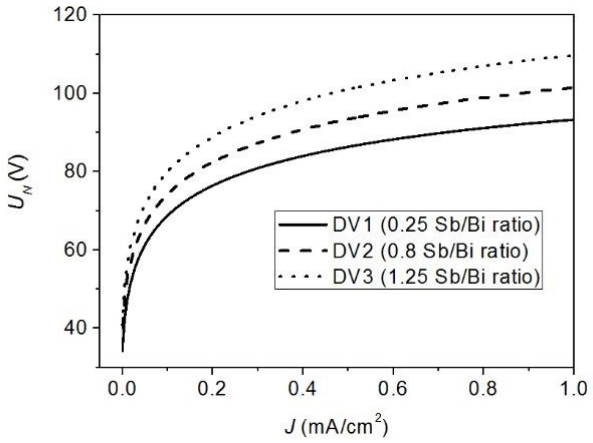


Figure 4.16: Voltage–current density (U–J) characteristics of printed varistors made with different Sb/Bi ratios DV1 (0.25), DV2 (0.8) and DV3 (1.25).

The high U_n can be explained with lower Bi_2O_3 content in the DV4 sample, which means less liquid phase during firing. Hence, it had smaller grains with the average size 0.41 µm and narrower size distribution according to the lower standard deviation of 39 % and the histogram of size distribution (Figure 4.15). The microstructure of the DV4 sample is shown in Figure 4.20d. At higher Bi_2O_3 the addition of 1.6 wt. % (DV5) U_T slightly increased to 3080 V/mm in comparison to the sample (DV1). At even higher addition of Bi_2O_3 1.8 wt. % (DV6) U_T was 2840 V/mm and only slightly smaller in comparison to the DV5 sample. At higher additions of Bi_2O_3 and Sb_2O_3 more of the spinel phase (Eq. (1.4)) and the pyrochlore phase (Eq. (1.5)) could be expected. With a higher amount of Bi_2O_3-rich liquid phase (Sb/Bi < 1) and a higher amount of inactive phases (pyrochlore and spinel) increased microstructural non-homogeneity with the presence of large grains could be expected (Figure 4.14 e, f). The DV5 sample had an average grain size of 0.49 µm and smaller, about 0.41 µm, for the DV6 sample. While the samples had similar standard deviation of grain

size, 45 % DV5 and 44% DV6, the histograms of grain size distribution indicate a narrower distribution in the sample DV6.

It can be seen from Table 4.3 that α value increased from 18 in the sample with 0.8 wt. % of Bi_2O_3 (DV2) to 24 in the sample with 1.6 wt. % of Bi_2O_3 (DV5). This increase can be correlated with a larger amount of free Bi_2O_3-rich liquid phase along the grain boundaries, which among other affects also the distribution of other varistor dopants in the microstructure important for the formation and characteristics of the electrostatic barriers resulting in higher α.

4.2.3 Influence of the firing time on the microstructure and the electrical properties

In a further study about the influence of the firing time on the microstructure development and the electrical characteristics of thick-film varistors, I used the varistor composition DV1. The electrical characteristics of thick-film varistors fired at 900 °C for different firing times of 15 min., 30 min. and 60 min. are summarized in Table 4.4.

Table 4.4 The electrical characteristics of the thick-film varistors with the composition DV1, fired at 900 °C for different durations.

t	U_N	α	I_L	U_T
min	V	/	µA	V/mm
15 min	94	17	14	2510
30 min	79	13.3	21	2017
60 min	69	12	22	1700

The U_T decreased from 2510 V/mm with a firing time of 15 min to 2017 V/mm with a firing time of 30 min and to 1700 V/mm at a firing time of 60 min. The size of the grains increases with a longer firing time. According to Eq. (1.7), the larger the average grain size, the smaller the U_T. With a longer firing time the nonlinear coefficient α also decreased from 17 to 12. This can be likely correlated with a larger evaporation of the Bi_2O_3 with a longer firing time, which can affect the number and characteristics of the electrostatic barriers at the grain boundaries.

4.3 Thick-Film Thermoelectric Micro Generators

For screen printing of the thick-film thermoelectrics, the ink was made on the basis of the optimized composition B-70S. The powders of the thermoelectric materials used as the solids load in the inks were prepared by grinding sintered bulk samples shown in Figure 4.17 a and b. The grinded powders from pellets Ca349 and Z5I are presented in Figure 4.17 c and d, respectively. The average particle size after homogenization d_{50} was 0.58 µm for Ca349 and 0.60 µm for Z5I, measured with a laser-scattering particle size distribution analyser (Horiba LA–920). The particles of the powders have an irregular shape and also probably contain mechanically induced defects (Figure 4.17 c, d).

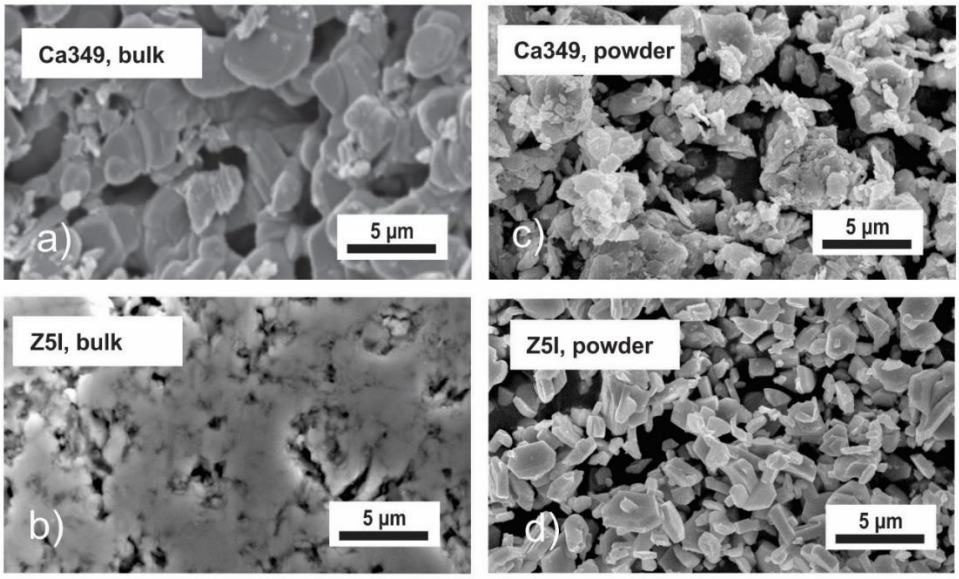


Figure 4.17: Microstructures of a polished cross-section of the bulk ceramics and powders of the $Ca_3Co_4O_9$ (Ca349) and $(ZnO)_5In_2O_3$ (Z5I) TE materials.

The XRD patterns presented in Figure 4.18 confirmed that the Z5I powder consists of the $Zn_5In_2O_8$ phase (JCPDF 00-020-1440) and the Ca349 powder is composed of the $Ca_3O_4O_9$ phase (JCPDF 00-021-0139).

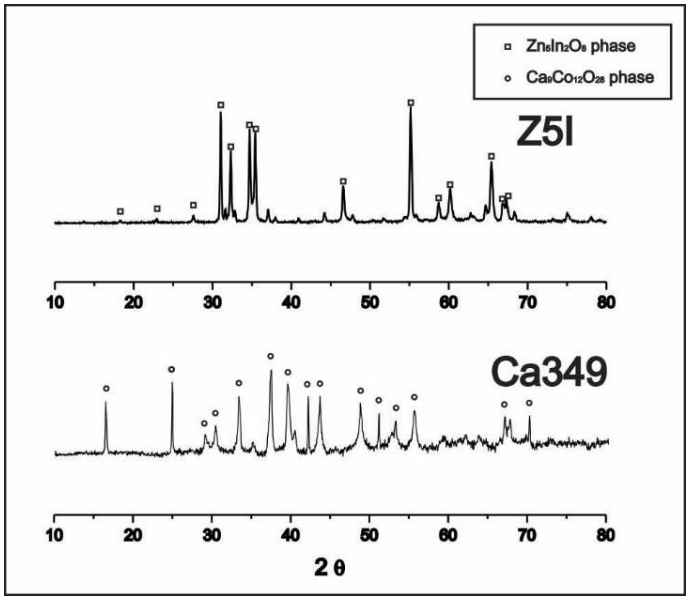


Figure 4.18: The X-ray diffractograms of the $(ZnO)_5In_2O_3$ and $Ca_3Co_4O_9$ powders.

4.3.1 Thick-film thermoelectric microgenerators based on $Ca_3Co_4O_9$

Configuration of the thick-film thermoelectric microgenerator made by screen printing of the Ca349-based ink is shown in Figure 4.19.

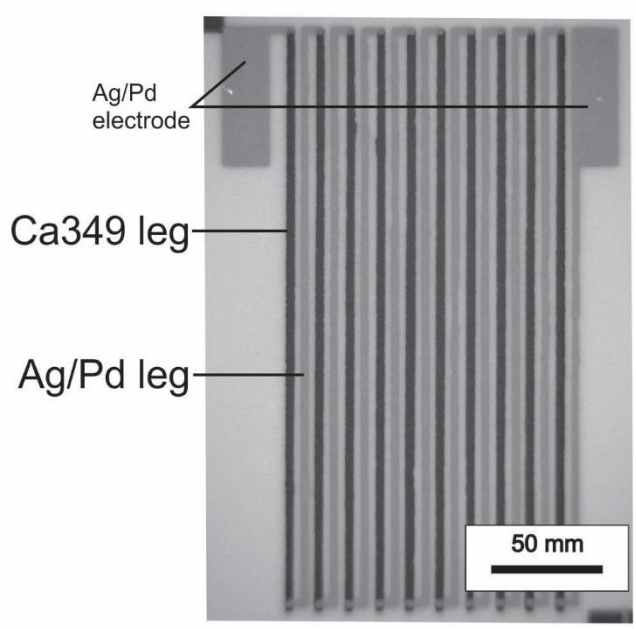


Figure 4.19: Screen-printed thick-film microgenerator made from ten Ca349 legs and ten Ag/Pd legs connected in series.

Microstructures of the surfaces and the polished cross-sections of the Ca349 films are presented in Figure 4.20.

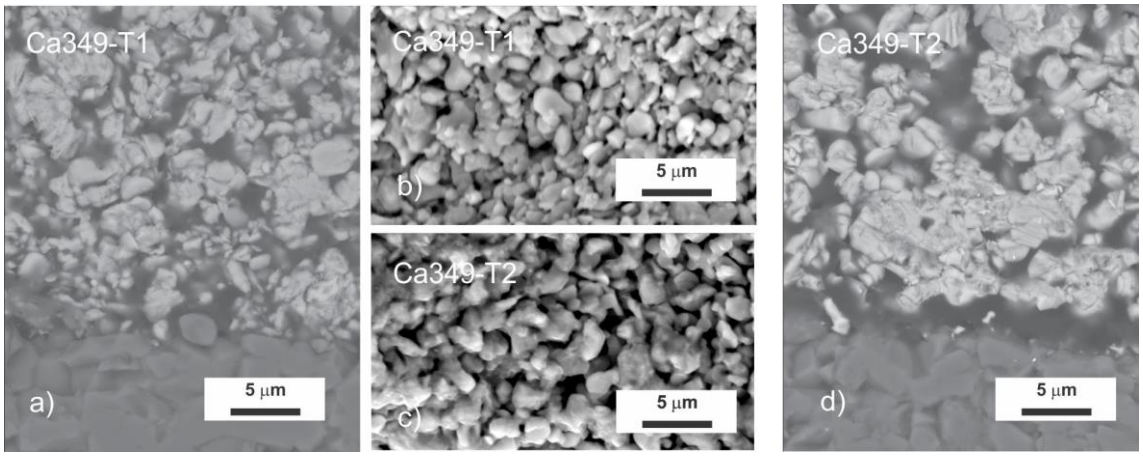


Figure 4.20: SEM micrograph of the Ca349 thick-film: cross-section a) and surfaces b) fired temperature of 900 °C (T1) and cross section d) and surfaces c) fired temperature of 920 °C (T2).

The SEM micrographs showed that both Ca349 films fired at slightly different temperatures are quite porous, but with good contact to the substrate and without a visible reaction at the interface. While in the grinded powder (Figure 4.17 c) some separate grains with the size up to 1 µm having sharp and irregular edges could be observed among larger irregular-shaped grain-clusters with the size up to 5 µm, the uniformity of the Ca349 grains improved significantly in the film after firing; the size distribution of the grains is more uniform and their morphology is more homogenous with rounded shapes (Figure 4.20). The grains in the Ca349-T2 film, fired at a higher temperature, are even slightly larger and

with more rounded shapes than in the Ca349-T1 film, fired at a lower temperature. Also, the presence of larger dense areas in the microstructure indicated better contacts between the grains in the Ca349-T2 film than in the Ca349-T1 film. The microstructures of the films are closely related to their electrical characteristics. For measuring the resistivity of the Ca349 thick films I tested Pd/Ag and Pt as a contact electrode; however, there was no significant difference in the measured resistivity between them. Therefore, I used the cheaper Pd/Ag electrodes for all subsequent measurements. The results of the resistivity and the Seebeck-coefficient measurements of the $Ca_3Co_4O_9$ (Ca349) are collected in Table 4.5.

Table 4.5: Electrical properties of Ca349 thick-films fired at different temperatures.

Sample	ρ (500 °C)	S (300 °C)	Px10^{-3} (300 °C)
	m$\Omega \cdot$ cm	µV/K	W/mK^2
Ca349-T1, 900 °C	13.7	156	0.161
CA349-T2, 920 °C	13.3	151	0.146

The specific resistivity of the samples decreases with increasing the temperature, as can be seen in Figure 4.21. It is noticeably higher at room temperature and only slightly higher at temperatures up to 250 °C for the sample Ca349-T1 fired at 900 °C in comparison to the sample Ca349-T2 fired at 920 °C, while at higher temperatures both samples had a similar specific resistivity. The higher resistivity of the sample Ca349-T1 could be contributing to the weaker restoration of the microstructure in the film fired at the lower temperature, as indicated by the slightly smaller grain size and, consequently, the larger number of grain boundaries [70, 71].

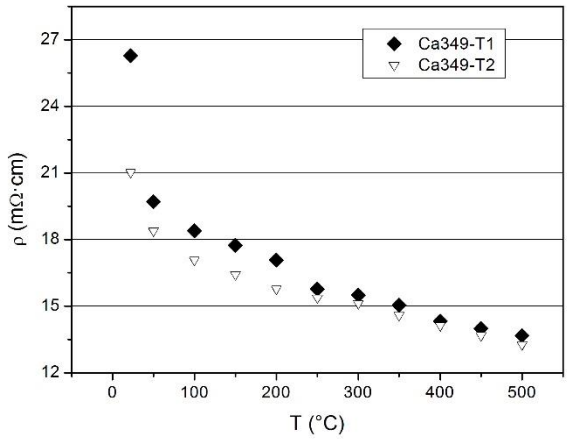


Figure 4.21: Temperature dependence of the specific resistivity for Ca349 thick-films fired at different temperatures Ca349-T1 (900 °C), Ca349-T2 (920 °C).

Figure 4.22 shows the temperature dependence of the Seebeck coefficient (*S)* calculated for a single Ca349 thermoelectric leg.

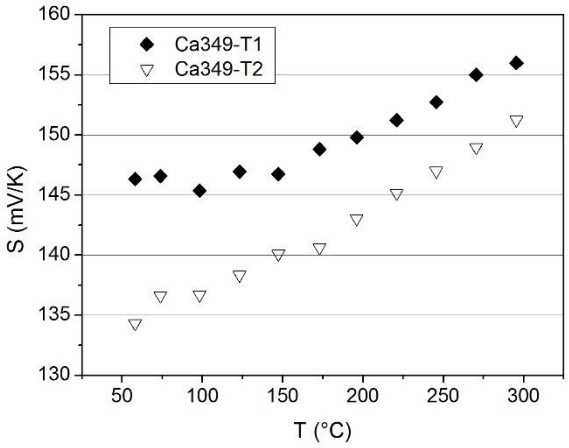


Figure 4.22: Temperature dependence of the Seebeck coeficient of the Ca349 thick-films fired at different temperatures Ca349-T1 (900 °C), Ca349-T2 (920 °C).

Across the whole temperature range of the measurements the S of the Ca349 samples increases and is slightly higher for the Ca349-T1 sample fired at 900 °C than for the Ca349-T2 sample fired at 920 °C; at 300 °C their values of S are 156 μV/K and 151 μV/K, respectively. The higher S observed in the sample Ca349-T1 fired at a lower temperature could be related to the enhanced energy-filtering effect of the charge carriers due to an increased grain-boundary density at a smaller grain size; the higher potential barriers of the less-developed boundaries with more defects can immobilise low-energy charge carriers, which increases the average carrier energy and consequently increases S [70, 71, 72]. The temperature dependence of the power factor (P) for the single $Ca_3Co_4O_9$ thermoelectric leg is shown in Figure 4.23.

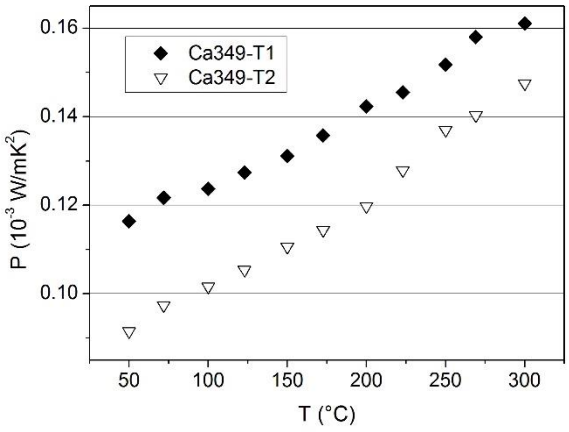


Figure 4.23: Temperature dependence of the Seebeck coeficient of Ca349 thick-films fired at different temperatures Ca349-T1 (900 °C), Ca349-T2 (920 °C).

The Ca349-T2 sample, fired at 920 °C, had a lower P than the Ca349-T1 sample, fired at 900 °C, which is mainly due to its lower S at just a slightly higher specific electrical conductivity (lower specific resistivity). The results indicated that the grain size and the

grain boundaries strongly influence the values of S and ρ, and consequently the value of P. With a higher firing temperature, I obtained larger grains, fewer grain boundaries and a larger contact area between the grains, an enhanced number of possible electron paths and a reduced specific resistivity. However, with larger grains the density of the grain boundaries is decreased and with this, effective energy filtering, so that fewer low-energy carriers were blocked, which resulted in a reduced value of S.

The calculated power factor (P) value for the Ca349-T1 sample is $0.16 \cdot 10^{-3}\,\mathrm{W/mK^2}$. It is about 25 % higher than for the starting bulk Ca349 material used for the preparation of the screen-printing ink [73] and about 25 % lower than that reported in the literature for bulk $Ca_3Co_4O_9$ ceramics [51], all measured at 300 °C. The similarity of the obtained TE characteristics can be explained on the basis of a comparison with the microstructures of the bulk sample fired for 20 h at 900 °C and the thick film $Ca_3Co_4O_9$ fired for 15 min at 900 °C, shown in Figure 4.17 and Figure 4.20, respectively. Both samples have a similar microstructure of the connected grains with high porosity; however, the grains in the bulk sample are slightly larger with a more round shape. Both samples also have a highly porous structure. The comparison clearly indicates that both Ca349 samples, i.e., the bulk and the thick film, have similar microstructures. The bulk material Ca349 has a twofold higher specific electrical resistivity, which is $33.3\ \mathrm{m\Omega \cdot cm}$, in comparison with the thick-film Ca349-T2 and $15.5\ \mathrm{m\Omega \cdot cm}$, both at 300 °C. Both samples are single-phase $Ca_3Co_4O_9$ ceramics and have similar microstructures, which also results in similar Seebeck coefficients at 300 °C, with 141 μV/K for the bulk Ca349 and 151 V/K for the thick-film Ca349-T2. The differences in the obtained values, especially for the electrical resistivity, could result from the different measurement methods; the bulk samples were measured with a Z-meter in high vacuum [74] and the thick films were measured in the air.

4.3.2 Thick-film thermoelectric microgenerators based on $(ZnO)_5In_2O_3$

Configuration of the thick-film thermoelectric microgenerator made from Z5I material is shown in Figure 4.24.

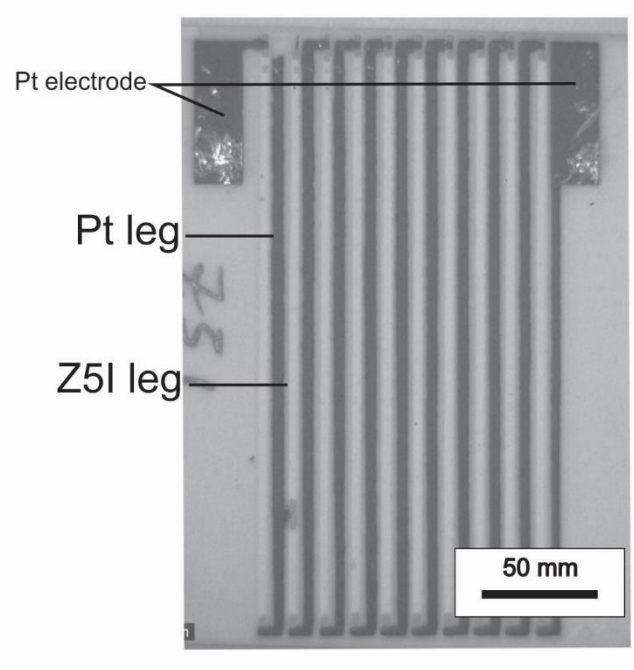


Figure 4.24: Screen-printed thick-film microgenerator made from ten Z5I legs and ten Pt legs connected in series.

Microstructures of the surface and the cross-section of the Z5I thick films are presented in Figure 4.25.

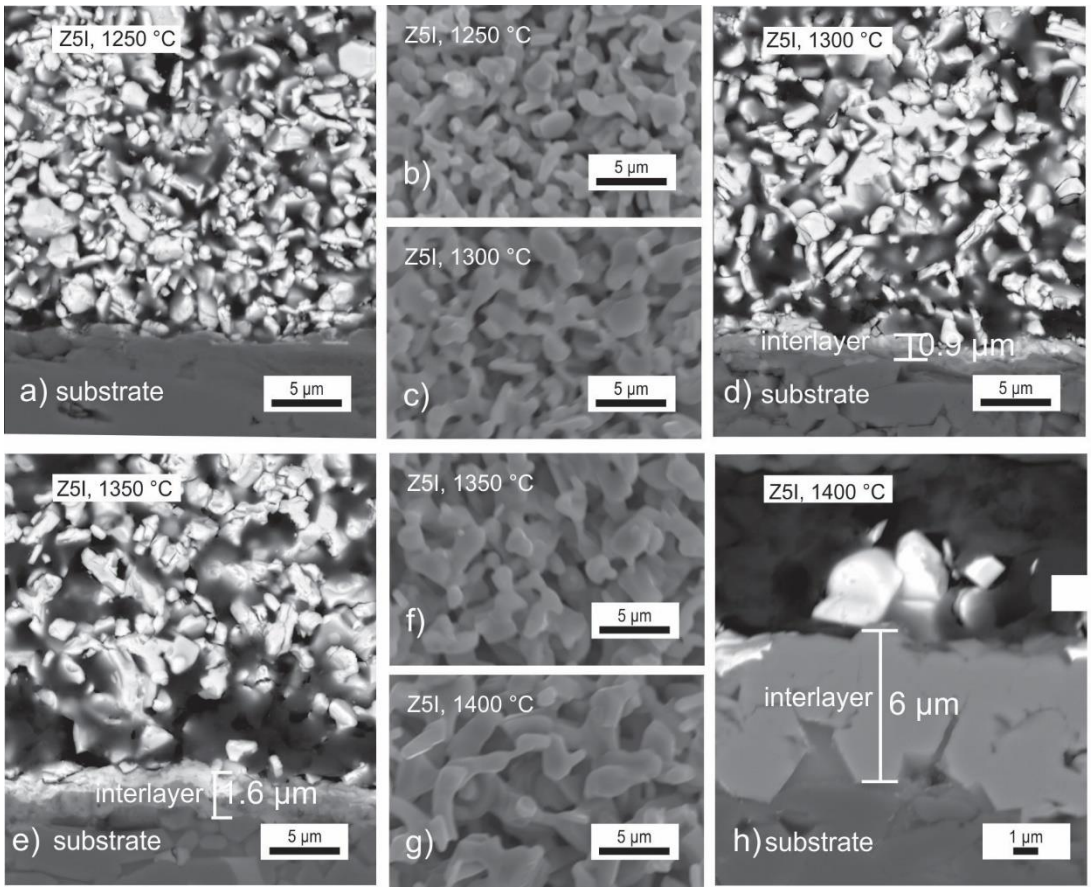


Figure 4.25: SEM micrograph of the Z5I thick-film: cross-section a) and surfaces b) fired temperature of 1250 °C (T1), cross section d) and surfaces c) fired temperature of 1300 °C (T2), cross section e) and surfaces f) fired temperature of 1350 °C (T3) and cross section h) and surfaces g) fired temperature of 1400 °C (T4).

The grains in the fired films are more homogenous (uniform size) with more rounded shapes in comparison to the grains in the initial powder (Figure 4.17). With an increase of the firing temperature the grain size increases and, consequently, also the effective contact area between the grains. Even though the grains are uniformly distributed and connected to each other the films are highly porous. The porosity likely resulted from the low green density of the films after printing, which leaves voids during the burning out of the organic phase of the ink. It is even more pronounced in the film fired at the highest firing temperatures due to the random orientation of the larger, plate-like grains forming larger voids between them. The higher firing temperatures enhanced the reaction between the Z5I film and the Al_2O_3 substrate to form an interface layer, the thickness of which increased with the firing temperature from about 1 µm at the 1300 °C to about 6 µm at 1400 °C. The EDXS analysis showed that the formed reaction layer is $ZnAl_2O_4$. At such high temperatures above 1300 °C also sublimation of the ZnO takes place as reported by Anthrop and Searcy [34], which also influences the sintering and the microstructure development in the film. All the described microstructural features can have an influence on the electrical properties of the fired films.

To measure the specific resistivity of the Z5I thick films I used two types of electrodes, the Pd/Ag and the Pt. The resistivity of the Z5I thick film fired at 1250 °C and measured with the Pd/Ag electrode was equal to 110 $\Omega \cdot$ cm, which was almost three times more than for the Pt electrode (40 Ω·cm). However, the specific resistivity of the Z5I thick-film measured without electrodes was only 2.9 $\Omega \cdot$ cm. The difference comes from the large potential barrier between the metal electrodes and the $(ZnO)_xIn_2O_3$ material, which was already discussed in the literature and the suggested solution was to include an intermediate In-Sn-O (ITO) layer [67]. Based on these results I decided to measure the resistivity without electrodes, while for the configuration of the Z5I-based thermopile I used the Pt electrode. The results of the resistivity and the Seebeck-coefficient measurements of the $(ZnO)_5In_2O_3$ (Z5I) are collected in Table 4.6.

Table 4.6: Electrical properties of Z5I thick-films, fired at different temperatures.

Sample	ρ (500 °C)	S (300 °C)	Px10^{-3} (300 °C)
	m$\Omega \cdot$ cm	μV/K	W/mK^2
Z5I-T1, 1250 °C	2860	N/A	N/A
Z5I-T2, 1300 °C	1080	176	$1.4 \cdot 10^{-3}$
Z5I-T3, 1350 °C	720	136	$2.0 \cdot 10^{-3}$

The specific resistivities of the Z5I thick films fired at 1250 °C, 1300 °C, and 1350 °C are shown in Figure 4.26. The resistivity is lower for a higher firing temperature and is decreased with the increasing temperature of the sample; especially in the case of the film fired at 1250 °C, when the resistivity dropped from about 30 $\Omega \cdot$ cm at 25 °C to about 3 $\Omega \cdot$ cm at 500 °C. In general, the temperature dependence of the specific resistivity is lower in the samples fired at a higher temperature.

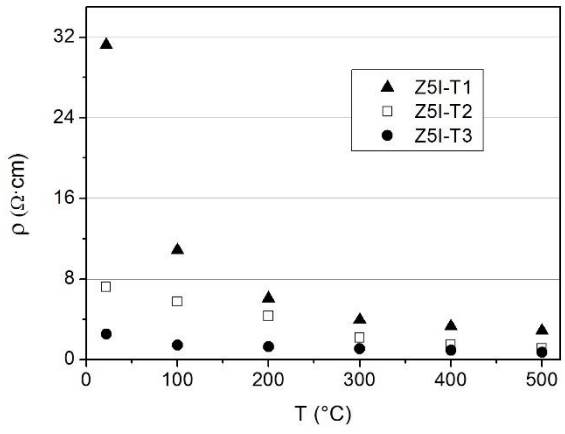


Figure 4.26: Temperature dependence of specific resistivity of the Z5I thick-films fired at different temperatures Z5I-T1 (1250 °C), Z5I-T2 (1300 °C) and Z5I-T3 (1350 °C).

The decrease in the specific resistivity could be correlated with the grain size and the connectivity between them. As shown in Figure 4.25, the grain size is increased with a

higher firing temperature, leading to improved connections between the grains and a reduced number of grain boundaries, contributing to the lower specific resistivity. Hence, with a firing-temperature increase to 1350 °C I managed to lower the specific resistivity of the Z5I film to about 1.8 $\Omega \cdot$ cm at room temperature and to 720 m$\Omega \cdot$ cm at 500 °C. However, at such a high firing temperature a strong reaction between the Z5I TE layer and the substrate is present (Figure 4.25) with the formation of $ZnAl_2O_4$, and the growth of the In-rich grains at the surface of the film (Figure 4.25 g, h) was observed. Although the films are highly porous, the fine diffusion of Al beyond the $ZnAl_2O_4$ interface layer into the Z5I film can result in the doping of ZnO with traces of Al, which can also contribute to a higher conductivity (lower specific resistivity.) [62] At an even higher firing temperature of 1400 °C, it is mainly In-rich grains that are present at the surface of the film (Figure 4.25 h), while at the film/substrate interface a strong interaction with the formation of a thick reaction layer of $ZnAl_2O_4$ was observed (Figure 4.25 h).

The Z5I thermopiles, fired at temperatures of 1300 °C and 1350 °C, were used for the measurements of the Seebeck coefficient (S). In Figure 4.27 the results of the S measurements are shown for a single Z5I thermoelectric leg.

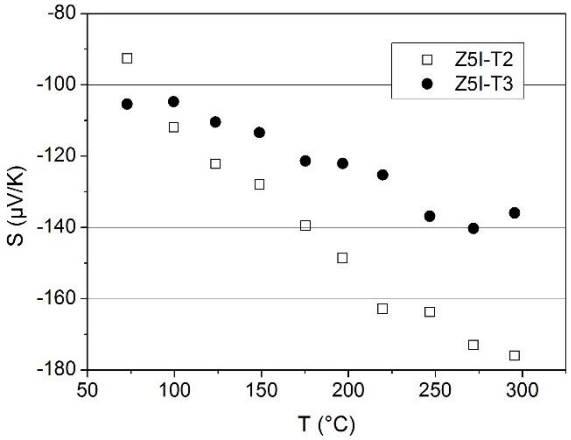


Figure 4.27: Temperature dependence of the Seebeck coefficient of the Z5I thick films fired at different temperatures Z5I-T2 (1300 °C) and Z5I-T3 (1350 °C).

The TE leg fired at 1300 °C, with a lower conductivity, has a higher S than the one fired at a higher temperature (Figure 4.27), which could be correlated to the smaller grain size and hence the larger number of grain boundaries for the energy-filtering effect. The obtained S value for Z5I-T3 was –136 µV/K and is slightly higher than S values of the starting bulk Z5I material [75], which was –130 µV/K and higher than reported in the literature with the value about –100 µV/K [76], all measured at 300 °C.

In Figure 4.28 the results of calculated values for the power factor (P) are shown for a single Z5I thermoelectric leg.

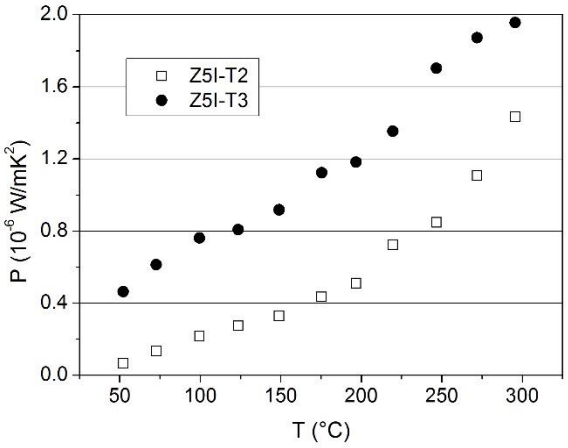


Figure 4.28: Temperature dependence of power factor (P) for Z5I thick films fired at different temperatures Z5I-T2 (1300 °C) and Z5I-T3 (1350 °C).

The TE leg fired at 1300 °C has an about 25% higher S; however, a higher *P,* by about 30%, was obtained for the TE leg fired at 1350 °C due to the about two-times lower specific resistivity. Nevertheless, the *P* of the studied Z5I legs is much lower, about two orders of magnitude, than for the starting bulk Z5I material ($1.7 \cdot 10^{-4}$ W/mK^2 at 300 °C) and the bulk material reported in the literature [54, 75].

The differences in the electrical characteristics between the bulk Z5I and the thick-film Z5I result from their microstructures, as shown in Figure 4.18 and Figure 4.25, respectively. The bulk Z5I material fired for 2 h at 1300 °C has a noticeably higher density and larger grains in comparison to the thick-film Z5I fired for 15 min at 1300 °C, so the grains in the bulk material are also better connected to each other with a smaller number of grain boundaries. The high porosity of the thick-film Z5I and hence the smaller number of electrical paths with a larger number of grain boundaries results in a much higher specific resistivity of 1.08 $\Omega \cdot$ cm in comparison with the bulk material (13m$\Omega \cdot$ cm), both values given for the temperature of 300 °C. Accordingly, the Seebeck coefficient of the thick-film Z5I with value –176 µV/K at 300 °C is larger than for the bulk Z5I (–140 µV/K).

Chapter 5

Conclusions

The topic of my PhD dissertation was the development of thick-film oxide-based electronic ceramics, specifically the thick film varistors and the thick-film oxide-based thermoelectric microgenerators (TEMGs), using the screen-printing technology with the advantages of miniaturization, faster and easier production of complex structures, and lower production costs. While the thick film varistors enable integration of the overvoltage protection into hybrid circuits as a replacement for the surface mounted devices, the TEMGs open a range of applications related either to the cooling in microelectronics or as micro power sources based on harvesting the waste heat by its direct conversion into electricity.

Functional characteristics of polycrystalline ceramics are closely related to their microstructure. Screen-printed thick films with characteristically much lower green density in comparison to conventionally prepared bulk ceramics suffer from poor densification and microstructure development, even more so due to typically much short firing times at lower temperatures and evaporation of volatile substances at a large area-to-volume (A/V) ratio. Overcoming these problems presented the main challenge in the dissertation and was addressed by the development of screen-printed ink with high solids load for maximum green-density and enhanced densification in the firing process. High solids-load inks with good screen-printed characteristics gave the optimal ground for further development of thick-film varistors and TEMGs.

Accordingly, in the first part of the dissertation research, I studied the influence of inks' composition in regard to the used vehicle, the addition of the surfactant and binder and the amount of solids load in the range from 50 to 75 wt.% on the rheological characteristics of inks, their printing properties and the quality of obtained films prior to firing. Based on the obtained results I was able to set the formulation of ink with high solids load of 70 wt. % with good characteristics for screen-printing without the formation of defects in film due to tackiness, poor levelling, creeping or the low mechanical strength of the deposited film, which is typical for the ink with inadequate rheology.

The results in the case of thick-film varistors clearly confirmed the working hypothesis that higher green density of the screen-printed film obtained with the use of the ink with higher solids load also results in higher density of the film. Varistor inks with suitable rheological characteristics and with different solids loads of 50, 60, 65 and 70 wt. % were printed and fired at 900 $^{\circ}$C for 15 minutes and the porosity of the film decreased with an increase of the solids load in the ink. The varistor film prepared from ink with 70 % of

solids load had a noticeably higher density with a negligible porosity. While a different organic vehicle in the inks could have an influence on the final density of these films, a comparison of films from inks based on the same organic vehicle but different solids loads of 65 % and 70 % clearly confirmed the dominant role of the solids load in the ink on the density of the film. A higher density of varistor film with better microstructural homogeneity also manifested in better current–voltage (*I–U*) characteristics, which are expressed a much higher coefficient of nonlinearity α of 16 in comparison to the other samples prepared from inks with lower solids load having α around 10.

In the second part of the dissertation, which was aimed to further enhance the *I-U* characteristics of the thick-film varistors, the composition of the varistor powder mixture used as a solids load in the screen-printing ink was varied for the amount of added Bi_2O_3 from 0.4 to 1.8 mol.% and the Sb_2O_3-to-Bi_2O_3 (Sb/Bi) ratio in the range from 0.25 to 1.25, while the addition of other varistor dopants was constant in all compositions. In accordance with the expectations it confirmed that these two compositional parameters strongly affect the microstructure development and *I-U* characteristics of the thick film varistors, similar as in the case of the bulk varistor ceramics; they determine the temperature of the formation and the amount of Bi_2O_3-rich liquid phase in the system, which enhances densification and grain growth, and facilitates uniform distribution of other varistor dopants for the formation of active electrostatic barriers at the grain boundaries. The results showed that in the case of thick film varistors a larger addition of Bi_2O_3 and the Sb/Bi ratio just below 1 are preferred; the system is less sensitive to the evaporation of the Bi_2O_3 due to the large area-to-volume (A/V) ratio of the film and the larger amount of free Bi_2O_3 in excess to Sb_2O_3 results in the more Bi_2O_3-rich liquid phase for enhanced microstructure development and formation of active "varistor" grain boundaries. Accordingly, the thick film varistor prepared from the composition with 1.6 mol.% Bi_2O_3 and Sb/Bi ratio 0.8, fired at 900 °C for 15 min., had, compared to other samples, a medium break-down voltage U_n of about 117 V and significantly improved current-voltage (*I-U*) nonlinearity with a coefficient α 24. Lower additions of Bi_2O_3 and the same or lowered Sb/Bi ratios in general resulted in a broader grain size distribution with increased fraction of larger grains and hence lower U_n and also α. At Sb/Bi ratio > 1 the absence of free Bi_2O_3-rich liquid phase and the formation of the spinel phase hindered the microstructure development, which resulted in an increased break-down voltage U_n at a lower nonlinearity coefficient α.

Breakdown voltage U_n decreased with increasing the firing time from 15 min to 30 min, and 60 min, which likely resulted from increasing the average grain size. However, a significant decrease in the coefficient of nonlinearity α was more detrimental, which was attributed to the Bi_2O_3 evaporation.

In the third part of the dissertation, the preparation of the screen-printed thick-film thermoelectric (TE) structures made from *p*-type $Ca_3Co_4O_9$ and from *n*-type $(ZnO)_5In_2O_3$ legs was studied in the development of thick-film TE microgenerators (TEMGs).

I successfully prepared the $Ca_3Co_4O_9$-based (Ca349) thermopile with a Seebeck coefficient of about 156 µV/K at 300 °C, resistivity as low as 13.7 mΩcm, measured at 500 °C. The power factor calculated for a single leg was $1.6 \cdot 10^{-4}$ W/K^{2}m. Interestingly, such TE parameters of the Ca349 thick-films on the alumina substrate, fired at 920 °C for 15

min., are entirely comparable to the values reported in the literature for the bulk Ca349 ceramics prepared by a classical ceramic process and resulted from microstructural similarity.

In the case of the $(ZnO)_5In_2O_3$-based thermopile it showed that poor densification of the film and its consequent high resistivity represent a serious obstacle. I have managed to lower the resistivity of the $(ZnO)_5In_2O_3$-based thermopile to 720 mΩ·cm at a temperature of 500 °C by using a higher firing temperature of 1350 °C. However, it also resulted in a strong reaction of the film with the Al_2O_3 substrate and the formation of a $ZnAl_2O_4$ layer at the interface, noticeable evaporation of ZnO and the formation of In_2O_3-rich grains on the surface of the film. The Seebeck coefficient of the $(ZnO)_5In_2O_3$ thermoelectric leg was as high as –176 µV/K and the power factor (P) $1.4 \cdot 10^{-6}$ W/K^{2}m. While the S values were comparable with the data reported in the literature for the bulk Z5I ceramics, the values obtained for P were several orders of magnitude lower due to much larger resistivity of the thick films resulting from the large porosity and weak connectivity among the grains. Nevertheless, a Z5I-based microgenerator has been, to the best of my knowledge, prepared and characterized for the first time.

Results of my study confirmed that the screen-printing technology is a promising fabrication method also for the preparation of the oxide-based TEGs, while the main challenges were identified as well.

References

[1] F. Menil, H. Debeda and C. Lucat , "Screen-printed thick-films: From materials to funtional device," *Journal of the European Ceramic Society,* vol. 25, no. 12, pp. 2105-2113, 2005.

[2] P. J. Holmes and R. G. Loasby, Handbook of thick film technology, Scotland: Electrocemical Publications Ltd, 1976.

[3] M. Prudenziati and J. Hormadaly , Printed films, Materials science and appications in sensors, electronics and photonics, Cambridge: Woodhead Publishing Ltd, 2012.

[4] H. B. Zhang , S. L. Jiang and K. Kajiyoshi, "Control of paste rheology and piezoelectric properties of $Bi_{0.5}(Na_{0.82}K_{0.18})_{(0.5)}TiO_3$ lead-free piezoelectric thick films deposited by screen printing," *International Journal of Applied Ceramic Technology,* vol. 8, no. 3, pp. 658-668, 2011.

[5] H.-W. Lin, C.-P. Chang, W.-H. Hwu and M.-D. Ger, "The rheological behaviors of screen-printing pastes," *Journal of Materials Processing Technology,* vol. 197, no. 1-3, pp. 284-291, 2008.

[6] L. M. A. de la Rubia , M. Peiteado, J. F. Fernández, A. C. Caballero, J. Holc, S. Drnovsek, D. Kuscer, S. Macek and M. Kosec, "Thick film ZnO based varistors prepared by screen printing," *Journal of the European Ceramic Society,* vol. 26, no. 14, pp. 2985-2989, 2006.

[7] G. Korotcenkov, "Materials for Thick Film Technology," in *Handbook of Gas Sensors Materials*, New York, Springer New York, 2013, pp. 249-254.

[8] P. A. Serra, Biosensors - Emerging Materials and Applications, Rijeka: InTech, 2011.

[9] A. Willfahrt, Screen Printed Thermoelectric Devices, Linkoping: Linkoping University Electronic Press, 2014.

[10] P. Markowski , E. Prociow and A. Dziedzic, "Mixed thick/thin-film thermocouples for thermoelectric microgenerators and laser power sensor," *Optica Applicata,* vol. 39, no. 4, pp. 681-690, 2009.

[11] M. R. Somalu, V. Yufit and N. P. Brandon , "The effect of solids loading on the screen-printing and the properties of nikel/scandia-stabilized-zirconia anodes for solid

oxide fuel cells," *International Journal of Hydrogen Energy,* vol. 38, no. 22, pp. 9500-9510, 2012.

[12] M. de la Rubia, M. Peiteado, J. de Frutos , F. Rubio-Marcos, J. F. Fernandez and A. C. Caballero, "Improved non-linear behaviour of ZnO-based varistor thick films prepared by tape casting and screen printing," *Journal of the European Ceramic Society,* vol. 27, no. 13-15, pp. 3887-3891, 2007.

[13] T. G. Mezger , The rheology handbook 2nd ed., Hannover, Germany: Vincentz Network GmbH & Co., 2006.

[14] G. Schramm, A practical approach to rheology and rheometry, Karlsruhe: Gabrueder HAAKE GmbH, 1998.

[15] S. Zurcher and T. Graule, "Influence of dispersant structure on the rheological propeties of highly-concentrated zirconia dispersions," *Journal of the European Ceramic Society,* vol. 25, no. 6, pp. 863-873, 2005.

[16] A. Sanson, D. Gardini, G. Montanari, C. Galassi and E. Roncari, "Key role of milling in the optimization of TiO_2 nanoinks," *Journal of Materials Research,* vol. 21, no. 6, pp. 1561-1569, 2006.

[17] V. Kardashian and S. Vellanki , "A method for the rheological characterization of thick-film pastes," *IEEE Transactions on Components, Hybrids, and Manufacturing Technology,* vol. 2, no. 2, pp. 232-239, 1979.

[18] F. Tanaka and S. F. Edwards, "Viscoelastic properties of physically cross-linked networks - transient network theory," *Macromolecules,* vol. 25, no. 5, pp. 1516-1523, 1992.

[19] R. E. Trease and R. L. Dietz, "Rheology of pastes in thick-film printing," *Solid State Technology,* vol. 15, no. 1, pp. 39-43, 1972.

[20] D. R. Clarke, "Varistor ceramics," *Journal of the American Ceramic Society,* vol. 82, no. 3, pp. 485-502, 1999.

[21] T. K. Gupta, "Application of zink oxide varistors," *Journal of the American Ceramic Society,* vol. 73, no. 7, pp. 1817-1840, 1990.

[22] P. R. Bueno, J. A. Varela and E. Longo , "SnO_2, ZnO and related polycrystalline compound semiconductors: An overview and review on the voltage-depandent resistance (non-ohmic) feature," *Journal of the European Ceramic Society,* vol. 28, no. 3, pp. 505-529, 2008.

[23] L. Hozer, Semiconductor ceramics, Grain boundary effects, Wroclaw, Poland: Polish scientific publishers pwn Ltd. , 1994.

[24] S. C. Pillai , J. M. Kelly , R. Ramesh and D. E. McCormack, "Advances in the synthesis of ZnO nanomaterials for varistor device," *Journal of Materials Chemistry C,* vol. 1, no. 20, pp. 3268-3281, 2013.

[25] M. Inada, "Crystal phases of nonohmic zinc oxide ceramics," *Japanese journal of applied physics ,* vol. 17, no. 1, pp. 1-10, 1978.

[26] M. Inada, "Formation mechanism of nonohmic zinc oxide ceramics," *Japanese journal of applied physics ,* vol. 19, no. 3, pp. 409-419, 1980.

[27] M. L. Arefin, F. Reather , D. Dolejš and A. Klimera, "Phase fromation during liquid phase sintering of ZnO ceramics," *Ceramics International,* vol. 35, no. 8, pp. 3313-3320, 2009.

[28] H. R. Phillip and F. M. Levinson, "Degradation phenomena in ZnO varistors: a review," in *Advances in Cermics*, Cincinnati, 1982.

[29] J. Ott, A. Lorenz, M. Harrer, E. A. Preissner , C. Hesse, A. Feltz, A. H. Whitehead and M. Schreiber, "The influence of Bi_2O_3 and Sb_2O_3 on the electrical properties of ZnO-based varistors," *Journal of Electroceramics,* vol. 6, no. 2, pp. 135-146, 2001.

[30] S. Bernik, J. Bernard , N. Daneu and A. Rečnik , "Microstructre development in low-antimony oxide-doped zinc oxide ceramics," *Journal of the American Ceramic Society,* vol. 90, no. 10, pp. 3239-3247, 2007.

[31] M. Pietado, M. A. de la Rubia , M. J. Velasco , M. J. Valle and A. C. Caballero, "Bi_2O_3 vaporization from ZnO-based varistors," *Journal of the European Ceramic Society,* vol. 25, no. 9, pp. 1675-1680, 2005.

[32] X. Dong , X. Cheng, X. Yan, H. Xu and L. Shi, "Sintering process as relevant parameter for Bi_2O_3 vaporization from Zn-Bi_2O_3-based ceramics," *Transactions of Nonferrous Metals Society of China,* vol. 19, no. 6, pp. 1526-1532, 2009.

[33] R. Metz, H. Delalu , J. R. Vignalou, N. Achard and M. Elkhatib, "Electricl properties of varistor in relation to their true bismuth composition after sintering," *Materials Chemistry and Physics,* vol. 63, no. 2, pp. 157-162, 2000.

[34] D. Anthrop and A. Searcy, "Sublimation and thermodynamic properties of zinc oxide," *The Journal of Physical Chemistry,* vol. 68, no. 8, pp. 2335-2342, 1964.

[35] E. Mis, A. Dziedzic and W. Mielcarek, "Microvaristors in the thick-film and LTCC circuits," *Microelectronics Reliability,* vol. 49, no. 6, pp. 607-613, 2009.

[36] C. Lucat, M. Martin, M. Debeda-Hickel, A. Largeteau and F. Menil, "Screen-printed varistors: New strategy for high non-linear coefficient," *Journal of the European Ceramic Society,* vol. 27, no. 13-15, pp. 3883-3886, 2007.

[37] M. A. de la Rubia, M. Peiteado, J. F. Fernandez and A. C. Caballero, "Compact shape as a relevant parameter for sintering ZnO–Bi_2O_3 based varistors," *Journal of the European Ceramic Society,* vol. 24, no. 6, pp. 1209-1212, 2004.

[38] D. Xu, . X.-n. Cheng, X.-h. Yan, H.-x. Xu and L.-y. Shi, "Sintering process as relevant parameter for Bi_2O_3 vaporization from ZnO-Bi_2O_3-based varistor ceramics," *Transactions of Nonferrous Metals Society of China,* vol. 19, no. 6, pp. 1526-1532, 2009.

[39] M. Peiteado, M. A. de la Rubia, J. de Frutos and T. Jardiel, "ZnO-based varistor thick films with high non-linear electrical behavior," *Journal of Electroceramics,* vol. 23, no. 1, pp. 62-66, 2009.

[40] A. Vojta and D. R. Clarke, "Microstructural origin of current localization and ''puncture'' failure in varistor ceramics," *Journal of Applied Physics,* vol. 81, no. 2, pp. 985-993, 1997.

[41] A. Vojta and T. Vojta, "Current localization in nonlinear inhomogeneous media," *Journal of Physics-Condensed Matter,* vol. 8, no. 33, pp. L461-L467, 1996.

[42] H. Wang, M. Bartkowiak, F. A. Modine, R. B. Dinwiddie, L. A. Boatner and G. D. Mahan, "Nonuniform heating in zinc oxide varistors studied by infrared imaging and computer simulation," *Journal of the American Ceramic Society,* vol. 81, no. 8, pp. 2013-2022, 1998.

[43] N. V. Nong, A. J. Samson, N. Pryds and S. Linderoth, "Microstructure and thermoelectric properties of screen-printed thick films of misfit-layered cobalt oxides with Ag addition," *Journal of Electronic Materials,* vol. 41, no. 6, pp. 1280-1285, 2012.

[44] J. G. Snyder and E. S. Toberer, "Complex thermoelectric materials," *Nature Materials,* vol. 7, no. 2, pp. 105-114, 2008.

[45] J. He and Y. Liu, "Oxide thermoelectrics: The challenges, progress, and outlook," *Journal of Material Research,* vol. 26, no. 15, pp. 1762-1772, 2011.

[46] W. J. Fergus, "Oxide materials for high temperature thermoelectric energy conversion," *Journal of the European Ceramic Society,* vol. 32, no. 3, pp. 525-540, 2012.

[47] K. Koumoto, R. Funahashi, E. Guilmeau, Y. Miyazaki, A. Weidenkaff, Y. F. Wang and C. L. Wan, "Thermoelectric ceramics for energy harvesting," *Journal of the American Ceramic Society,* vol. 96, no. 1, pp. 1-23, 2013.

[48] S. Misture and D. Edwards, "High-temperature oxide thermoelectrics," *American Ceramic Society Bulletin,* vol. 91, no. 3, pp. 24-27, 2012.

[49] S. M. Choi, K. H. Lee, C. H. Lim and W. S. Seo, "Oxide-based thermoelectric power generation module using p-type $Ca_3Co_4O_9$ and n-type $(ZnO)_7In_2O_3$ legs," *Energy Conversion and Management,* vol. 51, no. 1, pp. 335-339, 2011.

[50] S. Lambert, H. Leligny and D. Grebille, "Three forms of the misfit layered cobaltite $[Ca_2CoO_3]$ $[CoO_2]_{1.62} \cdot$ A 4D structural investigation," *Journal of Solid State Chemistry,* vol. 160, no. 2, pp. 322-331, 2001.

[51] S. Chen, X. Y. Song, X. Q. Chen, Y. Chen, E. J. Barbero, E. L. Thomas and P. N. Barnes, "Effect of precursor calcination temperature on the microstructure and thermoelectric properties of $Ca_3Co_4O_9$ ceramics," *Journal of Sol-Gel Science and Technology,* vol. 64, no. 3, pp. 627-636, 2012.

[52] Y. Miyazaki, "Crystal structure and thermoelectric properties of the misfit-layered cobalt oxides," *Solid State Ionics,* vol. 172, no. 1-4, pp. 463-467, 2004.

[53] D. Kenfaui, D. Chateigner, M. Gomina and J. G. Noudem, "Anisotropy of the mechanical and thermoelectric properties of hot-pressed single-layer and multilayer thick $Ca_3Co_4O_9$ Ceramics," *International Journal of Applied Ceramic Technology,* vol. 8, no. 1, pp. 214-226, 2011.

[54] X. Liang and D. R. Clarke, "Relation between thermolectric properties and phase equilibria in the ZnO-In_2O_3 binary system," *Acta Materialia,* vol. 63, pp. 191-201, 2014.

[55] J. P. Fleurial, G. J. Snyder, J. A. Herman, P. H. Giauque, W. Phillips, M. A. Ryan, P. Shakkottai, E. A. Kolawa and M. A. Nicolet, "Thick-film thermoelectric microdevices," in *International Conference on Thermoelectrics (ICT'99)*, Baltimore, MD, USA, 1999.

[56] R. Venkatasubramanian, E. Silvola and T. Colpitts, "Thin-film thermoelectric devices with high room-temperature figures of merit," *Nature ,* vol. 413, pp. 597-602, 2001.

[57] A. Chen, D. Madan, P. K. Wright and J. W. Evans, "Dispersed-printed planar thick-film thermoelectric energy genrators," *Journal of Micromechanics and Microengineering,* vol. 21, pp. 104006-104013, 2011.

[58] Z. Cao, E. Koukharenko, R. N. Torah, J. Tudor and S. P. Beeby, "Flexible screen printed thick film thermoelectric generators with reduced materil resistivity," *Yournal of Physics: Conference Series ,* vol. 557, pp. 012016-021021, 2014.

[59] T. Varghese, C. Hollar, J. Richardson, N. Kempf, C. Han, P. Gamarachchi, D. Estrade, R. J. Mehta and Y. Zhang, "High-performance and flexible thermoelectric films by screen printing solution-processed nanoparticle crystals," *Scientific Reports,* vol. 6, p. 33135, 2016.

[60] H. B. Lee, H. J. Yang, J. H. We, K. Kim, K. C. Choi and B. J. Cho, "Thin-film thermoelectric module for power generator applications using a screen-printing method," *Journal of Electronic Materials,* vol. 40, no. 5, pp. 615-619, 2011.

[61] P. Markowki and A. Dziedzic, "Planar and three-demensional thick-film thermoelectric microgenerators," *Microelectronics Reliability,* vol. 48, no. 6, pp. 890-896, 2008.

[62] Y. Zhang and J. Han, "Microstructure and temperature coefficient of resistivity for ZnO ceramics doped with Al_2O_3," *Materials Letters,* vol. 60, no. 20, pp. 2522-2525, 2006.

[63] H. Debeda-Hickel, C. Lucat and F. Menil, "Influence of the densification parameters on screen-printed component properties," *Journal of the European Ceramic Society,* vol. 25, no. 12, pp. 2115-2119, 2005.

[64] P. Markowski , "Thick-film photoimageable and laser-shaped arms for thermoelectric microgenerators," *Microelectronics International,* vol. 28, no. 3, pp. 43-50, 2011.

[65] J. W. Phair, M. Lundberg and A. Kaiser, "Leveling and thixotropic characteristics of concentrated zirconia inks for screen-printing," *Rheologica Acta,* vol. 48, no. 2, pp. 121-133, 2009.

[66] D. J. Green, O. Guillon and J. Rodel, "Constrained sintering: A delicate balance of scales," *Journal of the European Ceramic Society,* vol. 28, no. 7, p. 1451–1466, 2008.

[67] C. H. Lim, S. Choi, W. Seo, M. Lee, K. Lee and H. Park , "A study of electrodes for thermoelectric oxides," *Electronic Materials Letters,* vol. 9, no. 4, pp. 445-449, 2013.

[68] J. W. Goodwin and R. W. Hughes, Rheology for chemists, 2nd ed., Cambridge, UK: The Royal Society of Chemistry, 2008.

[69] R. L. Hoffman, "Discontinuous and dilatant viscosity behavior in concentrated suspensions. II. theory and experimental tests," *Journal of Colloid and Surface Science,* vol. 46, no. 3, pp. 471-506, 1972.

[70] S. Wang, G. Yan, S. Chen, Z. Bai and J. Wan, "Effect of microstructure on the thermoelectric properties of CSD-grown $Bi_2Sr_2Co_2O_y$ thin films," *Chin. Phys. B,* vol. 22, no. 3, 2013.

[71] B. Moyzhes and V. Nemchinsky, "Thermoelectric figure of merit of metal-semiconductor barrier structure based on energy relaxation length," *Applied Physics Letters,* vol. 73, no. 13, pp. 1895-1897, 1998.

[72] Y. Seto, "The electrical properties of polycrystalline silicon films," *Journal of Applied Physics,* vol. 46, no. 12, pp. 5247-5254, 1975.

[73] M. Presečnik and S. Bernik, "Effect of processing methods on the microstructural development and thermoelectric properties of $Ca_3Co_4O_9$," in *International Conference on Microelectronics, Devices and Materials MIDEM - Society for Microelectronics*, Ljubljana, 2014..

[74] S. Bernik and M. Pribošek, "Construction and characterization of a Z-Meter setup for thermoelectric measurements of materials," in *49th International conference on Microelectronics, Devices and Materials MIDEM*, Kranjska gora, Slovenia, 2013.

[75] M. Košir, N. Daneu, A. Rečnik, M. Čeh, E. Guilmeau and S. Bernik, "Thermoelectric ceramics based on the ZnO-In_2O_3 system," in *International Conference on Microelectronics, Devices and Materials, MIDEM - Society for Microelectronics, Electronic Components and Materials*, Ljubljana, 2014.

[76] H. Ohta, W. Seo and K. Koumoto, "Thermoelectric properties of homologous compounds in the ZnO-In_2O_3 system," *Journal of the American Ceramic Society,* vol. 79, no. 8, pp. 2193-2196, 1996.

Bibliography

Publications Related to the Thesis

Journal Articles

R. Rudež, J. Pavlič, S. Bernik, "Preparation and influence of highly concentrated screen-printing inks on the development and characteristics of thick-film varistors," *Journal of the European Ceramic Society*, vol. 35, no. 11, pp. 3013-2023, 2015.

R. Rudež, P.Markowski, M. Presečnik, M. Košir, A. Dziedzic, S. Bernik, "Development of thick-film thermoelectric microgenerators based on p-type $Ca_3Co_4O_9$ and n-type $(ZnO)_5In_2O_3$ legs," *Ceramics International*, , iss. 10, part A, pp. 13201-13209, 2015.

Published scientific conference contribution

R. Rudež, S. Bernik, "Studies of concentrated inks for the screen printing of thick-film varistors," in proceedings of 49th International Conference on Microelectronics, Devices and Materials & theWorkshop on Digital Electronic Systems, Kranjska Gora, Slovenia: MIDEM - Society for Microelectronics, Electronic Components and Materials, 2013, str. 245-250.

R. Rudež, P. Markowski, A. Dziedzic, S. Bernik, "Development of oxide-based thermoelectric microgenerators based on p-type $Ca_3Co_4O_9$ and n-type $(ZnO)_5In_2O_3$ thermopiles," in proceedings of the 50th International Conference on Microelectronics, Devices and Materials, Ljubljana, Slovenia: MIDEM - Society for Microelectronics, Electronic Components and Materials, 2014, pp. 215-220.

I. Poljanšek, R. Rudež, D. Pahovnik, E. Žagar, "Synthesis and characterization of dendritic polymers for drug delivery," in Slovenski kemijski dnevi, Maribor, Slovenia: FKKT, 2010, pp. 1-5.

Published scientific conference contribution abstract

R. Rudež, S. Bernik, "The effect of Bi_2O_3 and Sb_2O_3 on the microstructure and electrical properties of the thick - film varistors," in *Program and the book of abstracts*, 3rdConference of the Serbian Ceramic Society, Belgrade, Serbia: Institute for Multidisciplinary Research, University of Belgrade, 2015, pp. 60.

R. Rudež, S. Bernik, "Concentrated inks for screen printing thick-films varistors," in *Program and book of abstracts*, 21st International Conference on Materials and Technology: Inštitut za kovinske materiale in tehnologije, 2013, pp. 158.

R. Rudež, P. Markowski, A. Dziedzic, S. Bernik, "Development of oxide-based thermoelectric microgenerator based on p-type $Ca_3Co_4O_9$ and n-type $(ZnO)_5In_2O_3$ termopiles," in the *program and abstract book 9th Young researchers' day, Ljubljana, Slovenia:*. Institut Jožef Stefan, 2015, pp. 35.

R. Rudež, P. Markowski, A. Dziedzic, S. Bernik, "Development of oxide-based thermoelectric micro generator based on p-type $Ca_3Co_4O_9$ and n-type $(ZnO)_5In_2O_3$ thermopile," in *Detailed programme & abstracts book*, 12th European Conference on Thermoelectrics, Madrid, Spain: European Thermoelectric Society, 2014, pp. 224.

Invited lecture at foreign university

R. Rudež, "Development of oxide-based thermoelectric microgenerator based on p-type $Ca_3Co_4O_9$ and n-type $(ZnO)_5In_2O_3$" : invited talk. Wrocław: Faculty of Microsystem Electronics and Photonics, University of Technology, 28 maj 2014.

Biography

The author of this thesis Rok Rudež was born on September 20th, 1985 in Kranj. After finishing Gymnasium, he enrolled in the Chemistry Programme at the Faculty of Chemistry and Chemical Technology, University of Ljubljana. He defended his bachelor thesis in 2009 under the supervision of Dr. Drago Kočar and Dr. Ida Poljanšek. In 2012, he applied for the position of a Young Researcher through the Slovenian Research Agency programme and enrolled the Nanosciences and Nanotechnologies programme at the Jožef Stefan International Postgraduate School. In his doctoral research he studied the development of oxide-based thick film electronic ceramics, focused on varistors and themoelectrics, all under the supervision of Prof. Dr. Slavko Bernik. He presented his work at several international and Slovene conferences, and published two articles in recognized international journals.